



THE HONG KONG  
POLYTECHNIC UNIVERSITY

香港理工大學

Pao Yue-kong Library

包玉剛圖書館

---

## Copyright Undertaking

This thesis is protected by copyright, with all rights reserved.

**By reading and using the thesis, the reader understands and agrees to the following terms:**

1. The reader will abide by the rules and legal ordinances governing copyright regarding the use of the thesis.
2. The reader will use the thesis for the purpose of research or private study only and not for distribution or further reproduction or any other purpose.
3. The reader agrees to indemnify and hold the University harmless from and against any loss, damage, cost, liability or expenses arising from copyright infringement or unauthorized usage.

### IMPORTANT

If you have reasons to believe that any materials in this thesis are deemed not suitable to be distributed in this form, or a copyright owner having difficulty with the material being included in our database, please contact [lbsys@polyu.edu.hk](mailto:lbsys@polyu.edu.hk) providing details. The Library will look into your claim and consider taking remedial action upon receipt of the written requests.

BASIC RESEARCH IN  
WIRELESS INDUCTIVE POWER TRANSFER

ZHICONG HUANG

Ph.D

The Hong Kong Polytechnic University

2018



*The Hong Kong Polytechnic University*  
*Department of Electronic and Information Engineering*

# **Basic Research in Wireless Inductive Power Transfer**

Zhicong HUANG

A thesis submitted in partial fulfillment of the requirements for  
the degree of Doctor of Philosophy

August 2017



# Certificate of Originality

I hereby declare that this thesis is my own work and that, to the best of my knowledge and belief, it reproduces no material previously published or written, nor material which has been accepted for the award of any other degree or diploma, except where due acknowledgment has been made in the text.

\_\_\_\_\_ (Signed)

Zhicong HUANG (Name of student)



# Abstract

This thesis focuses on power control and efficiency optimization of inductive power transfer (IPT) systems, including the design of a single-stage IPT converter for electric vehicle (EV) battery charging, a maximized efficiency control of a three-stage IPT system and a development of a stability criteria of power distribution systems. Power is transferred via magnetic field coupling of an IPT system, that it is a kind of commercially available wireless power transfer (WPT) technique. Compared with conventional wired power transfer, IPT can be wireless, convenient, reliable and flexible. IPT has attracted many attentions in a wide spread applications, from low power to high power, from short distance to mid-distance and from stationary to dynamic. However, there are still some challenges in practical IPT applications due to low and varying coupling coefficient of the loosely-coupled transformer. Therefore, the study in this thesis will focus on power control and efficiency optimization in some specific applications. The applications are explained as follows.

Maximum power efficiency and load-independent output are widely studied for the IPT converters with basic compensation topologies (i.e., series-series, series-parallel, parallel-series, parallel-parallel). The operating frequencies of the IPT converters to achieve maximum power efficiency and load-independent output depend on the design of the compensation networks. In this thesis, we study the feasibility to achieve maximum power efficiency and load-independent output simultaneously with appropriate design of the compensation networks.

Taking the variation of coupling coefficient  $k$  into consideration, secondary series compensation topologies (i.e., series-series, parallel-series) are more suitable in dynamic applications, because the design of the compensation network is irrelevant to  $k$ .

In stationary EV battery charging application, a typical charging profile uses constant current (CC) charging followed by constant voltage (CV) charging, with power varying from the maximum rated power down to a minimum of 3%. An IPT system should be designed with minimum number of converter stages to achieve high efficiency. However, high efficiency for such a wide load range is difficult to achieve. Moreover, the efficiency-to-load relationship is distinctly different for CC and CV charging, posing difficulties for single-stage IPT converter design. In this thesis, a single-stage IPT converter is designed, complied with the battery charging profile. Soft switching is ensured and overall efficiency is optimized for the whole process of CC charging and CV charging.

Due to the variation of the coupling coefficient, it is hard to control the output power together with maintaining maximum power efficiency for a single-stage IPT converter. Therefore, in practical IPT applications with varying coupling coefficient, it is common to cascade the IPT converter with front-side and load-side DC/DC converters. The two DC/DC converters are normally controlled cooperatively for the requirements of output regulation and maximum efficiency tracking using a control technique based on perturbation and observation, which is inevitably slow in response. In this thesis, a decoupled control technique is developed. the load-side DC/DC converter is solely responsible for output regulation, while the front-side converter is responsible for impedance-matching of the IPT converter by controlling its input-to-output voltage ratio. DC and small-signal transfer functions are derived for designing the parameters of fast linear controller.

It is common that a DC power distribution system consists of a single

source and multiple load converters sharing a common DC voltage bus. Same configuration can also be adopted in an IPT power distribution system. Without a voltage regulator, the series-series compensated IPT (SSIPT) converter provides a constant current output with high output impedance where operating at its power efficient point. Multiple load-side converters can be connected to the SSIPT converter in parallel. Such current source DC power distribution system is relatively unexplored. In this thesis, a more general set of criteria based on power balance is proposed. To ensure the stability of the system, the load-side converters are distinguished between voltage-driven and current-driven converters.

All the applications proposed are developed with detailed analysis, verified with simulation and experimental measurements from some appropriate prototype converters.



# Publications

## Journal papers

- **Z. Huang**, S. C. Wong, C. K. Tse, “Revisiting stability criteria for DC power distribution systems based on power balance,” *CPSS Transactions on Power Electronics and Applications*, vol. 2, no. 1, March 2017.
- **Z. Huang**, S. C. Wong, C. K. Tse, “Design of a single-stage inductive-power-transfer converter for efficient EV battery charging,” *IEEE Transactions on Vehicular Technology*, vol. 66, no. 7, pp. 5808-5821, July 2017.
- **Z. Huang**, S. C. Wong, C. K. Tse, “Control design for optimizing efficiency in inductive power transfer systems,” *IEEE Transactions on Power Electronics*, vol. 33, no. 5, pp. 4523-4534, May 2018.

## Conference papers

- **Z. Huang**, S. C. Wong, C. K. Tse, “Design methodology of a series-series inductive power transfer system for electric vehicle battery charger application,” in *Proceedings, IEEE Energy Conversion Congress and Exposition (ECCE)*, 2014, pp. 1778–1782.
- **Z. Huang**, S. C. Wong, C. K. Tse, “Fast linear control for maximum energy efficiency of wireless power transfer systems,” in *Proceedings, International*

*Future Energy Electronics Conference (IFEEC2017-IEEE ECCE Asia),*  
2017, pp. 19–24.

# Acknowledgments

It is my pleasure to have the opportunity to pursue my Ph.D. at the Hong Kong Polytechnic University. During my Ph.D. study, I have gained not only research skills but also valuable experience in tackling difficult problems, which I believe will help me rise to future challenges.

First and foremost, I would like to express my sincere gratitude and appreciation to my supervisor Dr. S. C. Wong, for his kind support, patient guidance and continuous encouragement throughout my Ph.D. study. With his deep insights, innovative ideas and logical thinking, he not only helps me immensely to complete the Ph.D. study, but also inspires me how to conduct research.

Secondly, special thanks should go to Prof. Michael C. K. Tse, the leader of the Applied Nonlinear Circuits and Systems Research Group. His constructive ideas and effective comments always help me move forward in my research area. Weekly seminars organized by him also open doors for me to many other research areas.

Thirdly, I am very grateful to all the colleagues and friends in the Applied Nonlinear Circuits and Systems Research Group. It is my honor to be a member of this research group and I really enjoy the time studying with you here.

Last but not least, I would like to thank my families. Without their love and support, none of my accomplishments today would have ever been possible.



# Contents

<b>List of Figures</b>	<b>xix</b>
<b>List of Tables</b>	<b>xxvii</b>
<b>Abbreviations List</b>	<b>xxix</b>
<b>Nomenclature List</b>	<b>xxxii</b>
<b>1 Introduction</b>	<b>1</b>
1.1 Motivation . . . . .	1
1.2 Fundamentals of Wireless Power Transfer . . . . .	3
1.2.1 Electromagnetic Radiation . . . . .	3
1.2.2 Capacitive Power Transfer . . . . .	4
1.2.3 Inductive Power Transfer . . . . .	5
1.3 Applications of IPT systems . . . . .	6
1.3.1 Consumer Electronics . . . . .	6
1.3.2 Biomedical Implants . . . . .	7
1.3.3 Electric Vehicles . . . . .	8
1.3.4 Other applications . . . . .	10
1.4 Literature Review . . . . .	10
1.4.1 Coupler Design . . . . .	10
1.4.2 Compensation Network . . . . .	13

1.4.3	Control . . . . .	14
1.4.4	Safety . . . . .	16
1.5	Objective of the Thesis . . . . .	17
1.6	Outline of the Thesis . . . . .	18
<b>2</b>	<b>Overview of Four Basic IPT Compensation Topologies</b>	<b>21</b>
2.1	Four Basic Compensation Topologies . . . . .	22
2.2	Maximum Power Efficiency . . . . .	22
2.3	Load-independent Current and Load-independent Voltage Output	29
2.4	Load-independent Output and Maximum Efficiency . . . . .	32
2.5	Summary . . . . .	36
<b>3</b>	<b>Single-stage IPT Converter for EV Battery Charging</b>	<b>37</b>
3.1	Implementation Cases for EV charging . . . . .	39
3.2	Characteristics of SSIPT converter . . . . .	41
3.2.1	Efficiency and Control . . . . .	41
3.2.2	Practical Transconductance and Voltage Transfer Ratio .	44
3.2.3	Input Phase Angle . . . . .	49
3.2.4	Control Scheme . . . . .	51
3.3	Design Consideration . . . . .	53
3.3.1	Maximizing Overall Efficiency . . . . .	53
3.3.2	Loosely-coupled Transformer . . . . .	55
3.3.3	Converter Design . . . . .	59
3.4	Experiment Evaluation . . . . .	61
3.4.1	Experiment . . . . .	61
3.4.2	Soft Switching in LIC and LIV Operation . . . . .	64
3.4.3	Efficiency . . . . .	69
3.5	Summary . . . . .	73

<b>4</b>	<b>Control Design for Optimizing Efficiency</b>	<b>75</b>
4.1	Maximum IPT Converter Efficiency and Input-to-output Ratio . . . . .	78
4.2	SSIPT Converter Voltage Ratio Control . . . . .	79
4.3	Controller Design . . . . .	82
4.3.1	Small-signal Model of Transconductance . . . . .	83
4.3.2	Voltage Error Control Loop . . . . .	87
4.3.3	Stability Analysis . . . . .	89
4.4	Experiment Evaluation . . . . .	90
4.4.1	Design of Control Parameters . . . . .	90
4.4.2	Small-Signal Response . . . . .	95
4.4.3	Transient Response Against Variation of $k$ . . . . .	95
4.4.4	Transient Response Against Load Variations . . . . .	99
4.4.5	Discussion . . . . .	102
4.5	Summary . . . . .	103
<b>5</b>	<b>Stability Criteria for SSIPT Power Distribution System</b>	<b>105</b>
5.1	Impedance-based Stability Criterion . . . . .	106
5.2	Steady-state Operation Points from Viewpoint of Power Balance	108
5.3	Current or Voltage Driven Subsystems of Single Source Multiple Loads . . . . .	114
5.4	Illustrative Example: Single-Current-Source Two-Load System . . . . .	118
5.4.1	Inductive power transfer converter . . . . .	118
5.4.2	Experimental Evaluation . . . . .	122
5.4.3	Output Resistance of the SSIPT Converter . . . . .	124
5.4.4	Input Resistance of Load Converters . . . . .	124
5.4.5	Stability Verification of the Single-Current-Source-Two- Load System . . . . .	126
5.5	Summary . . . . .	129

<b>6</b>	<b>Conclusions and Suggestions for Future Research</b>	<b>131</b>
6.1	General Conclusions . . . . .	131
6.2	Contributions of This Thesis Work . . . . .	133
6.3	Suggestions for Future Work . . . . .	134
	<b>Bibliography</b>	<b>136</b>

# List of Figures

1.1	Qi-compatible consumer electronics: (a) Samsung Galaxy S8, (b) Hama wireless charging power bank, (c) Philips DiamondClean toothbrush. Rezenca-compatible consumer electronics: (d) Incipio wireless charging case, (e) Motorola Moto 360 smart watch, (f) Qualcomm Toq headset. . . . .	7
1.2	An artificial heart with IPT system [1]. . . . .	8
1.3	(a) A stationary EV charging system developed by INTIS [2], (b) A dynamic EV charging system developed by ORNL [3]. . . . .	9
1.4	Construction of (a) circular pad (CP), (b) double-D pad (DDP) [4].	11
1.5	Construction of (a) double-D quadrature pad(DDQP), (b) bipolar pad (BPP) [5]. . . . .	12
2.1	The four basic compensation topologies of IPT system (a) SS compensation. (b) SP compensation. (c) PS compensation. (d) PP compensation. . . . .	23
2.2	Circuit of (a) SSIPT converter. (b) SPIPT converter. . . . .	23
2.3	Equivalent circuit model of (a) SSIPT converter. (b) SPIPT converter. . . . .	24
2.4	Comparison of maximum efficiency versus load quality factor between SSIPT converter and SPIPT converter. Simulation parameters are $Q_P = Q_S = 150$ . . . . .	28

2.5	Comparison of maximum efficiency versus $k$ between SSIPT converter and SPIPT converter. Simulation parameters are $Q_P = Q_S = 150$ . . . . .	28
2.6	Current transfer function of (a) SS, (c) SP, (e) PS, and (g) PP compensated IPT converters. Voltage transfer function of (b) SS, (d) SP, (f) PS, and (h) PP compensated IPT converters. . . . .	33
2.7	Operating frequencies versus $\mu$ for (a) achieving load-independent output and maximum efficiency for secondary series compensation, and (b) achieving load-independent output and maximum efficiency for secondary parallel compensation. The intersection points are indicated with upward arrows. . . . .	35
3.1	Typical charging profile for a Li-ion battery cell [6]. . . . .	38
3.2	Comparison of efficiency $\eta$ versus $Q_L$ operating at $\omega_S$ (CC mode) and $\omega_H$ (CV mode) for various $k$ by using the model of (a) constant IPT transformer winding resistance and (b) constant IPT transformer winding quality factor. . . . .	42
3.3	Comparison of $Q_L$ versus $k$ at peak efficiency operating at $\omega_S$ (CC mode) and $\omega_H$ (CV mode). Both models of constant IPT transformer winding resistance and constant IPT transformer winding quality factor give near identical result. . . . .	44
3.4	Comparison of $\eta_{\max}$ vs. $k$ operating at $\omega_S$ (CC mode) and $\omega_H$ (CV mode) using model of (a) constant IPT transformer winding resistance and (b) constant IPT transformer winding quality factor. . . . .	45
3.5	Efficiency comparison of SSIPT converter operating at $\omega_H$ (CV mode). (a) Peak efficiency vs. $\mu$ ; (b) efficiency vs. $Q_L$ . . . . .	46
3.6	Efficiency comparison of SSIPT converter operating at $\omega_P$ (CC mode). (a) peak efficiency vs. $\mu$ ; (b) Efficiency vs. $Q_L$ . . . . .	47

3.7	Plots of (a) $\Delta g$ and (b) $\Delta e$ vs. $Q_L$ . . . . .	50
3.8	Input phase angle vs. $Q_L$ for (a) CC mode; (b) CV mode of operation. . . . .	52
3.9	Main circuit and control scheme. . . . .	53
3.10	(a) Piecewise-linear battery charging profile; (b) piecewise-linear resistance of the battery during the whole charging profile. . . . .	56
3.11	Charging efficiency $\eta$ profile for different values of $Q_n$ . Overall efficiency should be maximum at a particular $Q_n$ denoted as $Q_{n,o}$ . . . . .	57
3.12	Design plot of $Q_{n,o}$ vs. $k$ (red), and corresponding $\max(\eta_{\text{overall}})$ (blue), showing that $\max(\eta_{\text{overall}})$ increases with increasing $k$ , $Q_P$ and/or $Q_S$ . . . . .	57
3.13	Circular unipolar coupled transformer with constant inner and outer radii and evenly distributed wire distance for (a) $N = 10$ , (b) $N = 20$ and (c) $N = 40$ . . . . .	58
3.14	Coupling coefficient $k$ and inductance $L_S$ (or $L_P$ ) vs. number of turns $N$ . . . . .	59
3.15	Experimental prototype of the IPT system. . . . .	63
3.16	Waveforms of $v_{AB}$ , $i_P$ and $I_O$ at (a) start and (b) end of CC charging mode of the IPT converter designed with $\mu = 1$ . . . . .	65
3.17	Waveforms of $v_{AB}$ , $i_P$ and $I_O$ at (a) start and (b) end of CC charging mode of the IPT converter designed with $\mu = 0.96$ . . . . .	66
3.18	Waveforms of $v_{AB}$ , $i_P$ and $I_O$ at (a) start and (b) end of CV mode of charging of the IPT converter designed with $\mu = 1$ . . . . .	67
3.19	Waveforms of $v_{AB}$ , $i_P$ and $I_O$ at (a) start and (b) end of CV mode of charging of the IPT converter designed with $\mu = 0.96$ . . . . .	68
3.20	Measured charging efficiency $\eta$ versus load quality factor $Q_L$ . . . . .	69
3.21	Measured charging efficiency $\eta$ versus time $t$ . . . . .	70

3.22	Loss components estimation. (a) Illustrative voltage and current waveforms at the two phase legs of the H-bridge. (b) Measured charging efficiency $\eta$ versus duty cycle $D$ with LIC operation with $\mu = 1$ . The LIC output is regulated by varying $D$ to provide the required constant output current for CC mode and the required constant output voltage for CV mode. (c) Estimated loss components versus $D$ , where $P_{\text{Switch}} = P_{\text{SwitchOn}} + P_{\text{SwitchOff}}$ . . . . .	71
3.23	Measured charging profiles of voltage $U_C$ and current $I_C$ . . . . .	72
4.1	SSIPT converter cascaded with a front-side converter and a load-side converter. . . . .	78
4.2	Schematic of the system. . . . .	82
4.3	Simulated frequency response of transconductance of the SSIPT model. Parameters used in simulation are: $L_P = L_S = 30 \mu\text{H}$ , $C_P = C_S = 21.11 \text{ nF}$ , $R_P = R_S = 0.5 \Omega$ , $\frac{\omega}{2\pi} = 200 \text{ kHz}$ , $v_i = 30\text{V}$ and $P_O = 60\text{W}$ . . . . .	88
4.4	Block diagram of the voltage control loop of the cascaded buck-SSIPT converter system. . . . .	89
4.5	(a) Frequency response of $\hat{v}_{\text{err}}$ versus $\hat{d}$ . (b) Locations of pole (marked with 'x') and zero (marked with 'o') of the system with $K_P = 0.01$ , $K_I = 0.5$ , when $k$ increases from 0.1 to 0.3 as indicated by the arrow direction. Simulation parameters of the SSIPT converter are $L_P = L_S = 30 \mu\text{H}$ , $C_P = C_S = 21.11 \text{ nF}$ , and $\frac{\omega}{2\pi} = \frac{\omega_P}{2\pi} = \frac{\omega_S}{2\pi} = 200 \text{ kHz}$ . Parameters of the buck converter are $L_a = 1.2 \text{ mH}$ , $C_a = 760 \mu\text{F}$ , $V_{\text{IN}} = 50 \text{ V}$ , $V_O = 30 \text{ V}$ , and $R = 20 \Omega$ . . . . .	91
4.6	Experiment setup of the system and enlarged image of the loosely coupled transformer. . . . .	92

4.7	Measured efficiency of SSIPT converter versus output power under various voltage gains at (a) $k = 0.1739$ , (b) $k = 0.2541$ . . . . .	94
4.8	Measurements of the frequency response of input duty cycle to voltage error of the SSIPT at (a) $k = 0.1739$ , (b) $k = 0.2541$ . . . . .	96
4.9	Transient waveforms of key control parameters of voltage error control with $g$ dynamically changing (a) from 25 mm to 45 mm, (b) from 45 mm to 25 mm. The load resistance $R$ is 10 $\Omega$ . . . . .	97
4.10	Transient waveforms of key control parameters of an implementation of the minimum input current P&O control with $g$ dynamically changing (a) from 25 mm to 45 mm, (b) from 45 mm to 25 mm. The loading condition is $R$ is 10 $\Omega$ . . . . .	98
4.11	Transient waveforms of voltage tracking processes for $R$ switching from 55 $\Omega$ to 10 $\Omega$ and from 10 $\Omega$ to 55 $\Omega$ at (a) $k = 0.1739$ , (b) $k = 0.2541$ . . . . .	100
4.12	Transient waveforms of (a) voltage error control, and (b) minimum input current P&O control. At $t_1$ , the control is executed. At $t_2$ , load resistance $R$ is switched from 30 $\Omega$ to 10 $\Omega$ . $k$ is 0.1739. . . . .	101
5.1	Impedance-based models of a source converter $S_1$ and $n$ load converters $W_1, \dots, W_n$ . Components inside the dotted line blocks are the small-signal-equivalent circuit of the converters. (a) Voltage source converter $S_1$ sharing a common voltage with $n$ load converters. (b) Current source converter $S_1$ sharing a common voltage with $n$ load converters. (c) Voltage source converter $S_1$ sharing a common current with $n$ load converters. (d) Current source converter $S_1$ sharing a common current with $n$ load converters. . . . .	109

5.2	DC operation models of a source converter $S_1$ and a load converter $L_1$ . Components inside the dotted line blocks are the DC-equivalent circuit of the converters. (a) Voltage source converter $S_1$ sharing a common voltage with a load converter. (b) Current source converter $S_1$ sharing a common voltage with a load converter. . . . .	110
5.3	Constant power curve with biasing points A, B and C. . . . .	111
5.4	Power transfer characteristic of a voltage-source system. . . . .	112
5.5	Power transfer characteristic of a current-source system. . . . .	113
5.6	DC circuit models of four possible configurations consisting of a source converter $S_1$ and two load converters $W_1$ and $W_2$ . . . . .	115
5.7	Block diagram of the single-current-source-two-load system. . . . .	119
5.8	Basic PWM voltage converters. . . . .	120
5.9	Basic PWM current converters. . . . .	120
5.10	Schematic of the single-current-source-two-load subsystems. . . . .	121
5.11	Output characteristics of $S_1$ . (a) Steady-state output current $I_O$ versus load resistance $R_L$ . (b) Small signal response of output impedance. . . . .	123
5.12	Measured input VI steady-state characteristics of PWM converters $W_1$ and $W_2$ . The dotted constant power curves fit well with the input powers 33.75 W of $W_1$ and 6.43 W of $W_2$ . . . . .	124
5.13	Measured input impedances of PWM converters. . . . .	125
5.14	Measured magnitude of impedance ratio for object based stability verification of local stability within the bandwidth from 0 Hz to 1 kHz for converters (a) $S_1$ using (C3a), (b) $W_1$ using (C3a), and (c) $W_2$ using (V3a). . . . .	127

- 5.15 Step response of the system. (a) Sudden reduction of the output reference current  $I_{\text{Ref1}}$  of  $W_1$  leading to a reduction of input voltage  $V$ , a characteristic of a current source system. Traces  $U_{O1}$  and  $I_{O1}$  are the output voltage and current of  $W_1$ . Trace  $R_{W1}$ , input resistance of  $W_1$ , is calculated based on measured data, using  $R_{W1} = \frac{V^2}{U_{O1}I_{O1}}$ , where the loss of the converter is ignored. (b) Sudden reduction of the output voltage reference  $U_{\text{Ref2}}$  of  $W_2$ , leading to an increment of  $V$ , a characteristic of a voltage source system. Traces  $U_{O2}$  and  $I_{O2}$  are output voltage and current of  $W_2$ . Trace  $R_{W2}$  is the input equivalent resistance of  $W_2$ , calculated using  $R_{W2} = \frac{V^2}{U_{O2}I_{O2}}$ , where the loss of the converter is ignored. . . . . 128
- 5.16 System in response to the cold start of  $W_2$ . Traces  $I_1$  and  $I_{O1}$  are the input and output currents of  $W_1$ . Traces  $V$  and  $U_{O2}$  are the input and output voltages of  $W_2$ . . . . . 129



# List of Tables

2.1	Summary of LIC and LIV . . . . .	31
2.2	Summary of Operating frequencies $\omega_M$ , $\omega_{LIC}$ and $\omega_{LIV}$ . . . . .	32
3.1	Cases of Implementation . . . . .	40
3.2	Charging Parameters . . . . .	55
3.3	Design Specification . . . . .	61
3.4	Comparison of Calculated and Measured Transformer and Circuit Parameters . . . . .	62
4.1	Comparison of Different control schemes . . . . .	81
4.2	Components and Parameters of the System . . . . .	92
4.3	$k$ -independent Converter Transfer Function at Maximum Efficiency	102
5.1	Parameters of Converters . . . . .	122



# Abbreviations List

WPT	Wireless Power Transfer
IPT	Inductive Power Transfer
MWPT	Microwave Wireless Power Transfer
LWPT	Laser Wireless Power Transfer
EV	Electric Vehicle
CPT	Capacitive Power Transfer
CP	Circular Pad
DDP	Double-D Pad
DDPQ	Double-D PAD With A Quadrature Coil
BPP	Bipolar Pad
SSIPT	Series-Series Compensated Inductive Power Transfer
LIC	Load-independent Current
LIV	Load-independent Voltage
ZVS	Zero Voltage Switching
P&O	Perturb and Observe
CC	Constant Current
CV	Constant Voltage



# Nomenclature List

Unless otherwise specified, some commonly-used symbols in the thesis are defined as follows.

Symbol	Description
$\omega$	Operating angular frequency of the IPT converter
$\omega_{LIC}$	Operating angular frequency of the IPT converter to achieve load-independent current output
$\omega_{LIV}$	Operating angular frequency of the IPT converter to achieve load-independent voltage output
$\omega_M$	Operating angular frequency of the IPT converter to achieve maximum power efficiency
$\omega_P$	Resonant angular frequency of primary resonant network
$\omega_S$	Resonant angular frequency of secondary resonant network
$\mu$	The ratio of $\omega_P$ to $\omega_S$ , $\frac{\omega_P}{\omega_S}$
$L_P$	Inductance of the transformer primary winding
$L_S$	Inductance of the transformer secondary winding
$C_P$	Capacitance of primary resonant network
$C_S$	Capacitance for secondary resonant network
$M$	Transformer mutual inductance
$k$	Coupling coefficient
$R_P$	Winding resistance of the transformer primary winding
$R_S$	Winding resistance of the transformer secondary winding
$R_{battery}$	Equivalent DC resistance of the battery determined by charging voltage and charging current

Symbol	Description
$R$	Load resistance of the system
$R_L$	Equivalent AC load resistance of the IPT converter
$R_{L,opt}$	Optimum $R_L$ to achieve maximum efficiency
$Q_P$	Quality factor of the transformer primary winding
$Q_S$	Quality factor of the transformer secondary winding
$Q_L$	Load quality factor
$Q_{L,M}$	Optimum load quality factor to achieve maximum efficiency
$Q_{LCC}$	Optimum load quality factor of the SSIPT converter to achieve maximum efficiency at LIC
$Q_{LCV}$	Optimum load quality factor of the SSIPT converter to achieve maximum efficiency at LIV
$Q_n$	Load quality factor at the point of switch-over from CC to CV charging
$Q_{n,o}$	Optimum $Q_n$ to achieve maximum overall efficiency of the charging profile
$Z_P$	Impedance of the primary resonant network
$Z_S$	Impedance of the secondary resonant network including the load resistance
$Z_r$	Reflected impedance of $Z_S$ from the secondary to the primary
$\eta$	Power efficiency of the IPT converter
$\eta_{max}$	Maximum power efficiency of the IPT converter
$\eta_{maxCC}$	Maximum power efficiency of the SSIPT converter at LIC
$\eta_{maxCV}$	Maximum power efficiency of the SSIPT converter at LIV
$\eta_{overall}$	Overall efficiency for the whole charging profile
$v_i$	Input voltage vector of the IPT converter
$i_i$	Input current vector of the IPT converter
$i_P$	Current vector of the primary winding
$i_S$	Current vector of the secondary winding
$v_o$	Output voltage vector of the load
$i_o$	Output current vector of the load

Symbol	Description
$G$	Current transfer function
$E$	Voltage transfer function
$G_i$	Ideal current transfer function
$E_i$	Ideal voltage transfer function
$G_{LIC}$	Magnitude of load-independent current transfer function
$E_{LIV}$	Magnitude of load-independent voltage transfer function
$\Delta g$	Normalized error between ideal current transfer ratio and practical current transfer ratio of the SSIPT converter
$\Delta e$	Normalized error between ideal voltage transfer ratio and practical voltage transfer ratio of the SSIPT converter
$Z_{in}$	Input impedance of the SSIPT converter
$\theta_{in}$	Input phase angle of the SSIPT converter
$\theta_{CC}$	Input phase angle of the SSIPT converter at LIC
$\theta_{CV}$	Input phase angle of the SSIPT converter at LIV
$d_o$	Outer diameter of the circular coil
$d_i$	Inner diameter of the circular coil
$g$	Air gap distance
$N_P$	Number of the turns of the primary winding
$N_S$	Number of the turns of the secondary winding
$D_i$	Duty cycle of the SSIPT converter at LIC
$D_v$	Duty cycle of the SSIPT converter at LIV
$V_{err}$	Voltage error between input voltage and output voltage of the SSIPT converter
$G_{verr}$	Voltage error transfer function
$T_v$	The ratio of the output impedance of the source to the input impedance of the load
$T_c$	The ratio of the input impedance of the load to the output impedance of the source



# Chapter 1

## Introduction

### 1.1 Motivation

Over a century ago, Nicola Tesla successfully carried out a wireless power transfer (WPT) experiment in which a lamp was wirelessly powered [7]. Since that, both radiative and non-radiative WPT technologies have been in progress with the efforts of many researchers and their technological attempts [8–17]. In addition, emerging applications and markets are also driving the development of WPT, because of its benefits of wireless connectivity. Nowadays, non-radiative WPT via magnetic field coupling, also called inductive power transfer (IPT), has attracted many attentions in a widespread applications, from low-power to high-power, from short-distance to mid-distance and from stationary to dynamic, with the following advantageous features:

1. It is user-friendly. Since there is no physical contact in IPT systems, the hassle and unsafety from connecting electrical cables can be removed. Without actions of plug/unplug to provide physical path, IPT systems can be activated autonomously, which brings great convenience to users and maximizes charging opportunities.

2. It improves product reliability. The transmitter and receiver coils of the IPT systems are usually water proof by being sealed in something or embedded somewhere. Even in hazardous environment (e.g., underwater applications), the reliability of the IPT systems is high.
3. It enhances flexibility. For applications (e.g., biomedical implants) which are inconvenient to replace batteries or connect cables for charging, it is feasible to use IPT systems for continuous power supply.
4. It realizes in-motion charging. Without constrains of electric wires, IPT systems can be extended to dynamic power supply, which can address the energy bottleneck of battery-powered devices.

However, there are still some challenges for IPT systems arised in specific applications. Power control and efficiency optimization are important to IPT systems. In stationary battery charging applications, power varies in a wide range, which is a challenge to the design of IPT systems. Power control using multi-stage and hybrid-topology IPT systems causes additional component losses, thus design of a single-topology IPT system considering power control with efficiency optimization is desired. In dynamic applications with variations of coupling coefficient and load power, multi-stage IPT systems are usually used for power control and maximum efficiency tracking. Conventional coordinate control cannot meet the requirement of fast response, thus a better linear control method should be used. In addition, as IPT systems emerge in power distribution systems, the stability should be studied. Especially, when the IPT system operates as a current source with high impedance and the similar configuration is adopted as voltage-source power distribution system, load converters should be distinguished between current-source driven and voltage-source driven. This thesis is going to address these challenges.

## 1.2 Fundamentals of Wireless Power Transfer

Instead of using conductors to transfer power, WPT transfers power from a transmitter to a receiver over an air gap distance, by means of electromagnetic field [18, 19]. A transmitter generates high-frequency time-varying electromagnetic field by some kind of device, while a receiver uses similar kind of device to receive power. The shape of device can be a coil of wire, a metal plate or an antenna. In far-field region, the electric and magnetic fields are perpendicular to each other and propagate as an electromagnetic wave carrying power. Power is transferred in form of electromagnetic radiation. In near-field region, we should restrict our consideration to an electric field or a magnetic field alone. Power can be capacitively coupled in electric field or inductively coupled in magnetic field. According to power transfer mechanisms, literature review is classified into three categories:

### 1.2.1 Electromagnetic Radiation

Microwave and laser are two forms of electromagnetic radiation used for wireless power transfer.

In a typical microwave wireless power transfer (MWPT) system, an unidirectional power beam of microwave generated by a dish-like antenna travels through the atmosphere and is received by another antenna. Due to diffraction, to reduce the power wasted in the free space, larger antennas or shorter wavelength (i.e., higher frequency) are necessary to achieve sufficiently directional microwave beam. MWPT systems have been studied in space applications. The concept of Solar Power Satellite (SPS) was first introduced by Glaser in [20] that placing a satellite in stationary orbit to wirelessly transfer energy harvested in outer space to the receiver on earth by microwave. More researches have been carried out to study the feasibility of building SPSs [15, 21–23]. MWPT systems have also been

studied for mid-range electric vehicle (EV) charging [24,25], and 10 KW MWPT prototype for EV charging with over 80% efficiency was also implemented by researchers in Kyoto University.

Basic concept of laser wireless power transfer (LWPT) is the same as photovoltaic power generation. Benefiting from advanced technology in both solid-state lasers and photovoltaic cells, by converting electricity into laser beam and pointing to a remote photovoltaic receiver, LWPT system is closer to practice [26,27]. Compared with the microwave, laser beam has higher energy density, thus LWPT systems are studied for high power applications, like future space elevator [28]. Moreover, due to compact device size and flexible installation [29], LWPT systems can also be applied in power supply for mobile devices (e.g., sensor networks) [30].

### 1.2.2 Capacitive Power Transfer

Capacitive Power Transfer (CPT) is power transfer by electric field using capacitive coupling. In a CPT system, the transmitter and the receiver electrodes, usually metal plates, form a capacitor, with the air gap as the dielectric. An alternating voltage source is applied to the transmitter plate to generate oscillating electric field, and the receiver plate gets the power by electrostatic induction. The power transfer capability increases with the capacitance, the frequency and the intensity of the capacitor's voltage that produces the electric fields [31]. Due to the limitation of the size and low permittivity of air gap, the capacitance is usually very low. To improve the power transfer capability, the frequency or the voltage intensity should be increased. However, higher switching frequency will increase the power loss and higher electric field will result in significant safety concerns [32,33]. Therefore, most of the CPT systems are usually designed for low power applications, for example, integrated chips,

portable devices, small robots and so on [34–38]. Nevertheless, since the size of EV is relatively large, sufficient large capacitance can be designed for high power transfer. Some studies have been carried out high power CPT systems for EV charging, with relatively large air gap distance and high power efficiency [39–41].

### 1.2.3 Inductive Power Transfer

Inductive Power Transfer (IPT) transfers power by magnetic field using inductive coupling. In an IPT system, the transmitter and the receiver coils of wire form a transformer. An alternating current source is applied to the transmitter coil to generate oscillating magnetic field, and the receiver coil gets the power by magnetic induction. The power transfer capability increases with the mutual inductance, the frequency and the intensity of the conductors current that produces the magnetic fields. The mutual inductance depends on coupling coefficient of the coils, which decreases significantly as the air gap distance increases. To increase the power transfer capability, two coils of wire are usually in a short distance.

Resonant inductive coupling is a form of inductive coupling in which power is transferred by magnetic fields between two resonant circuits, one in the transmitter and one in the receiver. Compared with ordinary non-resonant inductive coupling, resonant inductive coupling has higher efficiency by using resonant circuit and therefore has greater transfer distance than non-resonant inductive coupling [42]. The principle behind resonant inductive coupling is that energy transfer is efficient in a system of coupled resonance [43, 44]. A well known experiment by MIT researchers has demonstrated this theory [44]. Both coupled mode theory [42, 44–46] and circuit theory [47–50] have been widely used to studied resonant inductive coupling.

The following chapters will focus on modern IPT systems using resonant

inductive coupling techniques.

## 1.3 Applications of IPT systems

IPT systems of different power levels can be designed to transfer power efficiently over an air gap from short-distance to mid-distance. Due to the elimination of physical electric contacts, IPT systems are suitable for wireless power transfer in not only clean environments but also hazardous (e.g. wet, dirty) environments [51, 52]. The IPT systems are relatively safe to human body, because the power is transferred by magnetic field, which interacts with human body very weakly compared with electric field. The advantages of IPT systems are safety, reliability, maintenance free, and long product life. IPT systems are suitable for both static and dynamic applications. Some of the applications will be discussed below.

### 1.3.1 Consumer Electronics

In 21st century, more and more consumer electronics emerge and benefit us in many aspects of our life, such as entertainment (e.g., music player), communication (e.g., mobile phone), health care (e.g., e-toothbrush) and office work (e.g., laptop). Each charger of the consumer electronics usually comes with a long cable connecting to the power socket, which takes up a lot of space and has poor mobility. To eliminate the inconvenient cables, IPT systems are developed for battery charging of consumer electronics. The transmitter coils of an IPT system are usually designed as planar platform [53–58], which is space-saving when embedded into the desk or wall. More than one consumer electronics, each of which has its own receiver coils, can be placed on the planar platform freely and charged simultaneously [59–63]. Such planar IPT charging platforms usually have abilities to locate the positions, identify the compatibility and monitor the condition of the loads.

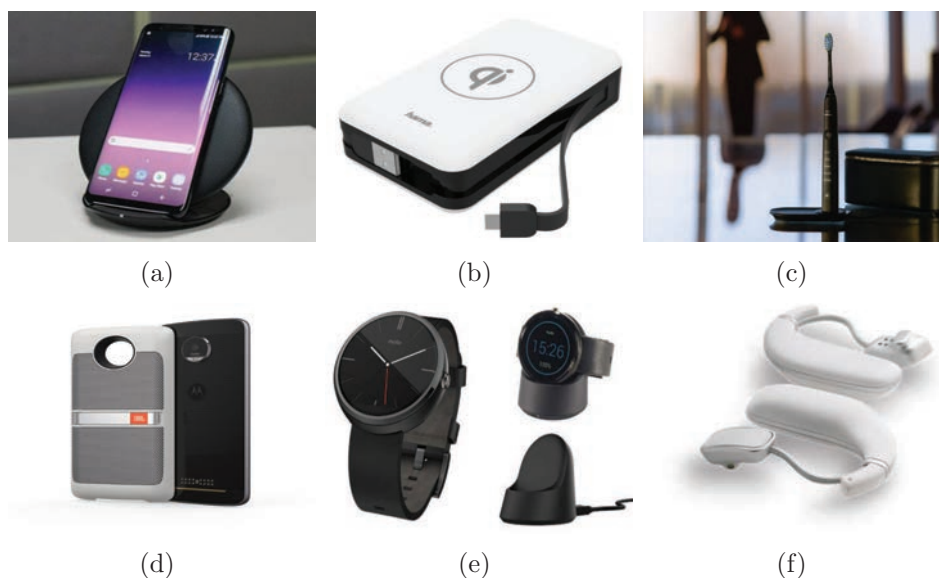


Figure 1.1: Qi-compatible consumer electronics: (a) Samsung Galaxy S8, (b) Hama wireless charging power bank, (c) Philips DiamondClean toothbrush. Rezencc-compatible consumer electronics: (d) Incipio wireless charging case, (e) Motorola Moto 360 smart watch, (f) Qualcomm Toq headset.

IPT technologies for battery charging of consumer electronics have been widely commercialized. Qi [64] and Rezencc [65] are two major wireless charging standards, both of which are supported by over 200 industrial companies. Fig. 1.1 shows some Qi-compatible and Rezencc-compatible consumer electronics.

### 1.3.2 Biomedical Implants

Biomedical implants are the man-made devices and structures inserted into the body of the patients to improve the quality of life, by simulating internal organs, monitoring internal vital signs and delivering drugs. Most of these biomedical implants contain electronic circuits and the power requirement typically ranges from a few microwatts [66–69] to a few tens of milliwatts [70–73]. It is a challenge to provide reliable power supply to the biomedical implants, because of size limitation and inaccessibility of the battery. In addition, it is dangerous, unconformable and costly to replace the biomedical implants by surgery, if the batteries are depleted. IPT is an effective power supply approach for

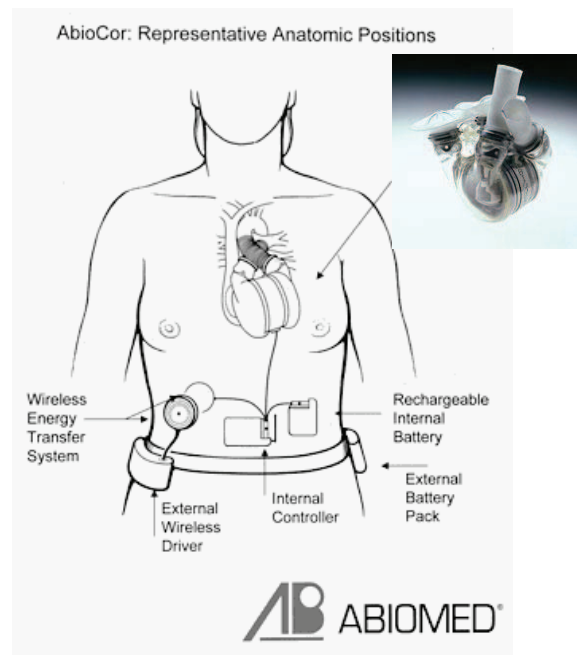


Figure 1.2: An artificial heart with IPT system [1].

biomedical implants [74]. Typically, receiver coils are implanted inside the body to receive power from the external transmitter coils. With IPT systems to provide continuous power for the biomedical implants, the battery can be miniaturized or even eliminated. Nowadays, IPT systems are widely studied to implement in different biomedical implants, such as artificial organs [75–78], neurostimulation systems [79, 80], drug delivery systems [81] and so on. Fig. 1.2 shows a total artificial heart, called AbioCor, which successfully worked in human body in 2001 [1]. This artificial heart was powered by a rechargeable battery, which is continuously charged by an IPT system. However, further development of this artificial heart has been terminated due to insufficient evidence of its biological efficacy.

### 1.3.3 Electric Vehicles

Electric vehicle (EV) has been more and more attractive to consumers in the last decade, because it can eliminate exhaust emissions and cure our addiction to



Figure 1.3: (a) A stationary EV charging system developed by INTIS [2], (b) A dynamic EV charging system developed by ORNL [3].

gasoline. Moreover, EVs have better user experience and lower maintenance cost [82, 83]. However, the conventional wired EV chargers cannot offer convenience and reliability of EVs, which is a drawback of EV especially in hazardous environments. Aside from wired chargers, the size of onboard EV battery is also a bottleneck because of low energy density and high cost of Lithium-ion batteries, which limits long-distance mobility of EVs. Prospecting to improve convenience, reliability and mobility of the EVs [84, 85], IPT systems are developed for EV charging. Without physical connections, IPT systems are suitable for stationary EV charging. Once parked over the transmitter coils with good alignment, EVs can be charged efficiently. Fig. 1.3(a) shows a 30 kW stationary EV charging system developed by INTIS company [2]. Some other IPT systems for stationary EV charging have been studied in [52, 86–91]. If IPT systems are incorporated into the roadway, EVs can get power directly while moving. As an example, Fig. 1.3(b) shows a prototype of dynamic EV charging system developed by Oak Ridge National Laboratory (ORNL) [3]. It can further downsize the onboard EV battery, shorter dedicated charging time and unlimited driving range capability. Some other IPT systems for dynamic EV charging have been studied in [92–98].

### 1.3.4 Other applications

Besides the aforementioned, IPT can be used in many other applications. In some industrial manufacturing systems, such as machine tools [99] and robot manipulators [100, 101], frequent reconfiguration is required. IPT systems can provide more freedom in reconfiguration, due to reliable power and data transfer without physical contacts. IPT systems have also found applications in wireless lighting [102–104], which can save the cables, plugs and sockets. In underwater environment, where plugged connectors are impractical, it is a feasible way to use IPT systems to charge underwater vehicles wirelessly [105–107]. Novel Domino [108] IPT systems also find applications in power grid, where Domino resonators are embedded in insulation discs to provide high-voltage insulation and wireless power transfer capability [109]. It is believed that more and more potential applications are to be exploited.

## 1.4 Literature Review

### 1.4.1 Coupler Design

In IPT systems, power is inductively coupled from a pair of coils, which are usually called transmitter pad and receiver pad, over an air gap distance. To increase the coupling, coil topologies in transmitter pad and receiver pad are widely studied. Unipolar coil and bipolar coil are two basic forms of coils. Unipolar coil is intuitively derived from pot core transformer [110–114], and it is characterized by the presence of only one magnetic pole in each coil surface. Coil geometry of unipolar coil can be circular and square. A widely studied and common used circular pad (CP) is shown in Fig. 1.4(a) [115–117]. Besides the circular coil, CP also has a ferrite layer to guide the magnetic flux and a shielding layer to reduce the leakage magnetic field [117]. A bipolar coil characterized by the presence of

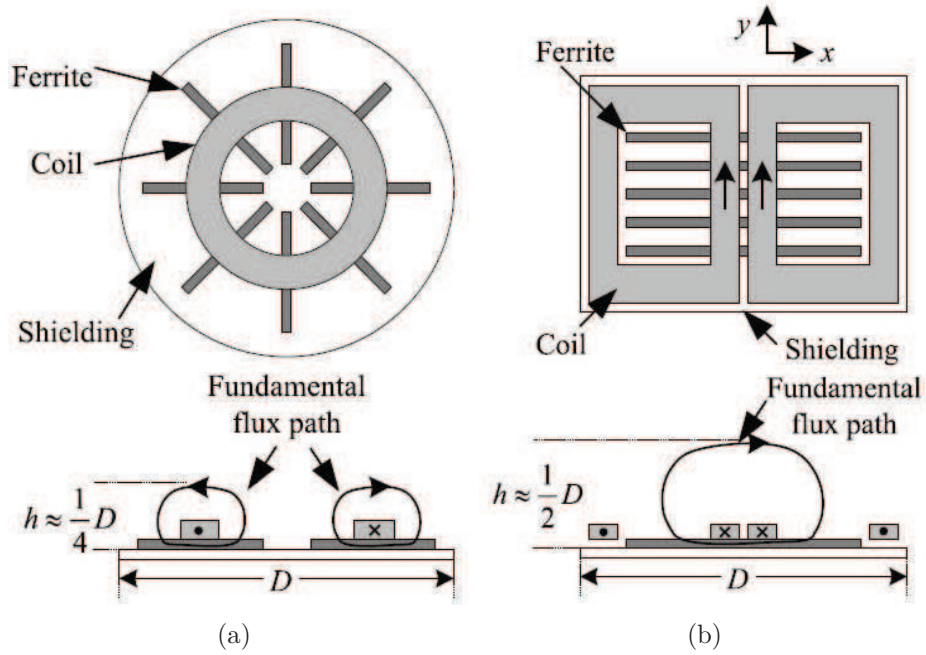


Figure 1.4: Construction of (a) circular pad (CP), (b) double-D pad (DDP) [4].

two magnetic poles in a single coil surface. Fig. 1.4(b) shows a pad, called double-D pad (DDP), where the bipolar coil is made of two regular coils electrically connecting to each other and generating opposite magnetic polarities. The layout of ferrite layer and shielding layer of DDP is similar to that of CP [88, 118]. A fundamental flux path concept is proposed in [88, 119] to study the relationship between the size of a transmitter coil and its ability to throw magnetic flux to a receiver coil. The fundamental flux path height is approximately one quarter of the pad diameter for CP, while the flux path height is approximately half of the pad diameter for DDP. Therefore, DDP has significant improved performance of magnetic coupling compared with CP in similar size.

From Fig. 1.4, as a receiver pad, CP only captures vertical flux, while DDP only captures horizontal flux [5]. DDP has poor position tolerance in  $x$ -axis due to the decrease of horizontal flux with the misalignment and there is a null coupling point under a certain horizontal misalignment in  $x$ -axis [118]. To improve the position tolerance, the work in [88] proposed adding a quadrature unipolar coil

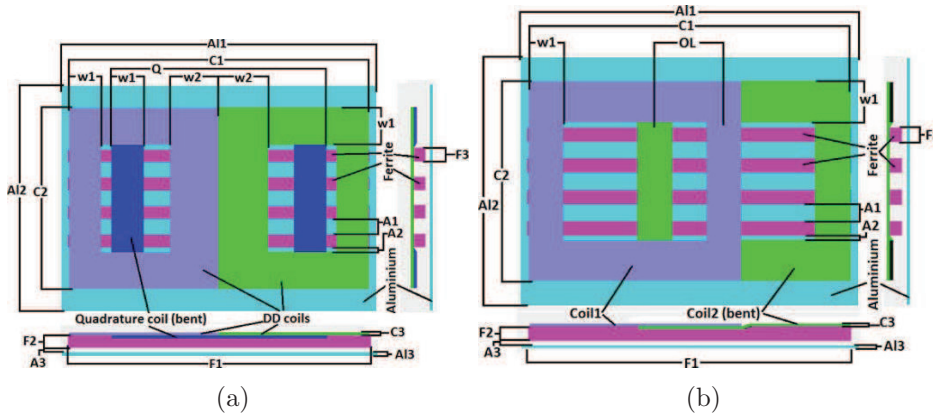


Figure 1.5: Construction of (a) double-D quadrature pad(DDQP), (b) bipolar pad (BPP) [5].

to existing DDP as shown in Fig. 1.5(a), which is named DDPQ. It has better coupling performance because two consisted pads can work together to capture both vertical flux and horizontal flux. It has been shown that a DDP-DDQP coupler provides a charge zone three times larger than a DDP-DDP coupler and five times larger than that of a CP-CP coupler [88]. Another design called bipolar pad (BPP) is proposed in [120], which consists of two identical, partially overlapped and mutually decoupled coils as shown in Fig. 1.5(b). BPP matches the performance of DDQP as a secondary pad, but with the advantage of using less copper [120]. The interoperability characteristics of DDP, DDQP and BPP are further studied in [5,121], which demonstrates that DDQP and BPP perform better than CP and DDP, but at the cost of making the design and control more complicated.

Charging platform is widely used in applications of consumer electronics because it supports more than one electronic loads and allows them to be placed freely within the charging area [53, 58, 63]. The charging platform is formed by extending a single unipolar coil into a coil array structure [54, 122, 123]. Magnetic flux flows vertically out of the charging surface and the secondary coil can be placed anywhere to pick up power regardless of its position. Nowadays, lumped IPT systems are also used in RPEVs as an alternative to the long power supply

rail scheme [97]. Coil topologies are preferred to be selected from DDQP and BBP because of better coupling and tolerance to misalignment as mentioned above [124]. A large number of small transmitter pads are laid down under the road [125]. With segmentation switching technique, only the transmitter pads covered by the receiver pad are excited to transfer power.

### 1.4.2 Compensation Network

Compensation networks are usually used to tune the transmitter coil and the receiver coil, forming a resonant circuit in the transmitter side (also called primary side) and a resonant circuit in the receiver side (also called secondary side). Researches in design of the compensation network and the operating frequency are different, depending on the requirements of the IPT converters:

1. Maximize power transfer capability and minimize voltage-ampere (VA) rating. IPT converters are design to operate at secondary resonant frequency to achieve maximum power transfer capability [126, 127]. In the primary, the compensation networks are designed to have zero phase angle (ZPA) and minimize VA rating [126, 128, 129]. IPT converters may have more than one operating frequency to have ZPA, which is related to compensation network, loading condition and variable frequency control. Variable frequency control may have bifurcation phenomenon which should be avoided to ensure the control stability. [126, 130–132].
2. Achieve load-independent current (LIC) or load-independent voltage (LIV) output. Conventionally, IPT converters are controlled to have constant current or voltage output, at the cost of wide range input modulation or frequency modulation, which usually leads to efficiency compromission. Therefore, native load-independent output characteristic is desired in IPT converters [133–135]. LIC [136] and LIV [137] of Series-Series and Series-

Parallel compensated IPT converters are firstly studied and compared. Some IPT converters with higher order compensation networks are also studied to achieve load-independent output, such as LCC-LCC [138], Series/Series-Parallel [139], LCL Series-Parallel [130] and so on. With a more general method introduced in [140], compensation networks can be derived to achieve load-independent characteristics.

3. Optimize the efficiency. It shows that maximum achievable efficiency of IPT converters only depends on the coupling coefficient and the quality factor of the windings, if well compensated [136]. IPT converters can be further optimized by facilitating soft switching (i.e., zero voltage switching (ZVS) for MOSFET drivers and zero current switching (ZCS) for IGBT drivers). Input phase angle of of the IPT converters can be slightly adjusted by designing the compensation network and choosing the operating frequency, to achieve ZVS and ZCS [134, 135, 141, 142].
4. Designed to be robust to coupling variation. IPT converters are desired to operating against coupling variation which usually occurs due to misalignment of the couplers. Some design approaches of the compensation network are studied, which makes the IPT converters insensitive to coupling variation [143, 144]. With well design compensation network and operating frequency control, coupling-independent LIV of the Series-Series IPT converter is also achieved [145, 146].

### 1.4.3 Control

In a typical IPT converter, a full-bridge converter is usually used to generate an AC voltage source and drive the primary resonant circuit. Alternating magnetic field generated by the primary side induces alternating current in the secondary side. A secondary full-bridge rectifier converters alternating current into direct

current output. Some control methods are discussed as below

1. Frequency modulation. As a resonant converter, frequency modulation of the full bridge inverter can regulate the output power [75, 147–149]. Bifurcation phenomenons and related instability issues have been reported when frequency control is performed to track the ZPA of the input voltage and current [52, 126]. Frequency modulation may be restricted to a limited frequency bandwidth, due to the electromagnetic safety issue [150]. The efficiency of IPT converters decreases significantly when the operating frequency shifts away from the resonant frequency [151].
2. LIC and LIV control. As discussed in Section 1.4.2 , the IPT converters can operate at load-independent frequencies to achieve LIC and LIV. However, the operating frequencies are usually related to coupling coefficient. Therefore, when there is position variation of the coupler, operating frequency should be adjusted to match load-independent frequency. Self oscillating and phase lock loop control are used to track the operating frequency of an SSIPT converter to achieve LIV [145, 146]. Phase shift PWM control can also be implemented to regulate the output, but the regulation depth is usually restricted by a soft switching region [134].
3. Topology switching control. IPT converters should be tuned perfectly under different coupling conditions and load conditions. When the operating frequency is fixed, variable inductors [152] and switchable capacitors [153, 154] are usually used to keep the IPT converters perfectly tuned. Using this approach, the IPT converters can be adaptive to coupling variation [155] and load variation [156]. In some battery charging applications, hybrid topologies are designed for the IPT converters, where the secondary compensation networks usually can be changed by switches. LIC and LIV

thus can be achieved for constant current (CC) and constant voltage (CV) charging through switching the compensation topology [157–159].

4. Control of additional cascaded converters. Due to less freedom for control in a single-stage IPT converter, additional front-side converter or end-side converter can be cascaded to an IPT converter. If the end-side converter is independently controlled to regulate the output power, the primary can be controlled on its own regardless of the loads. Also, with a load-side converter, wireless communication can also be eliminated [160]. It is especially useful for IPT systems with multiple secondary pickups, such as roadway IPT systems [161, 162]. As mentioned above, when the IPT converters operate at LIC or LIV, the modulation depth of phase shift PWM is shadow. Therefore, a front-side converter can extend the modulation of input voltage of the IPT converter, while soft switching condition of the IPT converter can be maintained. In [163, 164], Perturb and Observe (P&O) based coordinated control is adopted in a three-stage IPT system to regulate the output power and optimize the efficiency. In [160, 165], similar P&O methods are used to track the maximum efficiency, while the load-side converter is independently controlled to regulate the output power.

#### 1.4.4 Safety

High frequency electromagnetic fields (EMF) generated by IPT systems can induce high field strength in nearby objects, including human bodies, animals and other electronic equipments. Therefore, the design of the IPT systems for different applications should meet the safety standards and guidelines for electromagnetic field exposure (e.g. ICNIR [166]). Methods to reduce EMF can be categorized into

1. Passive reduction. It is common to use high permeability materials, such

as ferrite, to guide the magnetic flux intensively, thus reducing magnetic flux in unwanted directions [88, 117, 167]. It can improve the efficiency of the IPT systems, but at the cost of expensive high conductivity materials. High conductivity materials, such as aluminum, can be also used to shield the unwanted magnetic flux by inducing eddy current. However, it usually brings additional loss to the IPT systems [168].

2. Active cancellation. Opposite magnetic flux can be generated to cancel unwanted magnetic flux by using additional systems, which usually includes coils, power source, phaser detectors and controllers [169–171].

## 1.5 Objective of the Thesis

Since there are still some challenges in practical IPT applications, the study of this thesis will focus on power control and efficiency optimization in some specific applications. The objectives of this thesis are as follow:

**Efficient single-topology IPT converter for battery charging.** For most stationary Li-ion battery charging applications, a CC charging followed by a CV charging is the preferred charging algorithm, with load power varying from the maximum rated power down to a minimum of a few percentage. To eliminate extra loss associated with multi-stage and hybrid-topology IPT system, a single-topology IPT converter should be designed to charge the battery. However, high efficiency is hard to achieve for such a wide load range. To achieve CC and CV outputs, several implementation options of a single-topology IPT converter will be first compared in this thesis. We will select the most attractive implementation case and elaborate the design with soft switching for the entire battery load range and overall efficiency optimization for the whole charging profile.

**Controller design for efficiency optimization in three-stage IPT**

**system.** Once there is large variation of the coupling coefficient or the load power, a single-stage IPT converter cannot maintain at its maximum efficiency point. A three-stage IPT system is therefore used to meet the requirement of output power regulation and maximum efficiency tracking, where an IPT converter is cascaded with a front-side converter and a load-side converter. However, conventional cooperative control of these two converters, such as P&O, is inevitably slow in response, showing poor robustness in applications requiring fast output power regulation. In this thesis, a linear control scheme based on observing the voltage ratio will be designed to track the maximum efficiency. It shows more robust than P&O control, making the three-stage IPT system more suitable for applications with fast variation of coupling coefficient and load power.

**Stability analysis of current-source DC power distribution.** It is a popular configuration in voltage source DC power distribution that multiple load converters, in parallel connection, are sharing a common input DC voltage bus. With similar configuration, multiple downstream load-side converters can also be connected in parallel to the IPT converter. SSIPT converters are among the most power efficient IPT converters. However, unlike a voltage source, an SSIPT converter provides a constant output current with high output impedance when it operates at its most power efficient point. Such current source DC power distribution system is relatively unexplored. The load-side converters may be either voltage-driven or current-driven converters. Therefore, this thesis will first revisit the stability of current source DC power distribution system using impedance-based approach. A more general set of criterion, based on power balance to distinguish the load-side converters, are also derived.

## 1.6 Outline of the Thesis

The thesis is arranged in the following order.

Chapter 1 provides the background and literature review of the IPT systems. Three kinds of WPT technologies are introduced, including electromagnetic radiation, capacitive power transfer and inductive power transfer. IPT is widely used and its applications are further introduced. The literature review of recent development of IPT systems is provided in terms of coupler design, compensation network, control method and safety issue. The objective and outline of the thesis are presented.

In Chapter 2, four basic compensation topologies (i.e., SS, SP, PS and PP) are reviewed based on conditions to achieve maximum efficiency and load-independent output. To achieve both maximum efficiency and load-independent output, the design and selection of the IPT converters are evaluated. For secondary series compensation (i.e., SS and PS), the choice of operating frequency and the design of compensation network is independent of coupling coefficient.

With minimum number of converter stages to achieve high efficiency, a single-stage IPT converter is designed for EV battery charging in Chapter 3. The characteristics of SSIPT converter are reviewed, including LIC and LIV, which naturally provide the required CC and CV outputs for EV battery charging. The efficiencies at these two operating points are analyzed, and the overall efficiency of the SSIPT converter for the whole charging profile is optimized by determining a nominal load quality factor  $Q_n$ .

In Chapter 4, linear controller design for efficiency optimization in a three-stage IPT system is proposed. A three-stage IPT system usually has more freedom for output control and efficiency optimization. The relationship between maximum SSIPT converter efficiency and voltage ratio is first studied. Advantages of the proposed linear control method is readily observed compared with conventional P&O method. Large-signal and small-signal transfer functions are derived for controller design.

Chapter 5 starts with a revisit of the impedance-based stability criterions

for voltage-source system and current-source system. An unexplored power distribution system is proposed, where an SSIPT converter without voltage regulator is in parallel with multiple independently controlled load converters. A more general set of stability criterion based on power balance is proposed to distinguish the load converters individually between voltage-driven converter and current driven converter.

Chapter 6 concludes the thesis. The major contributions are summarized. Some suggestions for future research are discussed.

## Chapter 2

# Overview of Four Basic IPT Compensation Topologies

The power efficiency of the IPT converters are relatively low, due to low coupling coefficient of the loosely-coupled transformer. Therefore, it is important to maintain the IPT converters operating at their maximum efficiency points by selecting proper compensation network, operating frequency and the load. Given a compensation network, previous studies only studied the optimum operating frequency and the loading condition to achieve maximum efficiency [50,136,137,172,173]. However, to simplify controller design for output regulation, load-independent output characteristics are also important for IPT converters [133–135].

In this chapter, four basic compensation topologies are reviewed and evaluated based on conditions to achieve maximum efficiency and load-independent output. We will combine maximum efficiency and load-independent output for the design and selection of the IPT converters.

## 2.1 Four Basic Compensation Topologies

Four compensation topologies of a loosely-coupled transformer are shown in Fig. 2.1.  $R_P$  and  $R_S$  are the resistances of the primary winding and secondary winding, respectively. The magnetic coupler has self inductances  $L_P$  and  $L_S$ , and mutual inductance  $M$ . The coupling coefficient is defined as the traditional transformer, given by

$$k = \frac{M}{\sqrt{L_P L_S}} \quad (2.1)$$

The primary winding and the secondary winding can be compensated by a single capacitor. Therefore, we have four basic compensation topologies labeled as SS, SP, PS, PP of the IPT converters as shown in Fig. 2.1, where the first S or P stands for series or parallel compensation of the primary winding and the second S or P stands for series or parallel compensation of the the secondary winding. Primary series compensated topologies are usually driven by an AC voltage source, while primary parallel compensated topologies are usually driven by an AC current source.

## 2.2 Maximum Power Efficiency

In this section, the power efficiency of these four basic compensation topologies will be highlighted first. Since the Equivalent Series Resistance (ESR) of the capacitor is assumed to be negligible, the calculation of the power efficiency is the same for secondary series compensation topologies, i.e., SS and PS. Similarly, the calculation of the power efficiency is the same for secondary parallel compensation topologies, i.e., SP and PP. Therefore, we will use circuits of SS compensated IPT (SSIPT) converter and SP compensated IPT (SPIPT) converter, as shown in Fig. 2.2 for power efficiency calculation.

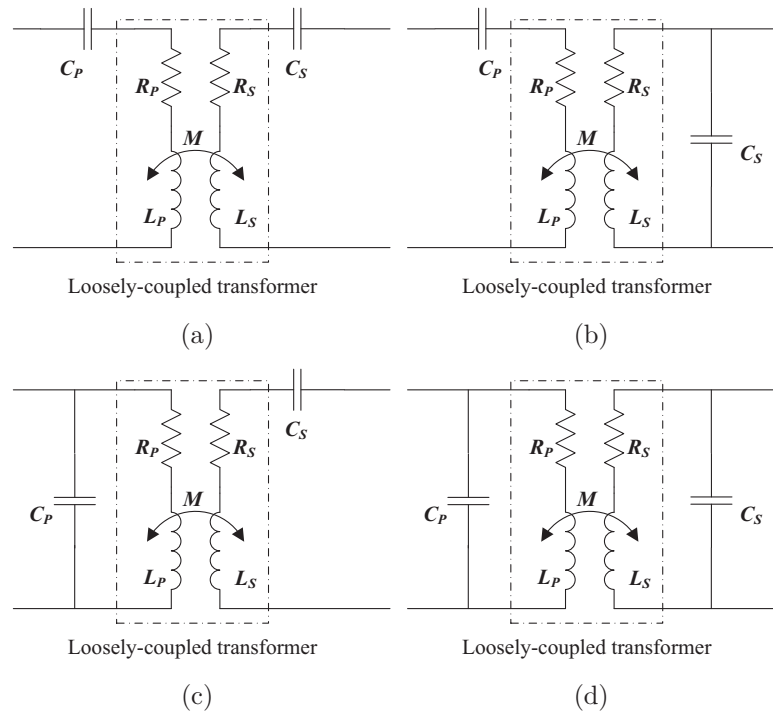


Figure 2.1: The four basic compensation topologies of IPT system (a) SS compensation. (b) SP compensation. (c) PS compensation. (d) PP compensation.

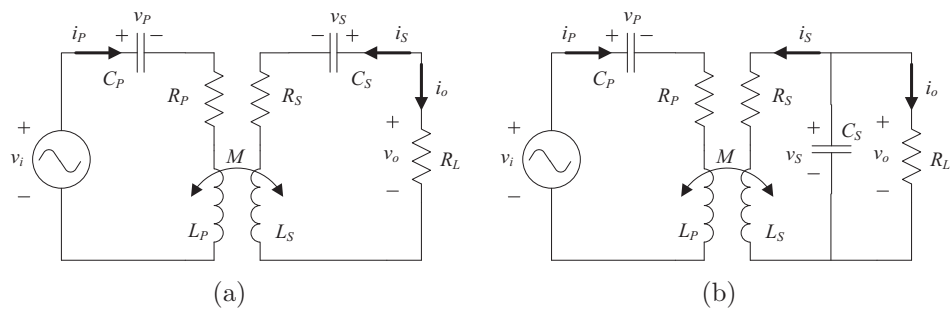


Figure 2.2: Circuit of (a) SSIPT converter. (b) SPIPT converter.

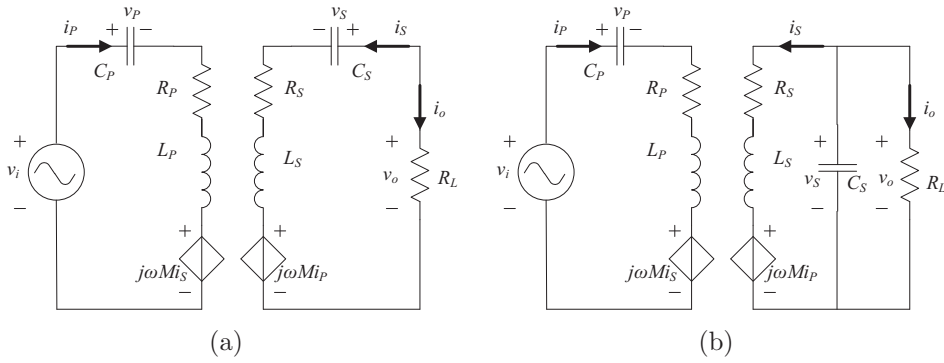


Figure 2.3: Equivalent circuit model of (a) SSIPT converter. (b) SPIPT converter.

Fig. 2.2 shows an equivalent circuit of commonly used SSIPT converter and SPIPT converter model [136, 137, 173]. The circuits are driven by an approximate equivalent AC voltage source  $v_i$  at a fundamental angular frequency  $\omega$  modulated by the inverter. The output is usually rectified to drive a DC load with  $R_L$  being the AC equivalent resistance.  $R_P$  and  $R_S$  are the resistances of the primary winding and secondary winding, respectively. Fig. 2.3 gives an equivalent circuit of Fig. 2.2 for the analysis of steady-state solutions. In the subsequent analysis, a frequency-domain equivalent circuit is adopted and only the fundamental component is considered here for simplicity [126, 136, 137, 173, 174]. The fundamental component approximation is sufficiently accurate for a high quality factor resonant circuit that works near resonance.

The power efficiency of the IPT models shown in Fig. 2.3 can be determined by considering the power loss in  $R_P$  and  $R_S$  [137]. The power efficiency is therefore given by

$$\eta = \frac{\Re(Z_r)}{R_P + \Re(Z_r)} \frac{\Re(Z_S) - R_S}{\Re(Z_S)} \quad (2.2)$$

where  $Z_S$  is the impedance of the secondary network including the loading resistance.  $Z_r$  is the reflected impedance of  $Z_S$  from the secondary to the primary,

given by

$$Z_r = \frac{\omega^2 M^2}{Z_S}, \quad (2.3)$$

$\Re(Z_r)$  is the real component of  $Z_r$ .

$Z_S$  is the impedance of either the secondary series compensated network or the secondary parallel compensated network. By using the tailing subscripts  $-S$  and  $-P$  to distinguish the impedance of secondary series compensation and parallel compensation network,  $Z_{S-S}$  and  $Z_{S-P}$  are given by

$$Z_{S-S} = j\omega L_S + \frac{1}{j\omega C_S} + R_S + R_L, \text{ and} \quad (2.4)$$

$$Z_{S-P} = j\omega L_S + R_S + \frac{1}{j\omega C_S} || R_L, \quad (2.5)$$

respectively. Therefore,  $Z_{r-S}$  and  $Z_{r-P}$  are given by

$$Z_{r-S} = \frac{\omega^2 M^2}{j\omega L_S + \frac{1}{j\omega C_S} + R_S + R_L}, \text{ and} \quad (2.6)$$

$$Z_{r-P} = \frac{\omega^2 M^2}{j\omega L_S + R_S + \frac{1}{j\omega C_S} || R_L}, \quad (2.7)$$

respectively.

In general, resistances  $R_P$  and  $R_S$  of the primary windings and the secondary windings are frequency dependent. In this chapter, the resistances are represented as quality factors in resonant circuits. We make an assumption that  $Q_P$  and  $Q_S$  are maximized at  $\omega_P$  and  $\omega_S$ , respectively. When the operating frequencies are within a certain range of  $\omega_P$  and  $\omega_S$ ,  $Q_P$  and  $Q_S$  are near their maximum.

Therefore,

$$Q_P = \frac{\omega L_P}{R_P} \approx \frac{\omega_P L_P}{R_P}, \quad (2.8)$$

$$Q_S = \frac{\omega L_S}{R_S} \approx \frac{\omega_S L_S}{R_S}. \quad (2.9)$$

The loading resistance  $R_L$  of a series compensated circuit and a parallel compensated circuit are represented by quality factors, given by

$$Q_{L-S} = \frac{\omega_S L_S}{R_L}, \quad (2.10)$$

$$Q_{L-P} = \frac{R_L}{\omega_S L_S}. \quad (2.11)$$

respectively.

The primary resonant angular frequency  $\omega_P$  and the secondary resonant angular frequency  $\omega_S$  are defined as

$$\omega_P = \frac{1}{\sqrt{L_P C_P}}, \text{ and} \quad (2.12)$$

$$\omega_S = \frac{1}{\sqrt{L_S C_S}}. \quad (2.13)$$

By substituting (2.4), (2.5), (2.6) and (2.7) into (2.2), the power efficiency of secondary series compensation and secondary parallel compensation can be calculated as

$$\eta_{-S} = \frac{\frac{\omega}{\omega_S} k^2 \frac{1}{Q_L}}{\frac{1}{Q_P} \left( \frac{\omega}{\omega_S} \frac{1}{Q_S} + \frac{1}{Q_L} \right)^2 + \frac{1}{Q_P} \left( \frac{\omega}{\omega_S} - \frac{\omega_S}{\omega} \right)^2 + \frac{\omega}{\omega_S} k^2 \left( \frac{\omega}{\omega_S} \frac{1}{Q_S} + \frac{1}{Q_L} \right)}, \quad (2.14)$$

$$\eta_{-P} = \frac{k^2 \frac{\omega^2}{\omega_P \omega_S} Q_L}{\frac{1}{Q_P} \left[ \left( Q_L + \frac{1}{Q_S} - \frac{\omega^2}{\omega_S^2} Q_L \right)^2 + \left( \frac{\omega}{\omega_S} + \frac{Q_L \omega}{Q_S \omega_S} \right)^2 \right] + k^2 \frac{\omega^2}{\omega_P \omega_S} \left( Q_L + \frac{1}{Q_S} + \frac{Q_L^2 \omega^2}{Q_S \omega_S^2} \right)}. \quad (2.15)$$

It has been studied that, given a load, there exists a local maximum of  $\eta$  at

the operating frequency, denoted by  $\omega_M$  [50, 136, 137, 172, 173]. By solving  $\frac{d\eta}{d\omega}$ , the efficiency of secondary series compensation is maximized at

$$\omega_{M-S} = \frac{\omega_S}{\sqrt{1 - \frac{(\frac{1}{Q_L} + \frac{1}{Q_S})^2}{2}}} \quad (2.16)$$

$$\approx \omega_S \text{ for } \frac{1}{Q_L} + \frac{1}{Q_S} \ll 1, \quad (2.17)$$

$$Q_{L,M-S} = \frac{Q_S}{\sqrt{1 + k^2 \frac{\omega_S}{\omega_P} Q_P Q_S}} \quad (2.18)$$

$$\approx \frac{1}{k} \sqrt{\frac{Q_S}{Q_P}} \text{ for } Q_P \gg 1, Q_S \gg 1. \quad (2.19)$$

and the efficiency of secondary parallel compensation is maximized at

$$\omega_{M-P} = \frac{\omega_S (1 + \frac{1}{Q_L Q_S})^{\frac{1}{2}}}{\Gamma} \quad (2.20)$$

$$\approx \frac{\omega_S}{\Gamma}, \quad (2.21)$$

$$Q_{L,M-P} = \sqrt{\frac{\frac{1}{Q_S^2} + \frac{1+k^2}{\Gamma^2}}{(1 - \frac{1}{\Gamma^2})^2 + \frac{1}{\Gamma^2 Q_S^2} + \frac{k^2}{\Gamma^4}}}. \quad (2.22)$$

where

$$\Gamma = (1 + k^2 \frac{\omega_S Q_P}{\omega_P Q_S})^{\frac{1}{4}}. \quad (2.23)$$

Fig. 2.4 shows the power efficiency versus load quality factor of secondary series compensation and secondary parallel compensation. By substituting (2.17) and (2.19) into (2.14), and substituting (2.21) and (2.22) into (2.15), maximum achievable power efficiencies of secondary series compensation and secondary parallel compensation can be compared. Fig. 2.5 shows that maximum achievable power efficiency points of secondary series compensation and secondary parallel compensation are close with optimum design of compensation network.

From (2.17) and (2.21), it can also be observed that the operating frequency to

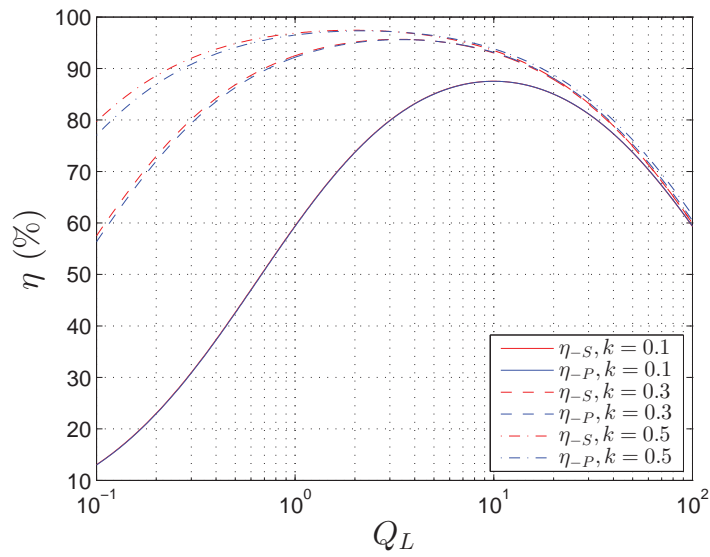


Figure 2.4: Comparison of maximum efficiency versus load quality factor between SSIPT converter and SPIPT converter. Simulation parameters are  $Q_P = Q_S = 150$ .

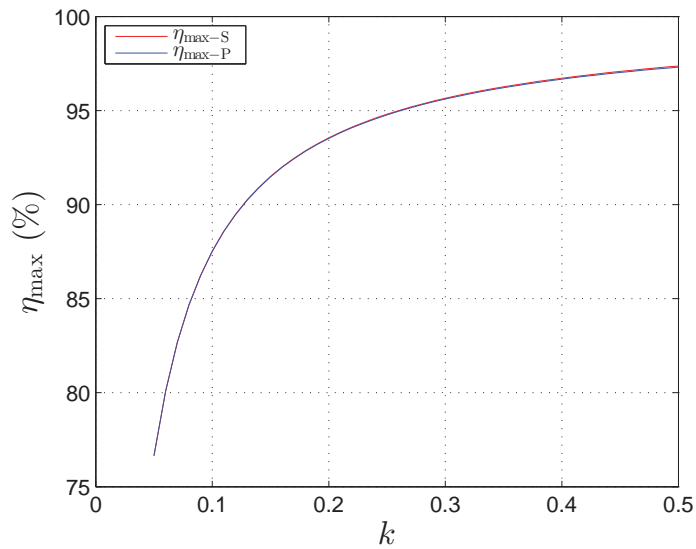


Figure 2.5: Comparison of maximum efficiency versus  $k$  between SSIPT converter and SPIPT converter. Simulation parameters are  $Q_P = Q_S = 150$ .

achieve maximum efficiency is  $k$ -independent for secondary series compensation, while it is  $k$ -dependent for secondary parallel compensation.

## 2.3 Load-independent Current and Load-independent Voltage Output

It is common to cascade load-side converters to the IPT converters, which requires the IPT converters to act as current source or voltage source. Otherwise, it is hard to control the load-side converters cascading to an uncertain source. To eliminate controllers for output regulation, load-independent output characteristics are also important for IPT converters. For primary series compensation, i.e., SSIPT and SPIPT converters, current transfer function and voltage transfer function are defined as  $G = \frac{i_o}{v_i}$  and  $E = \frac{v_o}{v_i}$ , respectively. For primary parallel compensation, i.e., PSIPT and PPIPT converters, current transfer function and voltage transfer function are defined as  $G = \frac{i_o}{i_i}$  and  $E = \frac{v_o}{v_i}$ , respectively. In this section, load-independent current (LIC) and load-independent voltage (LIV) of SS will be calculated as an example [136, 137, 173]. Then, LIC and LIV for all four basic topologies will be summarized and given in a table.

From the circuit model of SSIPT converter shown in Fig. 2.3(a), we have

$$v_i = Z_P i_P + j\omega M i_S \quad (2.24)$$

$$j\omega M i_P = -Z_S i_S \quad (2.25)$$

where  $Z_P = j\omega L_P + \frac{1}{j\omega C_P} + R_P$  and  $Z_S = j\omega L_S + \frac{1}{j\omega C_S} + R_S + R_L$ . By solving (2.24) and (2.25), the output current  $i_o$  is calculated

$$i_o = -i_S = \frac{v_i}{Z_P Z_S + \omega^2 M^2} \quad (2.26)$$

Therefore, current transfer function  $G$  and voltage transfer function  $E$  are calculated by

$$G = \frac{i_o}{v_i} = \frac{j\omega M}{Z_P Z_S + \omega^2 M^2} \quad (2.27)$$

$$E = \frac{i_o R_L}{v_i} = \frac{j\omega M R_L}{Z_P Z_S + \omega^2 M^2} \quad (2.28)$$

By assuming  $R_P = R_S = 0$ , ideal current transfer function and ideal voltage transfer function, denoted as  $G_i$  and  $E_i$  are given

$$G_i = \frac{j\omega M}{(j\omega L_P + \frac{1}{j\omega C_P})(j\omega L_S + \frac{1}{j\omega C_S} + R_L) + \omega^2 M^2} \quad (2.29)$$

$$E_i = \frac{j\omega M R_L}{(j\omega L_P + \frac{1}{j\omega C_P})(j\omega L_S + \frac{1}{j\omega C_S} + R_L) + \omega^2 M^2} \quad (2.30)$$

respectively.

$G_i$  and  $E_i$  can be load independent at some operating frequencies. The frequencies can be found by setting the coefficients of  $R_L$  in (2.29) and (2.30) to zero. When ideal current transfer function or ideal voltage transfer function is load-independent, the IPT converters operate at load-independent current (LIC) output or load-independent voltage (LIV) output, respectively.

LIC operating point of SSIPT converter is derived, with the magnitude of ideal current transfer function  $G_{\text{LIC}}$  and operating frequency  $\omega_{\text{LIC}}$  given by

$$G_{\text{LIC}} = |G_i(\omega_{\text{LIC}})| = \frac{1}{\omega_P k \sqrt{L_P L_S}}, \text{ when} \quad (2.31)$$

$$\omega_{\text{LIC}} = \omega_P. \quad (2.32)$$

LIV operating points of SSIPT converter are derived, with the magnitude of

ideal voltage transfer function  $E_{\text{LIV}}$  and operating frequency  $\omega_{\text{LIV}}$  given by

$$E_{\text{LIV}} = |E_i(\omega_{\text{LIV,L}})| = \sqrt{\frac{L_S}{L_P}} \frac{k(\omega_P^2 + \omega_S^2 - \Delta)}{(2k^2 - 1)\omega_P^2 + \omega_S^2 - \Delta}, \text{ or} \quad (2.33)$$

$$E_{\text{LIV}} = |E_i(\omega_{\text{LIV,H}})| = \sqrt{\frac{L_S}{L_P}} \frac{k(\omega_P^2 + \omega_S^2 + \Delta)}{(2k^2 - 1)\omega_P^2 + \omega_S^2 + \Delta}, \text{ when} \quad (2.34)$$

$$\omega_{\text{LIV,L}} = \sqrt{\frac{\omega_P^2 + \omega_S^2 - \Delta}{2(1 - k^2)}}, \text{ or} \quad (2.35)$$

$$\omega_{\text{LIV,H}} = \sqrt{\frac{\omega_P^2 + \omega_S^2 + \Delta}{2(1 - k^2)}}, \quad (2.36)$$

respectively, where

$$\Delta = \sqrt{(\omega_P^2 + \omega_S^2)^2 - 4(1 - k^2)\omega_P^2\omega_S^2} \quad (2.37)$$

With similar calculations, we can derive the operating conditions to achieve LIC and LIV for SPIPT, PSIPT and PPIPT converters. Table. 2.1 and Fig. 2.6 give a summary of the operating conditions for four basic compensation topologies.

Table 2.1: Summary of LIC and LIV

		LIC		LIV	
		$\omega_{\text{LIC}}$	$G_{\text{LIC}}$	$\omega_{\text{LIV}}$	$E_{\text{LIV}}$
SS	$\omega_P$		$\frac{1}{\omega_P k \sqrt{L_P L_S}}$	$\omega_L$	$\sqrt{\frac{L_S}{L_P}} \frac{k(\omega_P^2 + \omega_S^2 - \Delta)}{(2k^2 - 1)\omega_P^2 + \omega_S^2 - \Delta}$
				$\omega_H$	$\sqrt{\frac{L_S}{L_P}} \frac{k(\omega_P^2 + \omega_S^2 + \Delta)}{(2k^2 - 1)\omega_P^2 + \omega_S^2 + \Delta}$
SP	$\omega_L$		$\frac{2k}{\sqrt{L_P L_S}} \frac{\sqrt{\frac{\omega_P^2 + \omega_S^2 - \Delta}{2(1 - k^2)}}}{\omega_P^2 + \omega_S^2 + \Delta}$	$\omega_Q$	$\frac{1}{k} \sqrt{\frac{L_S}{L_P}}$
	$\omega_H$				
PS	$\omega_P$		$\frac{1}{k} \sqrt{\frac{L_P}{L_S}}$	$\omega_L$	$\frac{2\omega_P^2(1 - k^2)\sqrt{L_P L_S} \sqrt{\frac{\omega_P^2 + \omega_S^2 - \Delta}{2(1 - k^2)}}}{(1 - 2k^2)\omega_P^2 - \omega_S^2 + \Delta}$
				$\omega_H$	$\frac{2\omega_P^2(1 - k^2)\sqrt{L_P L_S} \sqrt{\frac{\omega_P^2 + \omega_S^2 + \Delta}{2(1 - k^2)}}}{(1 - 2k^2)\omega_P^2 - \omega_S^2 - \Delta}$
PP	$\omega_L$		$2k \sqrt{\frac{L_P}{L_S}} \frac{\omega_P^2}{\omega_P^2 - \omega_S^2 + \Delta}$	$\omega_Q$	$\frac{\omega_P \sqrt{1 - k^2} \sqrt{L_P L_S}}{k}$
	$\omega_H$				

Variables  $\omega_Q$ ,  $\omega_L$  and  $\omega_H$  in Table 2.1 are given as

$$\omega_Q = \frac{\omega_P}{\sqrt{1-k^2}}, \quad (2.38)$$

$$\omega_L = \sqrt{\frac{\omega_P^2 + \omega_S^2 - \Delta}{2(1-k^2)}}, \text{ and} \quad (2.39)$$

$$\omega_H = \sqrt{\frac{\omega_P^2 + \omega_S^2 + \Delta}{2(1-k^2)}} \quad (2.40)$$

respectively, where

$$\Delta = \sqrt{(\omega_P^2 + \omega_S^2)^2 - 4(1-k^2)\omega_P^2\omega_S^2}. \quad (2.41)$$

## 2.4 Load-independent Output and Maximum Efficiency

Achieving maximum efficiency and having load-independent output (LIC or LIV), will be two objectives of the IPT converters. Therefore, we will further compare these four compensation topologies through studying the feasibility of achieving maximum efficiency and load-independent output at the same time.

Table 2.2: Summary of Operating frequencies  $\omega_M$ ,  $\omega_{\text{LIC}}$  and  $\omega_{\text{LIV}}$

	$\omega_M$	$\omega_{\text{LIC}}$	$\omega_{\text{LIV}}$
SS, PS	$\omega_S$	$\omega_P$	$\omega_L, \omega_H$
SP, PP	$\frac{\omega_S}{(1+k^2\frac{\omega_S}{\omega_P})^{\frac{1}{4}}}$	$\omega_L, \omega_H$	$\omega_Q$

As shown in Table 2.2,  $\omega_M$  is the operating frequency to achieve maximum efficiency, while  $\omega_{\text{LIC}}$  and  $\omega_{\text{LIV}}$  are the operating frequencies to achieve LIC and LIV, respectively. By equating  $\omega_M$  to  $\omega_{\text{LIC}}$  or  $\omega_{\text{LIV}}$ , we can select the operating

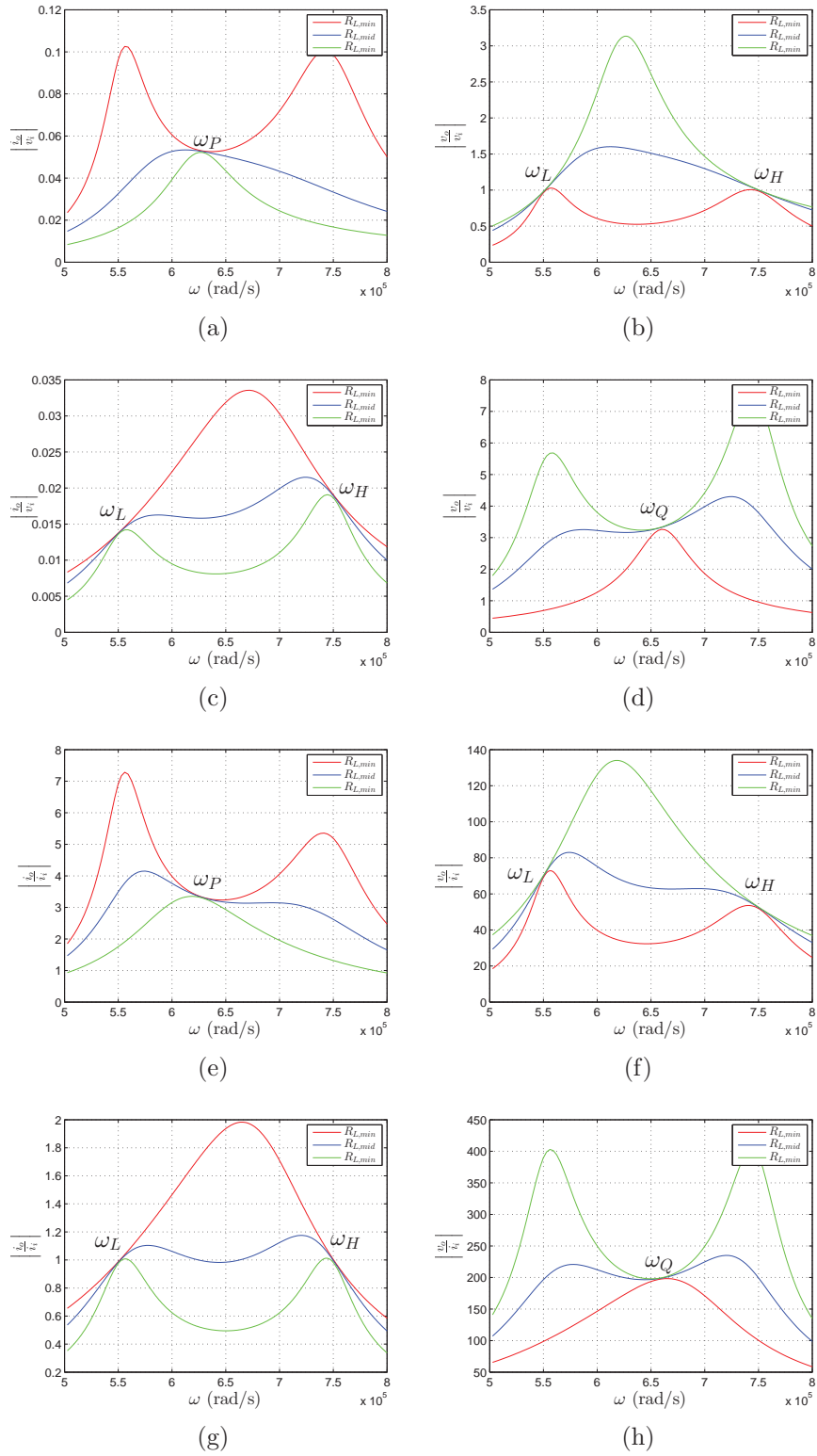


Figure 2.6: Current transfer function of (a) SS, (c) SP, (e) PS, and (g) PP compensated IPT converters. Voltage transfer function of (b) SS, (d) SP, (f) PS, and (h) PP compensated IPT converters.

frequency  $\omega$ , where

$$\omega = \omega_M = \omega_{\text{LIC}} \text{ or } \omega_{\text{LIV}} \quad (2.42)$$

to have maximum efficiency and load-independent output at the same time. The resonant frequencies  $\omega_P$  and  $\omega_S$  should be designed to satisfy (2.42). The ratio between  $\omega_P$  and  $\omega_S$  is defined as  $\mu$ , given by

$$\mu = \frac{\omega_P}{\omega_S}. \quad (2.43)$$

Therefore,  $\omega_P$ ,  $\omega_Q$ ,  $\omega_L$  and  $\omega_H$  are given as

$$\omega_P = \omega_S \mu \quad (2.44)$$

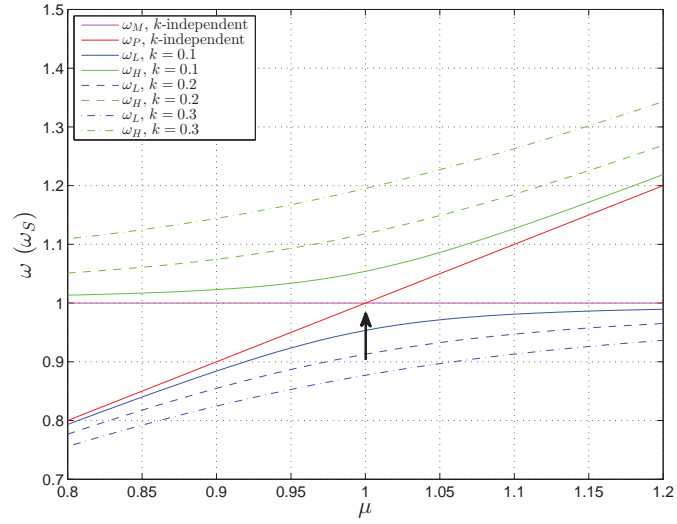
$$\omega_Q = \frac{\omega_S}{\left(1 + \frac{k^2}{\mu}\right)^{\frac{1}{4}}} \quad (2.45)$$

$$\omega_L = \omega_S \sqrt{\frac{\mu^2 + 1 - \sqrt{(\mu^2 + 1)^2 - 4(1 - k^2)\mu^2}}{2(1 - k^2)}} \quad (2.46)$$

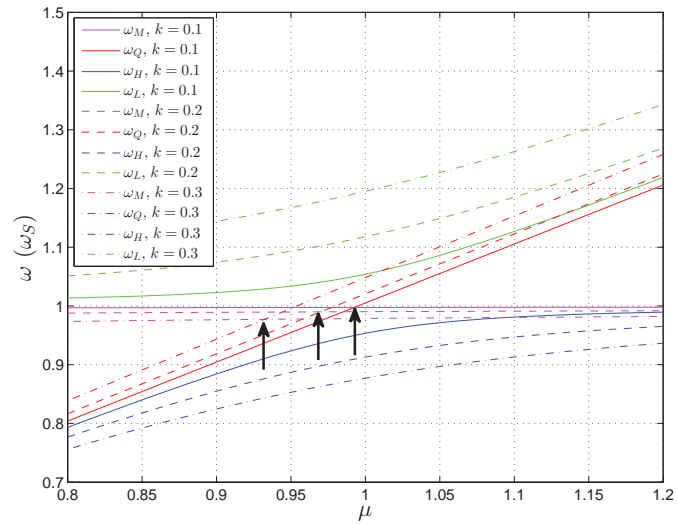
$$\omega_H = \omega_S \sqrt{\frac{\mu^2 + 1 + \sqrt{(\mu^2 + 1)^2 - 4(1 - k^2)\mu^2}}{2(1 - k^2)}} \quad (2.47)$$

Equation (2.42) can be solved numerically by plotting equations (2.44) - (2.47) versus  $\mu$  for various  $k$  as shown in Fig. 2.7. From Fig. 2.7(a), a single intersection point is found at  $\mu = 1$ , being  $k$ -independent. From Fig. 2.7(b), there are several intersection points at different values of  $\mu$ , which are  $k$ -dependent. Therefore, we can conclude that

1. For secondary series (i.e., SS and PS) compensated IPT converters, the design of the resonant frequency to achieve maximum efficiency and LIC simultaneously is  $k$ -independent. The operating frequencies are also  $k$ -independent. Therefore, they are suitable for applications with  $k$ -variation.



(a)



(b)

Figure 2.7: Operating frequencies versus  $\mu$  for (a) achieving load-independent output and maximum efficiency for secondary series compensation, and (b) achieving load-independent output and maximum efficiency for secondary parallel compensation. The intersection points are indicated with upward arrows.

2. For secondary parallel compensated (i.e., SP and PP) IPT converters, the design of the resonant frequency to achieve maximum efficiency and LIV simultaneously is  $k$ -dependent. In addition, the operating frequencies to achieve maximum efficiency and LIV is also  $k$ -dependent. Therefore, they are not suitable to be used in applications with  $k$ -variation, because additional controls for compensation network matching and operating frequencies are needed.

## 2.5 Summary

Comparison of secondary series compensation and secondary parallel compensation has been studied in the chapter, in the view point of achieving maximum efficiency and load-independent output simultaneously. For secondary parallel compensation, the choice of operating frequency and the design of the compensation network depends on coupling coefficient. Therefore, it is not suitable for applications with variation of coupling coefficient. Compared with secondary parallel compensation, secondary series compensation has the following advantage: the choice of the operating frequency and the design of compensation network is independent of coupling coefficient, which is suitable for applications with variation of coupling coefficient. Since an equivalent current source is needed to drive IPT converters with primary parallel compensation, extra components are needed to generate current source from existing voltage source, which will incur extra loss. Therefore, series compensation is preferred to parallel compensation in the primary. In the following chapters, we will choose series-series compensated IPT (SSIPT) converter.

## Chapter 3

# Single-stage IPT Converter for EV Battery Charging

Lithium-ion (Li-ion) batteries are widely used in EVs. The charging profile of lithium-ion batteries for electric vehicles mandates a constant current (CC) at rated power for a depleted battery, and follows by a constant voltage (CV) charging at a power level down to 3% of the rated power in order to fully charge the battery as shown in Fig. 3.1. An inductive-power-transfer (IPT) converter should be designed with minimal number of stages to achieve high efficiency. However, the efficiency-to-load relationship is distinctly different for CC and CV charging operations, posing difficulties for single-stage design.

The IPT converters can achieve optimal efficiency at some resonant frequencies with matched input and output impedances. Deviating from this optimal matching point, the converter efficiency suffers [175]. In view of the narrow input impedance and output impedance ranges of resonant converters, multi-stage converter topologies with input and/or output power converters connected in-front-of and/or after the IPT converter have been proposed [160, 164, 176], hoping to improve system efficiency by operating the resonant converter without modulation at its optimal load while allowing losses of extra efficient

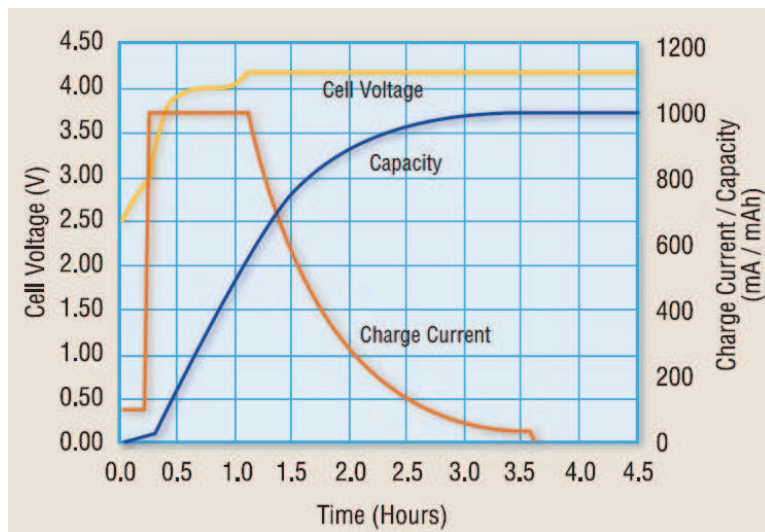


Figure 3.1: Typical charging profile for a Li-ion battery cell [6].

converters. The obvious drawbacks of these multi-stage converters are that (a) more converters are used, (b) more complicated control may be needed for the coordination of controls between the primary and secondary sides of the IPT converter, and (c) these topologies are for general applications as they are designed for an arbitrary variation of load range without optimizing the power loss and the charging time of the battery charging profile. Without the additional cascaded power converter(s) for the tracking of the input and/or load impedance, a single-stage IPT converter has less degree of freedom for optimization under the specific charging profile. The single-stage IPT converter can be designed for maximum efficiency at maximum load power. Thus, the IPT converter can efficiently operate with shallow modulation at either its load-independent voltage output (LIV) operation point using series-parallel compensation or load-independent current output (LIC) operation point using series-series compensation [136, 137]. At these operation points, the equivalent reactance on the inverter switches is near ZPA. To achieve energy-efficient CC and CV charging stages with narrow-range PWM control and/or FM control, switching of IPT compensation topologies from series-series (S-S) compensation

to series-parallel (S-P) compensation is needed [158, 159]. These hybrid- or dual-topology IPT converters necessitate extra power switches along the main power path of the converter, incurring additional cost for power switches and power loss.

This chapter describes the design of a single-stage IPT converter that complies with the battery charging profile and at the same time achieves optimal efficiency. Design optimization includes soft switching for the entire battery load range, efficiency optimization for CC and CV modes of operation, and system efficiency optimization for the whole battery charging profile. Measured results of two experimental IPT battery chargers are presented for illustration and verification.

### 3.1 Implementation Cases for EV charging

To eliminate the power loss associated with the multi-stage and hybrid-topology IPT converter at rated power, some design options for a single topology IPT converter are available. First, the single topology IPT converter can operate near its maximal efficiency point and be controlled for the required two stages of battery charging. Alternatively, it may operate at its optimal efficiency point for the first stage of CC or second stage of CV charging and use a control technique with reduced efficiency for the other stages of charging. Furthermore, it may operate at its optimal efficiency points at LIC and LIV for the first and second stages of charging respectively. The possible cases of implementations for a single topology IPT converter are summarized in Table.3.1.

In Table. 3.1, cases (C1) to (C2) are mostly achieved by utilizing different depth and type of modulations. Without modulation, the converter can be efficiently operated at operation points LIV and LIC. As a rule of thumb, efficiency suffers from more depth of modulation.

Case (C1) has been used in a single-stage S-S compensated IPT (SSIPT) converter with a simple narrow-frequency-range FM control [177]. Normally,

Table 3.1: Cases of Implementation

Case	Operating point	CC charging	CV charging
(C1)	LIV	MC	MC
(C2)	LIC	MC	MC
(C3)	LIV	MC	native
(C4)	LIC	native	MC
(C5)	LIC	native	
	LIV		native
note:	MC - modulation and control		
	native - minimal modulation for efficiency		

a frequency limiter is used to implement the FM control [177] to maintain stability in the loosely-coupled systems [4, 126, 177]. It is obvious that the single topology SSIPT converter operating near the LIV operating point [177] can only be optimized for efficiency with an operating frequency at a single loading point for the CC and CV modes of charging for an EV battery. Likewise, this also applies to case (C2). However, due to their operations near LIC operating point, cases (C2) and (C4) require deep modulation to satisfy the wide current range within the CV charging stage of the battery charging profile. Thus, a large variation of the phase angle between the driving voltage and the current of a compensated IPT transformer is needed, making soft switching impossible if FM or PWM control is employed for the required load range [178]. In contrast, an IPT converter operating at its resonance, i.e., SSIPT converter operating at LIC operating point, is found to be most power efficient [86, 160, 163, 164, 176, 179], making implementation of case (C3) less attractive than case (C5).

In this chapter, a single-stage SSIPT converter operating at LIC for CC charging and at LIV for CV charging complying with an EV battery profile (i.e., case (C5)) is designed and optimized for efficiency and ease of control.

## 3.2 Characteristics of SSIPT converter

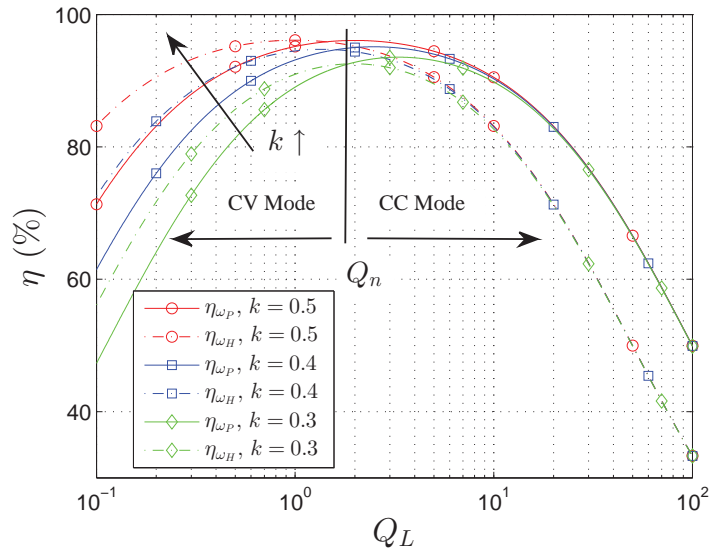
In Chapter 2, it shows that the SSIPT converter can operate at resonant frequency  $\omega_P$ , which is the LIC operating point, for the best efficiency at rated load. However, the SSIPT converter operating at  $\omega_H$ , which is the LIV point, can be more efficient than operating at LIC point at light load [137]. To facilitate the implementation (C5) of a single topology IPT converter complying with the battery charging profile, this section will first go into the analysis of the power efficiency at these two operating points.

Operating frequencies for ideal load-independent transconductance  $G_{LIC}$  and voltage transfer ratio  $E_{LIV}$  of the SSIPT converter have been studied in Section. 2.3 by assuming zero power loss. However, in practical applications, operating at these frequencies is subject to small variations of  $G_{LIC}$  and  $E_{LIV}$  due to load variation. In this section, practical transconductance, voltage transfer ratio, and input phase angle will also be studied by taking equivalent winding resistance  $R_P$  and  $R_S$  into consideration. Also,  $\mu$  will be designed to be smaller than 1 to facilitate ZVS of MOSFET switches.

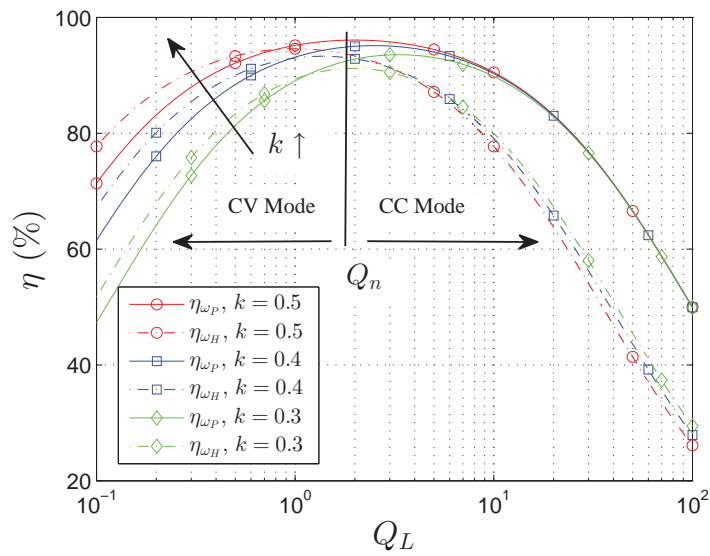
### 3.2.1 Efficiency and Control

As an illustration, the efficiencies versus load quality factor for  $\mu = 1$ , operating frequencies  $\omega = \omega_P$  (CC mode) and  $\omega = \omega_H$  (CV mode) are calculated using (2.14), as shown in Fig. 3.2. In the calculation, we use  $Q_{P\max} = Q_{S\max} = Q_P = Q_S = 100$  and  $k = 0.3, 0.4$  and  $0.5$ . Fig. 3.2 shows that the peak efficiency in the CC operation appears at a higher  $Q_L$  than that of the CV operation. This trend supports the implementation case (C5) of battery charging described in Section 3.3. Hence, the location of  $Q_L$  has practical importance for the peak efficiency and deserves further analysis.

For constant  $R_P$  and  $R_S$ , the maximum efficiencies  $\eta_{\max_R}(\omega_P)$  and  $\eta_{\max_R}(\omega_H)$



(a)



(b)

Figure 3.2: Comparison of efficiency  $\eta$  versus  $Q_L$  operating at  $\omega_S$  (CC mode) and  $\omega_H$  (CV mode) for various  $k$  by using the model of (a) constant IPT transformer winding resistance and (b) constant IPT transformer winding quality factor.

with  $\mu = 1$  can be calculated using (2.14) and the corresponding load quality factors can be approximated as

$$Q_{LCCR} \approx \frac{1}{k} \text{ for } Q_P, Q_S \gg 1 \quad (3.1)$$

$$Q_{LCVR} \approx \frac{1}{k} \sqrt{\frac{1-k}{1+\frac{Q_P}{Q_S}}} \text{ for } Q_S \gg 1 \quad (3.2)$$

Likewise, for constant  $Q_P$  and  $Q_S$ , we have

$$Q_{LCCQ} \approx \frac{1}{k} \text{ for } Q_{P\max}, Q_{S\max} \gg 1, \text{ and} \quad (3.3)$$

$$Q_{LCVQ} \approx \frac{1}{k} \sqrt{\frac{1-k}{1+\frac{Q_{P\max}}{Q_{S\max}}}} \text{ for } Q_{S\max} \gg 1. \quad (3.4)$$

Using equations (3.1) to (3.4), plots of  $Q_L$  and  $\eta_{\max}$  versus  $k$  at peak efficiency can be obtained, as shown in Figs. 3.3 and 3.4. The  $Q_L$  of the battery is high during CC charging, while it is low during CV charging. Therefore, the system efficiency for implementation case (C5) will follow the solid curve during the CC mode of charging and the dashed curve during the CV mode of charging, as shown in Fig. 3.2. In Section 3.3.1, the location  $Q_n$  where the system switches from CC mode to CV mode will be chosen for optimizing the overall efficiency of the EV battery charging profile.

In Section 3.2.3,  $\mu$  will be designed smaller than 1 to facilitate zero-voltage-switching (ZVS) of MOSFET switches during CC mode of operation. In previous study [173],  $\mu < 1$  has been reported to improve efficiency of an SSIPT converter in CV mode where the maximum efficiency increases with decreasing  $\mu$ , as shown in Fig. 3.5(a). Moreover, Fig. 3.5(b) shows the efficiency versus  $Q_L$ . When  $Q_L > 2$ , the efficiency improves with decreasing  $\mu$ , and when  $Q_L < 2$ , the efficiency degrades slightly with decreasing  $\mu$ . The overall degradation of efficiency for  $\mu < 1$  in the CV mode for the normal load range is thus insignificant.

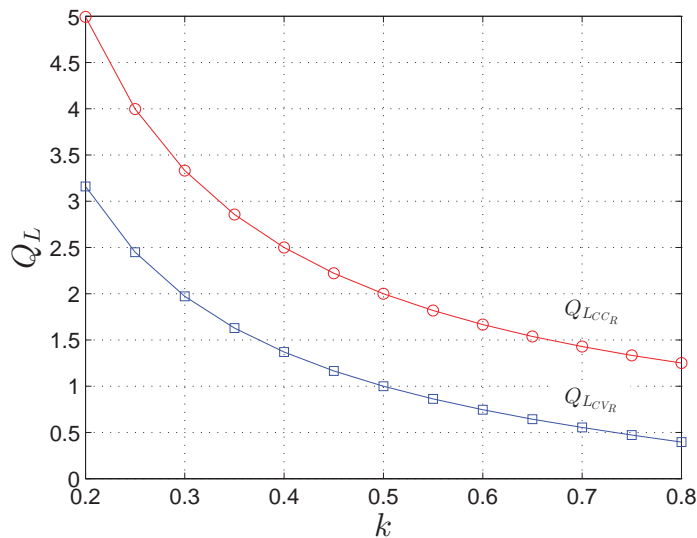
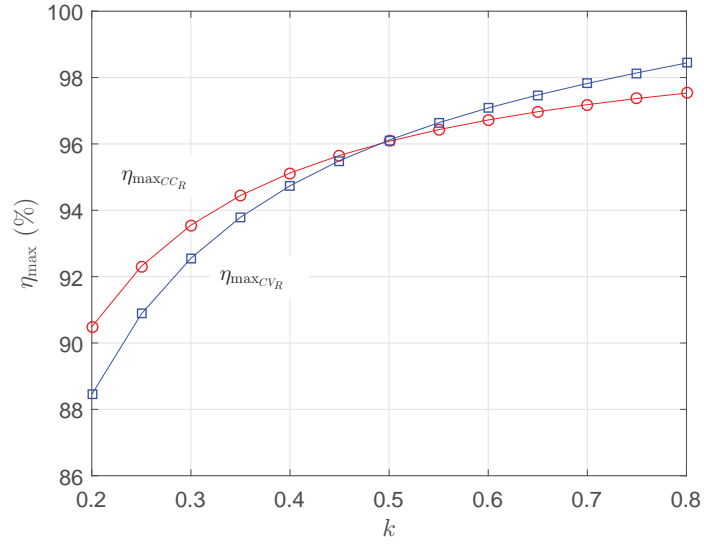


Figure 3.3: Comparison of  $Q_L$  versus  $k$  at peak efficiency operating at  $\omega_S$  (CC mode) and  $\omega_H$  (CV mode). Both models of constant IPT transformer winding resistance and constant IPT transformer winding quality factor give near identical result.

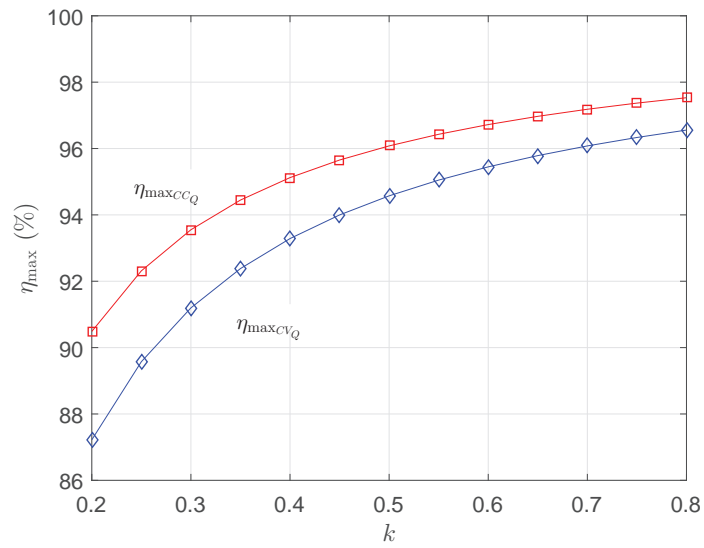
The efficiency trend of the converter designed with  $\mu < 1$  for the CC mode is plotted in Fig. 3.6(b). The efficiency degrades significantly with decreasing  $\mu$ . The degradation of peak efficiency versus  $\mu$  is shown in Fig. 3.6(a). Therefore, in our design,  $\mu$  will be restricted to a few percent below 1 to facilitate soft switching during CC mode of operation.

### 3.2.2 Practical Transconductance and Voltage Transfer Ratio

As the converter is of high power efficiency, operating at the frequencies found in Section 2.3 will still be subject to small variations of  $G_{LIC}$  and  $E_{LIV}$  due to load variation. The practical load-independent transconductance  $G(\omega_P)$  can be found

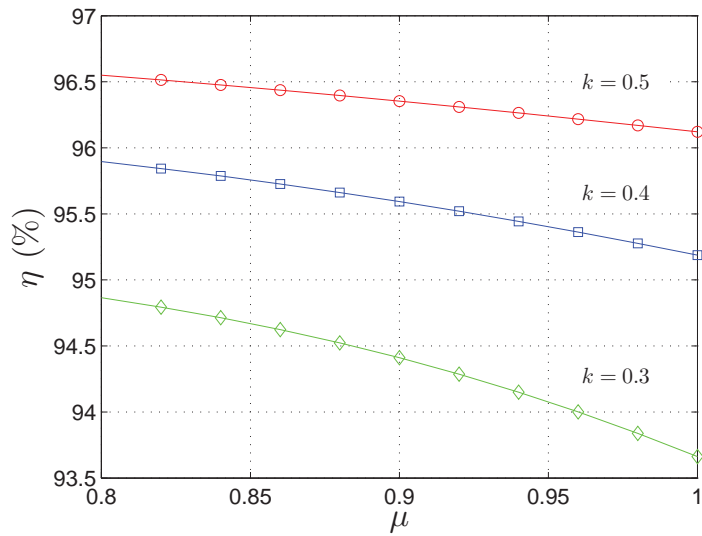


(a)

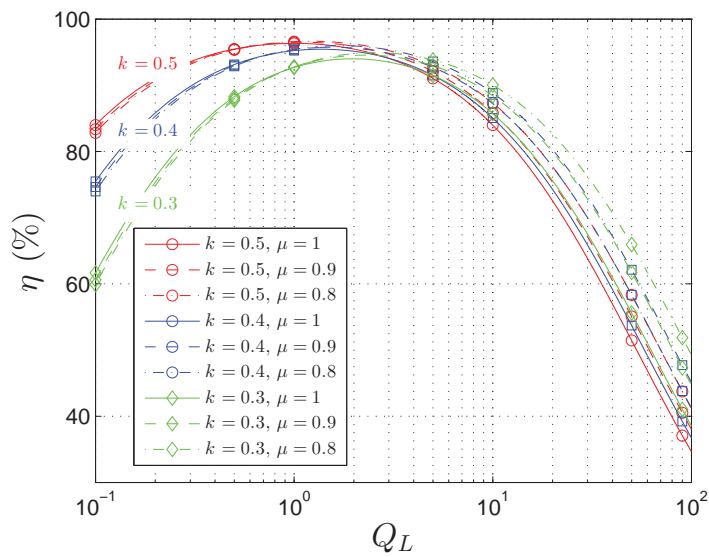


(b)

Figure 3.4: Comparison of  $\eta_{\max}$  vs.  $k$  operating at  $\omega_S$  (CC mode) and  $\omega_H$  (CV mode) using model of (a) constant IPT transformer winding resistance and (b) constant IPT transformer winding quality factor.

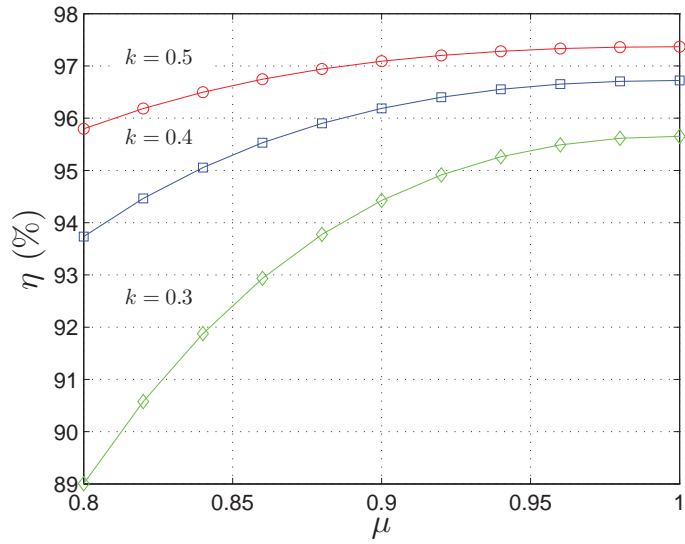


(a)

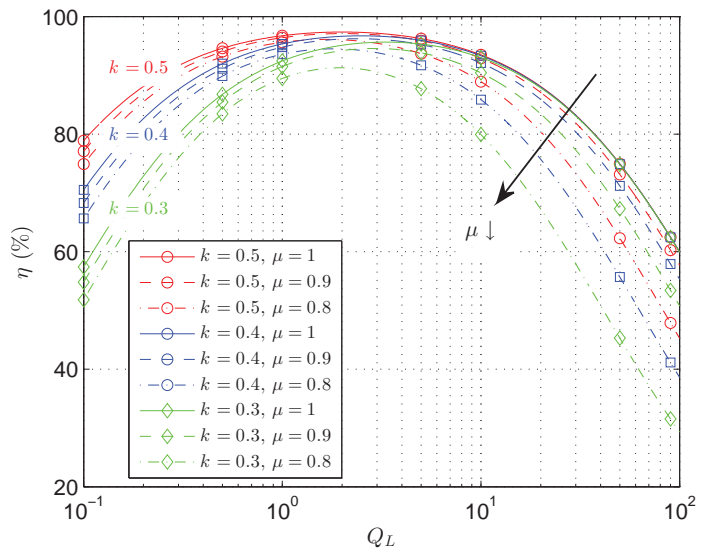


(b)

Figure 3.5: Efficiency comparison of SSIPT converter operating at  $\omega_H$  (CV mode).(a) Peak efficiency vs.  $\mu$ ; (b) efficiency vs.  $Q_L$ .



(a)



(b)

Figure 3.6: Efficiency comparison of SSIPT converter operating at  $\omega_P$  (CC mode). (a) peak efficiency vs.  $\mu$ ; (b) Efficiency vs.  $Q_L$ .

by substituting  $\omega_P$  into (2.31). The normalized error  $\Delta g$  is defined as

$$\begin{aligned}\Delta g &= \frac{|G_i(\omega_P)| - |G(\omega_P)|}{|G_i(\omega_P)|} \\ &= 1 - \left| \frac{\mu^2 k^2}{j \frac{\mu^2 - 1}{Q_P} + \frac{\mu^2}{Q_P Q_S} + \frac{\mu}{Q_P Q_L} + \mu^2 k^2} \right|\end{aligned}\quad (3.5)$$

which can be simplified by putting  $\mu \approx 1$ , i.e.,

$$\Delta g(Q_L) \approx \frac{1}{1 + k^2 Q_P Q_L} \text{ for } Q_S \gg Q_L. \quad (3.6)$$

The practical load-independent voltage transfer ratio  $E(\omega_H)$  can be found by substituting  $\omega_H$  into (2.28). The normalized error  $\Delta e(\omega_H)$  can be defined as

$$\Delta e = \frac{|E_i(\omega_H)| - |E(\omega_H)|}{|E_i(\omega_H)|} = 1 - \left| \frac{E_1}{E_2 - E_3} \right|, \quad (3.7)$$

where

$$\nu = \frac{\omega_H}{\omega_S}, \quad (3.8)$$

$$E_1 = \left( -\frac{\nu^2}{\mu^2} + 1 \right) \left[ -\nu^2 + 1 + \frac{j\nu}{Q_L} \right] - E_3, \quad (3.9)$$

$$E_2 = \left( -\frac{\nu^2}{\mu^2} + 1 + j \frac{\nu^2}{\mu^2 Q_P} \right) E_4 \quad (3.10)$$

$$E_3 = \frac{\nu^4}{\mu^2} k^2 \quad (3.11)$$

$$E_4 = -\nu^2 + 1 + j\nu \left( \frac{\nu}{Q_S} + \frac{1}{Q_L} \right). \quad (3.12)$$

From equations (3.5) and (3.7),  $\Delta g$  increases with decreasing  $Q_L$  while  $\Delta e$  increases with increasing  $Q_L$ , i.e.,  $G(\omega_P)$  and  $E(\omega_H)$  decrease with increasing load. For illustration, Fig. 3.7 shows the percentage error on  $\Delta g$  and  $\Delta e$  versus  $Q_L$ . The load quality factor  $Q_{LCC_R}$  or  $Q_{LCC_Q}$  to achieve maximum efficiency at a particular  $k$  in CC mode is shown in Fig. 3.3. The value of  $Q_L$  read from

Fig. 3.3 can be used to estimate the errors of  $\Delta g$  and  $\Delta e$  using Fig. 3.7. The input voltage variation of the prototype IPT converter described in Section 3.4 can thus be designed to be within a few percent, permitting soft switching by using phase shift PWM control to regulate the desired output current and voltage of the IPT converter.

### 3.2.3 Input Phase Angle

Inductive input phase angle is important for the MOSFET main switches to achieve zero voltage turn-on. The input impedance of the equivalent circuit model shown in Fig. 2.3(a) is given by

$$Z_{\text{in}} = Z_P + Z_{r_s}. \quad (3.13)$$

The corresponding input phase angle is given by

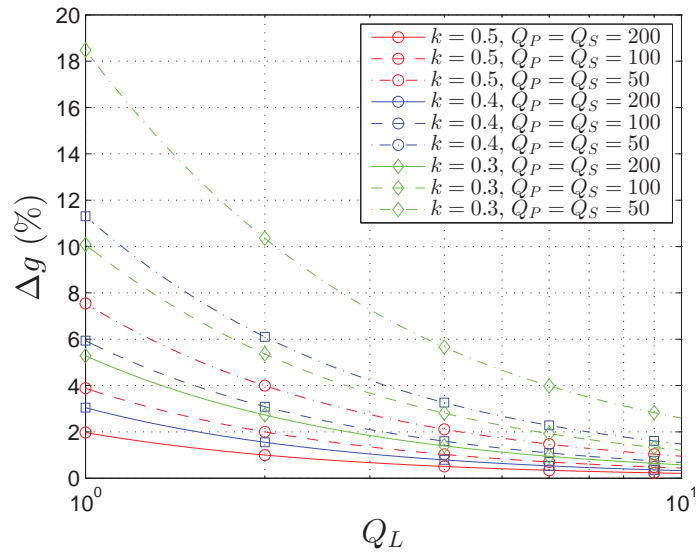
$$\theta_{\text{in}} = \tan^{-1} \left( \frac{\Re(Z_{\text{in}})}{\Im(Z_{\text{in}})} \right). \quad (3.14)$$

To achieve zero voltage turn-on of MOSFET switches, inductive input impedance is expected for both CC and CV modes of operation. For CC mode, the input phase angle is given by

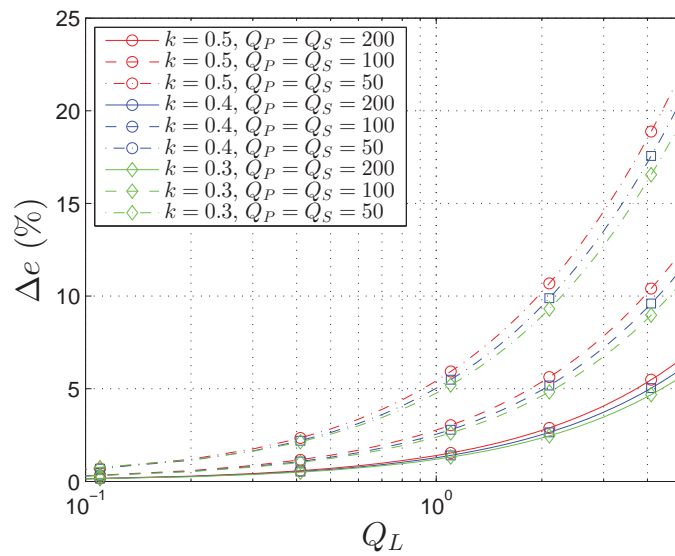
$$\theta_{CC} = \tan^{-1} \frac{-k^2(1 - \frac{1}{\mu^2})}{\frac{1}{Q_P} \left[ A_1^2 + (1 - \frac{1}{\mu^2})^2 \right] + k^2 A_1} \quad (3.15)$$

$$= \tan^{-1} \left\{ Q_L \left( \frac{1}{\mu} - \mu \right) \right\}, \text{ for } Q_P \approx Q_S \gg Q_L, \quad (3.16)$$

where  $A_1 = (\frac{1}{Q_S} + \frac{1}{\mu Q_L})$ . Fig. 3.8(a) shows the input phase angle  $\theta_{CC}$  versus  $Q_L$  in CC mode. When  $\mu = 1$ ,  $\theta_{CC}$  is exactly zero, which leaves no room for PWM control with soft switching. When  $\mu$  is designed to be slightly smaller than 1, positive input phase angle can be achieved to have PWM control with soft



(a)



(b)

Figure 3.7: Plots of (a)  $\Delta g$  and (b)  $\Delta e$  vs.  $Q_L$ .

switching.

For CV mode, the input phase angle is given by

$$\theta_{CV} = \tan^{-1} \frac{(\frac{v^2}{\mu^2} - 1) [A_2^2 + A_3^2] - \frac{v^2}{\mu^2} k^2 A_3}{\frac{v^2}{\mu^2 Q_P} [A_2^2 + A_3^2] + \frac{v^2}{\mu^2} k^2 A_2}, \quad (3.17)$$

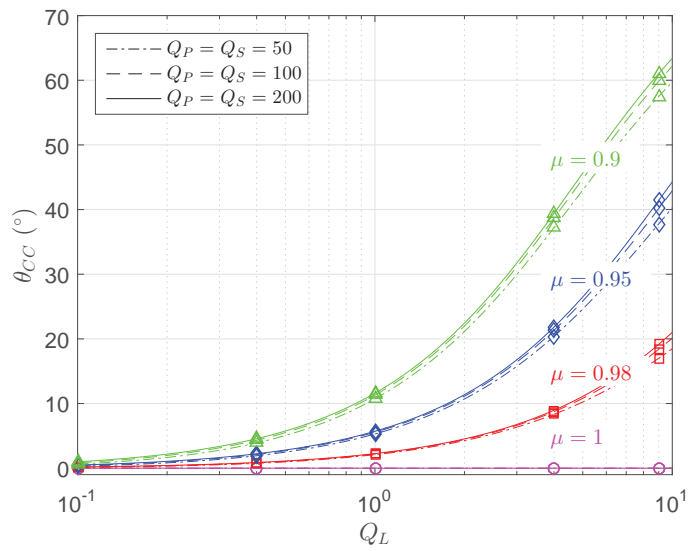
where  $A_2 = (\frac{1}{Q_S} + \frac{1}{vQ_L})$  and  $A_3 = (1 - \frac{1}{v^2})$ . Fig. 3.8(b) shows the input phase angle  $\theta_{CV}$  versus  $Q_L$  in CV mode, where the positive input phase angle guarantees PWM control with soft switching.

### 3.2.4 Control Scheme

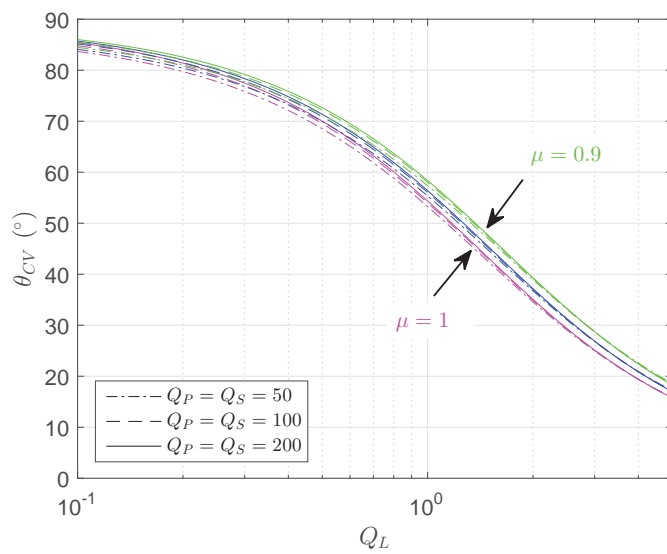
The main circuit of the SSIPT system for EV battery charging with a control scheme is illustrated in Fig. 3.9. The DC voltage  $U_{IN}$  is modulated as a high frequency AC voltage  $v_{in}$  by the set of H-bridge power MOSFET switches that drive the transmitting coil through a series compensation network. The power flow is unidirectional in this application, therefore passive rectifier is used to converter ac power to dc power. Since battery charging is a slow process for the converter, the battery can be modeled as a resistor  $R_{battery}$ , which varies slowly according to the battery charging profile. The rectifier with the battery can be modeled as an equivalent resistor  $R_L$ , i.e.,

$$R_L = \frac{8}{\pi^2} R_{battery}. \quad (3.18)$$

The system will operate at  $\omega_P$  which is slightly lower than  $\omega_S$  to provide a constant current, and at  $\omega_H$  to provide a constant voltage. Since errors are inevitable in the output current and voltage, the input voltage is regulated by a H-bridge inverter using a phase shift PWM control. The fundamental component



(a)



(b)

Figure 3.8: Input phase angle vs.  $Q_L$  for (a) CC mode; (b) CV mode of operation.

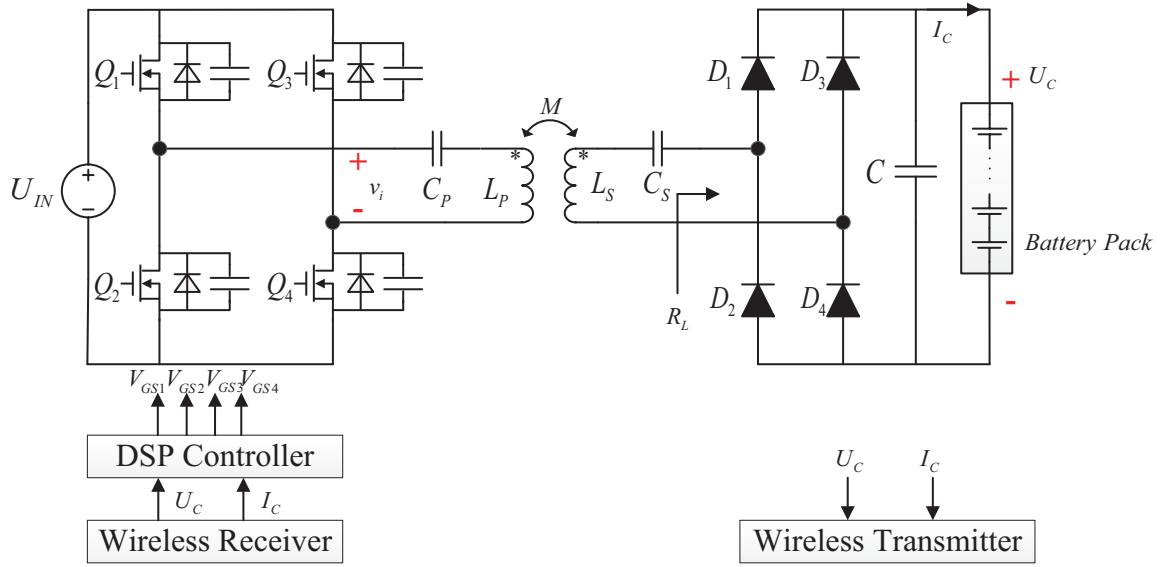


Figure 3.9: Main circuit and control scheme.

of  $v_i$  is modeled as

$$v_i = \frac{4}{\pi} U_{IN} \cos \frac{\theta}{2} \quad \text{or} \quad v_i = \frac{4}{\pi} U_{IN} D. \quad (3.19)$$

where  $U_{IN}$  is the DC input voltage,  $\theta \in (0, \pi)$  is the phase shift angle of the H-bridge and  $D = \cos \theta/2 \in [0, 1]$  is the equivalent duty cycle. The driving signals are generated by a DSP controller. Information of the charging voltage and current in the secondary side is collected and transmitted wirelessly to the controller at the primary side.

### 3.3 Design Consideration

#### 3.3.1 Maximizing Overall Efficiency

Suppose a battery pack consists of  $y$  parallel-connected batteries, and each battery consists of  $x$  series-connected cells [180]. The nominal values of voltage, current

and resistance of a battery pack are given by

$$U_n = 4.2x \text{ V}, \quad (3.20)$$

$$I_n = yC \text{ A, and} \quad (3.21)$$

$$R_n = \frac{U_n}{I_n} = \frac{4.2x}{yC} \Omega \quad (3.22)$$

where  $I_n$  is the current at CC charging,  $U_n$  is the voltage at CV charging, and  $C$  is the maximum current the battery can supply for one hour. Depending on the values of  $x$  and  $y$ , different battery packs have different specifications.

For simplicity of calculating the averaged charging efficiency, the battery charging profile is approximated by several piecewise-linear segments, as shown in Fig. 3.10(a). From the charging parameters given in Table 3.2, the equivalent resistance ( $\Omega$ ) of the battery  $R_{\text{battery}}$  ranges from  $0.714 R_n$  to  $20 R_n$ , i.e., from  $\frac{3x}{yC}$  to  $\frac{4.2x}{0.05yC}$ , as shown in Fig. 3.10(b). We define the load quality factor at the point of switch-over from CC to CV charging as  $Q_n$ , which is  $\frac{\omega_S L_S}{\pi^2 R_n}$  according to (2.10), (3.18) and (3.22), and this gives a charging profile ranging from  $0.05 Q_n$  to  $1.4 Q_n$ , as shown in Fig. 3.10(b).

The equivalent resistance of the battery varies with time within the whole charging profile. Therefore, the charging efficiency varies with time. From Figs. 3.2 and 3.10(b), the choice of  $Q_n$  affects the charging efficiency versus time as shown in Fig. 3.11. The optimization of the converter efficiency for the whole charging profile is thus simplified to choosing  $Q_n$  (or  $\omega_S L_S$  since  $R_n$  is fixed) that maximizes the charging efficiency for the charging profile, i.e.,

$$\begin{aligned} \eta_{\text{overall}} &= \frac{\text{output energy}}{\text{input energy}} \\ &= \frac{\int_0^T U_C(t) I_C(t) dt}{\int_0^{T_1} \frac{U_C(t) I_C(t)}{\eta_{CC}(Q_L(t))} dt + \int_{T_1}^T \frac{U_C(t) I_C(t)}{\eta_{CV}(Q_L(t))} dt}, \end{aligned} \quad (3.23)$$

where  $T_1$  is the CC charging time,  $T$  is the total charging time, and  $Q_L(T_1) = Q_n$ .

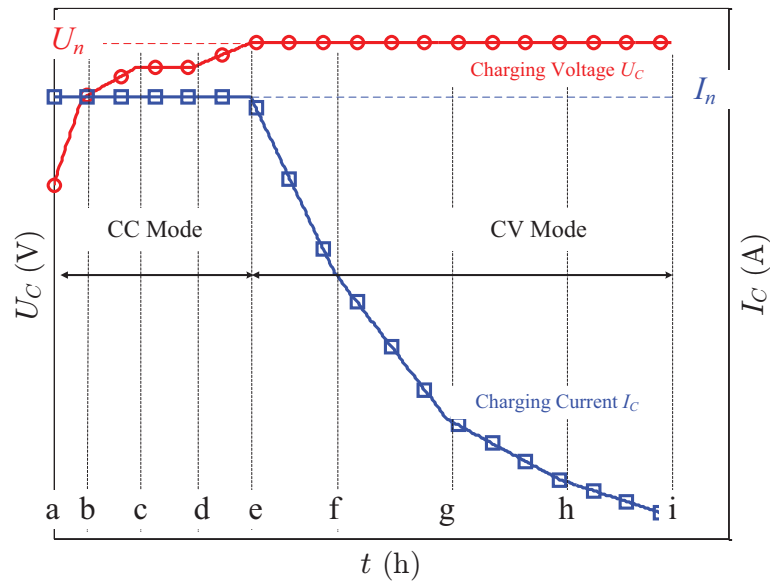
Table 3.2: Charging Parameters

Time (h) [point in Fig. 11]	Current (A)	Voltage (V)
0 [a]	$yC$	$3x$
0.125 [b]	$yC$	$3.725x$
0.375 [c]	$yC$	$4x$
0.625 [d]	$yC$	$4x$
0.875 [e]	$yC$	$4.2x$
1.25 [f]	$0.6yC$	$4.2x$
1.75 [g]	$0.27yC$	$4.2x$
2.25 [h]	$0.133yC$	$4.2x$
2.75 [i]	$0.05yC$	$4.2x$

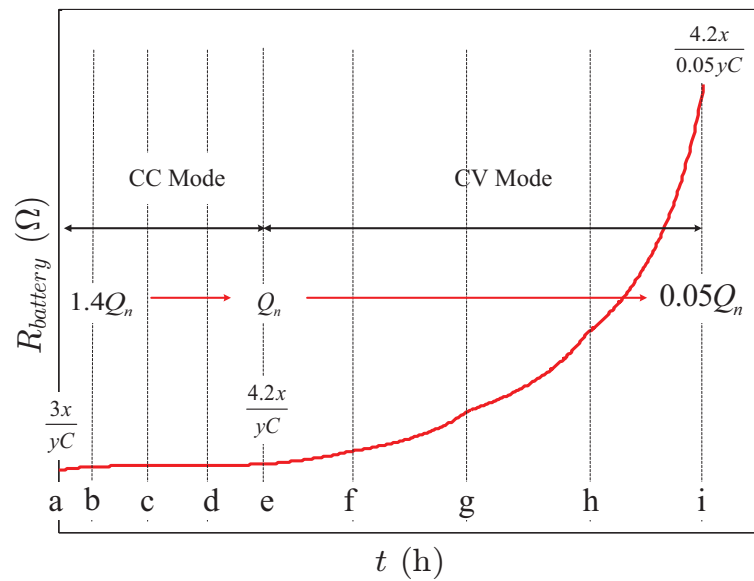
We have done extensive numerical calculations to obtain an optimum  $Q_{n,o}$  that corresponds to  $\eta_{\text{overall}}(Q_{n,o}) = \max(\eta_{\text{overall}})$ . Interestingly, there is no observable change in  $Q_{n,o}$  for a range of  $Q_P$  and  $Q_S$  from 10 to 5000. Therefore, it is safe to omit  $Q_P$  and  $Q_S$  in obtaining  $Q_{n,o}$ . To facilitate design, Fig. 3.12 presents  $Q_{n,o}$  versus  $k$  graphically. In Fig. 3.12, the red curve plots  $Q_{n,o}$  versus  $k$ , showing that  $Q_{n,o}$  is not a function of  $Q_P$  or  $Q_S$ . Moreover, when comparing  $Q_{n,o}$  with  $Q_{LCC}$ 's in (3.1) and (3.3),  $Q_{n,o}$  is a bit higher than  $\frac{1}{k}$  for all values of  $k$ . The blue curves show  $\max(\eta_{\text{overall}})$  versus  $k$  for different values of  $Q_P = Q_S$ . From Fig. 3.12, a higher overall efficiency can be achieved by using a transformer with higher  $k$ ,  $Q_P$  and/or  $Q_S$ .

### 3.3.2 Loosely-coupled Transformer

The loosely coupled transformer for stationary EV charging can be designed with a circular pad, a double-D pad, a double-D quadrature pad or a bipolar pad [5, 117]. The popular primary and secondary circular pad structures shown in Fig. 3.13 will be adopted. In this chapter, the circular pads of equal size have an outer diameter of  $d_o$ , inner diameter of  $d_i$  and a separation gap of  $g$ . For a given structure, a higher  $k$  can be achieved with a larger  $\frac{d_o}{g}$  and/or a larger



(a)



(b)

Figure 3.10: (a) Piecewise-linear battery charging profile; (b) piecewise-linear resistance of the battery during the whole charging profile.

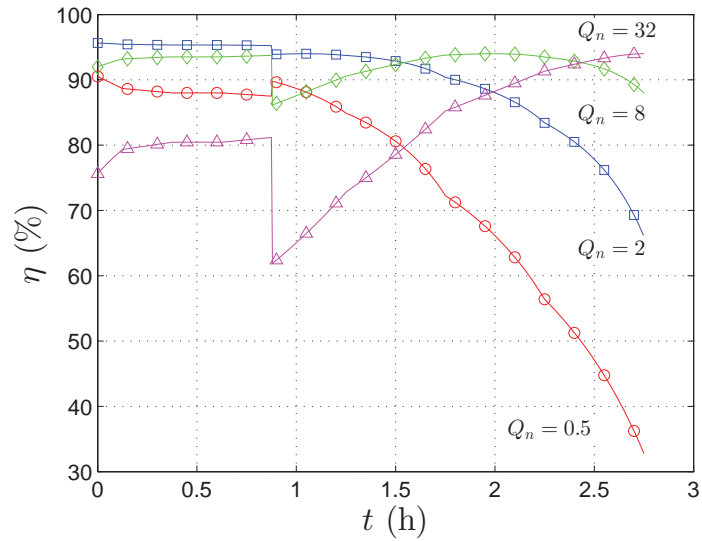


Figure 3.11: Charging efficiency  $\eta$  profile for different values of  $Q_n$ . Overall efficiency should be maximum at a particular  $Q_n$  denoted as  $Q_{n,o}$ .

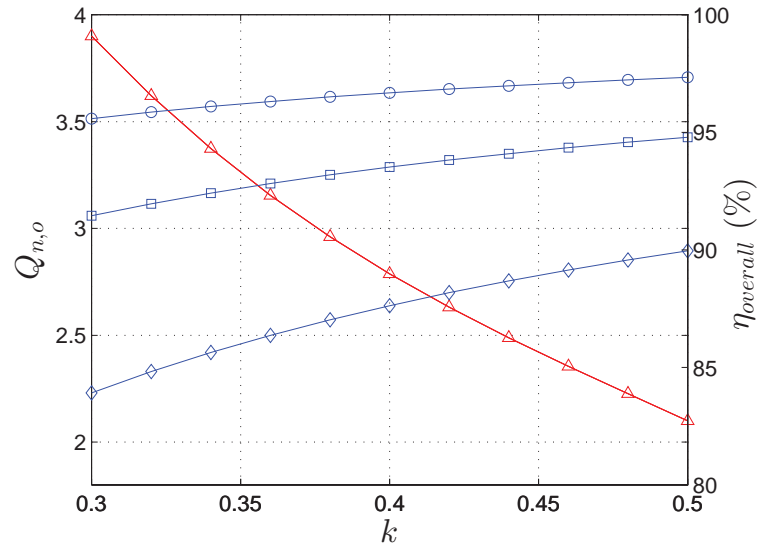


Figure 3.12: Design plot of  $Q_{n,o}$  vs.  $k$  (red), and corresponding  $\max(\eta_{\text{overall}})$  (blue), showing that  $\max(\eta_{\text{overall}})$  increases with increasing  $k$ ,  $Q_P$  and/or  $Q_S$ .

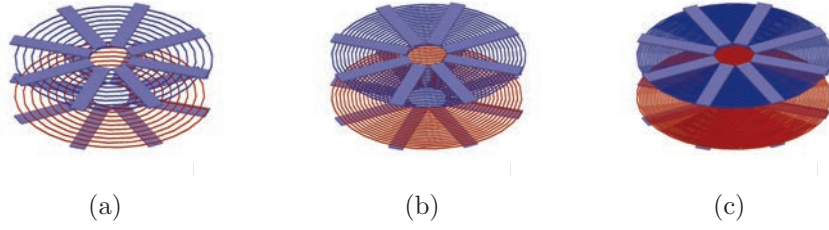


Figure 3.13: Circular unipolar coupled transformer with constant inner and outer radii and evenly distributed wire distance for (a)  $N = 10$ , (b)  $N = 20$  and (c)  $N = 40$ .

ferrite section area [117]. According to the overall charging efficiency indicated in Fig. 3.12, using a larger pad diameter and/or better magnetic and/or conducting material, a higher  $\eta_{\text{overall}}(Q_{n,o})$  can be achieved.

In Fig. 3.13, the simplified pad has two layers. The top layer contains the coil that generates magnetic field and the second layer contains the ferrite to reduce the reluctance. The two pads are arranged with a magnetic linking path  $h$ . It is assumed that the secondary pad is attached to the underside of an EV, while the primary pad is buried under the ground. Once an EV has stopped over the charging system, power is transferred across the air gap via magnetic coupling from the primary pad to the secondary pad.

The structure and the dimension of the loosely coupled transformer are usually designed according to some expected ranges of  $k$ ,  $L_P$  and  $L_S$ . We have performed Ansoft Maxwell simulations using the transformer structures shown in Fig. 3.13 with  $d_o = 500$  mm,  $d_i = 100$  mm,  $g = 100$  mm and the number of turns  $N = N_P = N_S$  of the coils varying from 5 to 40. Design curves shown in Fig. 3.14 show how  $k$  and  $L_S$  vary with  $N$ , which are consistent with the results shown in reference [181].

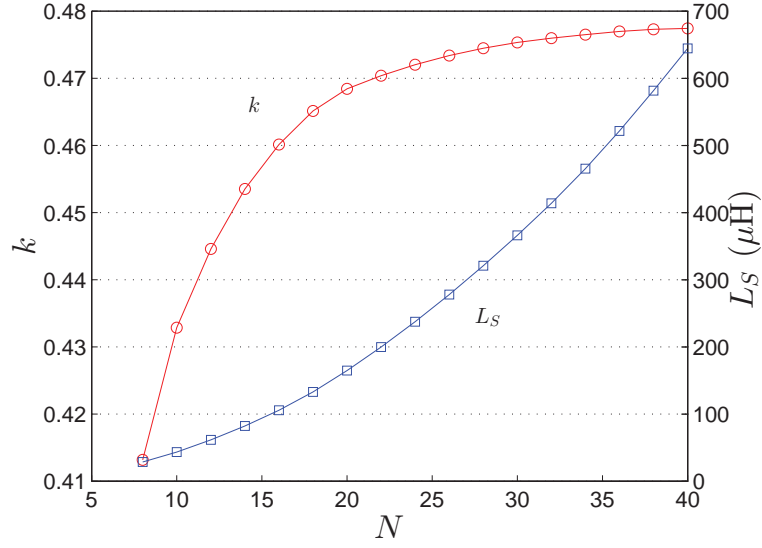


Figure 3.14: Coupling coefficient  $k$  and inductance  $L_S$  (or  $L_P$ ) vs. number of turns  $N$ .

### 3.3.3 Converter Design

Given an input voltage  $U_{\text{IN}}$ , the converter as shown in Fig. 3.9 provides the required charging current  $I_n$  and voltage  $U_n$  according to (3.20), (3.21) and the battery profile shown in Fig. 3.10. Here,  $Q_L$  varies from  $1.4Q_n$  to  $Q_n$  during CC mode of charging and from  $Q_n$  to  $0.05Q_n$  during CV mode of charging. Therefore, the design should satisfy (2.31) and (2.34), which are practically equivalent to

$$\begin{aligned} \frac{\pi^2 I_n}{8D_i(Q_L)U_{\text{IN}}} &= |G_i(\omega_P)|(1 - \Delta g(Q_L)) \\ &= \frac{1 - \Delta g(Q_L)}{\omega_P k \sqrt{L_P L_S}}, \text{ and} \end{aligned} \quad (3.24)$$

$$\begin{aligned} \frac{U_n}{D_v(Q_L)U_{\text{IN}}} &= |E_i(\omega_H)|(1 - \Delta e(Q_L)) \\ &= \Delta_H (1 - \Delta e(Q_L)) \sqrt{\frac{L_S}{L_P}}, \end{aligned} \quad (3.25)$$

where  $\Delta_H = \left| \frac{k(\mu^2 + 1 + \Delta)}{(2k^2 - 1)\mu^2 + 1 + \Delta} \right|$  is a function of  $k$  and  $\mu$  only and duty cycles  $D_i$  and  $D_v$  varying with  $Q_L$  are given in (3.19) for operation with LIC and LIV output, respectively. At rated power  $Q_L = Q_n$ , which corresponds to switching of CC

mode to CV mode, both (3.24) and (3.25) should be satisfied, giving

$$Q_n = \frac{\pi^2 I_n}{8 U_n} \sqrt{\frac{L_S}{C_S}} \quad (3.26)$$

$$= \frac{1}{k\mu} \frac{D_i(Q_n)}{D_v(Q_n)} \left( \frac{1 - \Delta g(Q_n)}{\Delta_H (1 - \Delta e(Q_n))} \right), \quad (3.27)$$

where  $Q_n$  should be designed close to  $Q_{n,o}$ , as obtained from (3.23) for the maximum overall charging efficiency (see Fig. 3.12). As  $R_n = \frac{U_n}{I_n}$  in (3.26) is fixed for a given battery, the converter can be designed with a suitable value of  $\frac{L_S}{C_S}$  for achieving  $Q_n = Q_{n,o}$ . According to the simulated results shown in Fig. 3.12,  $\max(\eta_{\text{overall}})$  increases with  $k$  at a reducing rate (saturates as  $k$  becomes large), and from Fig. 3.14,  $k$  also increases with  $L_S$  at a reducing rate. Hence, increasing  $L_S$  will offer diminishing return of  $\max(\eta_{\text{overall}})$ . We may therefore use  $X = \frac{\Delta k}{\Delta N} = 0.001$  as an indicator for choosing an initial value of  $N$  or  $L_S$ . Other indicators may also be adopted for design [5, 117]. The value of  $\omega_S = \frac{1}{\sqrt{L_S C_S}}$  obtained in (3.26) should be verified as being within the efficient operating range of the magnetics, switches, etc. Otherwise, a better choice of  $N$  or  $L_S$  should be used.

Duty cycles  $D_i(Q_n)$  and  $D_v(Q_n)$  at rated power loaded by  $Q_n$  should be designed close to 1 for best efficiency. For the reasons analyzed in Section 3.2, the LIC operating point has a much tighter tolerance than the LIV operating point for soft switching implementation. Therefore,  $D_i(Q_n)$  should be given priority and set as 1. Thus, from (3.24) and (3.25), we have

$$\frac{I_n}{U_{\text{IN}}} = \frac{8}{\pi^2} \frac{1 - \Delta g(Q_n)}{\omega_P k \sqrt{L_P L_S}}, \text{ and} \quad (3.28)$$

$$\frac{U_n}{U_{\text{IN}}} = D_v(Q_n) \Delta_H (1 - \Delta e(Q_n)) \sqrt{\frac{L_S}{L_P}}. \quad (3.29)$$

The values of duty cycles  $D_i(1.4Q_n)$  at the beginning of the CC charging mode

Table 3.3: Design Specification

Name	Parameter	Value
Input voltage	$U_{\text{IN}}$	$\approx 190$ V
Nominal charging voltage	$U_n$	175 V
Nominal charging current	$I_n$	6.4 A
Air gap distance	$g$	100 mm
Transformer outer diameter	$d_o$	500 mm

and  $D_v(0.05Q_n)$  at the end of the CV charging mode are thus given by

$$D_i(1.4Q_n) = \frac{1 - \Delta g(Q_n)}{1 - \Delta g(1.4Q_n)}, \text{ and} \quad (3.30)$$

$$D_v(0.05Q_n) = D_v(Q_n) \frac{1 - \Delta e(Q_n)}{1 - \Delta e(0.05Q_n)}. \quad (3.31)$$

According to Fig. 3.6(a), the implementation of soft switching by using  $\mu < 1$  in CC mode comes with an efficiency penalty as studied in Section 3.2.1. In practice,  $\mu$  can be assigned as 0.96. Using (3.15),  $\theta_{CC}(Q_n, \mu)$  and  $\theta_{CC}(1.4Q_n, \mu)$  can be obtained which should be larger than  $2 \cos^{-1} \{D_i(Q_n)\}$  and  $2 \cos^{-1} \{D_i(1.4Q_n)\}$ , respectively. Otherwise, a smaller  $\mu$  should be assigned with additional efficiency penalty. Thus, soft switching during CC mode of charging is guaranteed. Using (3.17),  $\theta_{CV}(Q_n)$  and  $\theta_{CV}(0.05Q_n)$  can be obtained, which should be larger than  $2 \cos^{-1} \{D_v(Q_n)\}$  and  $2 \cos^{-1} \{D_v(0.05Q_n)\}$  respectively. Thus, soft switching during CV mode can also be guaranteed. A more detailed illustration will be given in Section 3.4.

## 3.4 Experiment Evaluation

### 3.4.1 Experiment

Two prototypes of an 1.5 kW IPT system with and without soft switching during CC mode of operation for EV battery charging, as shown in Fig. 3.15, are built with design specifications given in Table 3.3. Switching devices used

Table 3.4: Comparison of Calculated and Measured Transformer and Circuit Parameters

Parameter	Calculated		Measured	
$k$	0.468		0.447	
$N_P$	20		20	
$N_S$	20		20	
$L_P$	163 $\mu\text{H}$		163.46 $\mu\text{H}$	
$L_S$	163 $\mu\text{H}$		161.96 $\mu\text{H}$	
$\mu$	0.96	1	0.96	1
$Q_{n,o}$	2.4	2.4	2.43	2.43
$C_P$	63.48 nF	58.50 nF	61.70 nF	61.70 nF
$C_S$	59.04 nF	59.04 nF	57.56 nF	61.96 nF
$f_P$	49.41 kHz	51.47 kHz	50.11 kHz	50.11 kHz
$f_H$	67.88 kHz	69.21 kHz	70.09 kHz	68.79 kHz
Parameter	Calculated		Measured	
$\mu$	0.96	1	0.96	
$\Delta g(Q_{n,o})$	0.0159	0.0153	0.0157	
$\Delta e(Q_{n,o})$	0.0381	0.0409	0.0386	
$D_i(Q_{n,o})$	1	1	1	
$D_v(Q_{n,o})$	1	0.9570	1	
$U_{\text{in,min}}$	191.66 V	191.54 V	186.5825	
$\Delta g(1.4Q_{n,o})$	0.0115	0.0110	0.0113	
$D_i(1.4Q_{n,o})$	0.9955	0.9957	0.9956	
$2 \cos^{-1} \{D_i(Q_{n,o})\}$	$0^\circ$	$0^\circ$	$0^\circ$	
$2 \cos^{-1} \{D_i(1.4Q_{n,o})\}$	$10.8640^\circ$	$10.6477^\circ$	$10.7883^\circ$	
$\theta_{CC}(Q_{n,o})$	$10.7700^\circ$	$0^\circ$	$10.5200^\circ$	
$\theta_{CC}(1.4Q_{n,o})$	$14.8975^\circ$	$0^\circ$	$14.5536^\circ$	
$\Delta e(0.05Q_{n,o})$	0.0021	0.0023	0.0021	
$D_v(0.05Q_{n,o})$	0.9640	0.9613	0.9634	
$2 \cos^{-1} \{D_v(Q_{n,o})\}$	$0^\circ$	$33.7273^\circ$	$0^\circ$	
$2 \cos^{-1} \{D_v(0.05Q_{n,o})\}$	$30.8603^\circ$	$31.9918^\circ$	$31.0901^\circ$	
$\theta_{CV}(Q_{n,o})$	$36.2488^\circ$	$34.3081^\circ$	$35.8358^\circ$	
$\theta_{CV}(0.05Q_{n,o})$	$85.2603^\circ$	$84.9369^\circ$	$85.2000^\circ$	

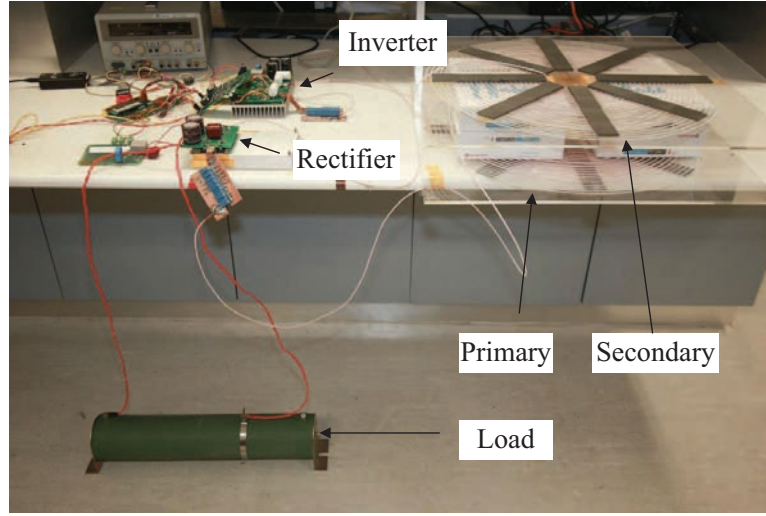


Figure 3.15: Experimental prototype of the IPT system.

are Infineon CoolMOS IPW60R199CP with  $R_{on} = 0.041 \Omega$ . Rectifier devices are STMicroelectronics STTH60AC06C with  $V_F = 0.8 \text{ V}$  at rated power. The loosely coupled transformer is constructed according to Section 3.3.2 using Litz wire AWG38 with  $N_P : N_S = 20 : 20$ . The calculated and measured transformer parameters are shown in Table 3.4. The measured parameters will be used for the subsequent design. The winding resistances are measured near the calculated operating frequencies. i.e.,  $R_{P_w} = 293 \text{ m}\Omega$  and  $R_{S_w} = 298 \text{ m}\Omega$  at  $f_P = \frac{\omega_P}{2\pi}$ ; and  $R_{P_w} = 379 \text{ m}\Omega$  and  $R_{S_w} = 378 \text{ m}\Omega$  at  $f_H = \frac{\omega_H}{2\pi}$ . These give the winding quality factors of approximately 174 at 50 kHz and 185 at 68.5 kHz. The equivalent resistance  $R_P$  for the model can be obtained as  $R_P = R_{P_w} + 2R_{on}$  [173], which gives  $Q_P = 136$  at  $f_P = 50 \text{ kHz}$  and 152 at  $f_H = 68.5 \text{ kHz}$ . In contrast,  $Q_S$  is determined by the windings resistance only. Moreover, the loss due to the rectifier diodes can be modeled as a voltage source of  $2V_F$  connected in series with the battery. Essentially, the quality factors of this transformer stay between the models of constant resistance and constant quality factor described in Section 3.2.1. With the parameters  $k$ ,  $Q_P$  and  $Q_S$  measured,  $Q_{LCC}$  can be obtained from (3.1) or (3.3), and  $Q_{LCV}$  can be obtained from (3.2) or (3.4).

Two prototype converters are designed with  $\mu = 0.96$  and 1. Since the physical

transformers have  $k = 0.447$ ,  $Q_{n,o}$  can be read from Fig. 3.12 as 2.4. From (3.26),  $C_S$  is calculated as 59.04 nF for the two converters. Compensation capacitors  $C_S$  and  $C_P$  are measured. Their values are shown in Table 3.4. Using  $\Delta g$  and  $\Delta e$  determined from (3.5) and (3.7),  $D_i(Q_{n,o})$  can be assigned as 1 and  $D_v(Q_{n,o})$  can be obtained as shown in Table 3.4 according to (3.27).

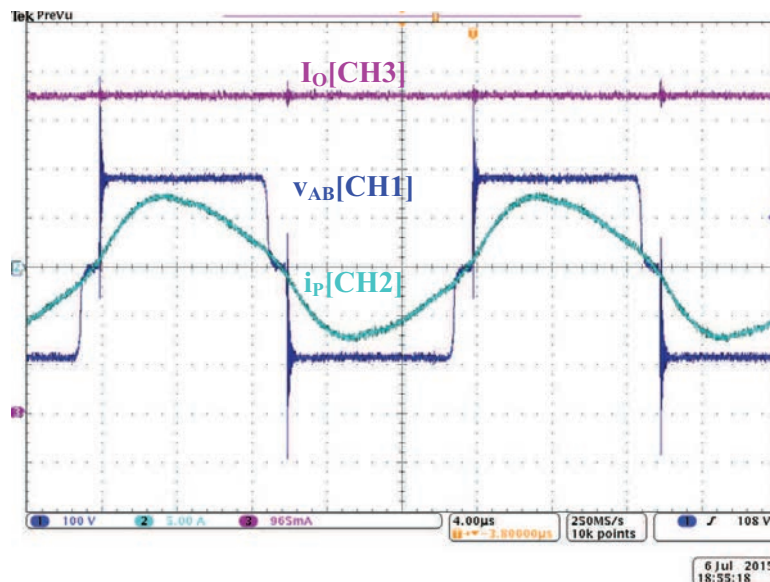
The rated output voltage  $U_n$  and current  $I_n$  can be scaled up or down with a suitable value of  $U_{IN}$  by using (3.6), (3.7) and (3.28), (3.29). The value of  $U_{in,min}$  can be uniquely determined in this design. However, if (3.28) and (3.29) give two significantly distinct values of  $U_{in,min}$  for CC and CV charging, the design should be re-iterated with some appropriated values of  $L_P$  and  $L_S$ .

Using (3.15),  $\theta_{CC} > 2 \cos^{-1} \{D_i(Q_n)\}$  is checked for  $Q_n$  varying from  $Q_{n,o}$  to  $1.4Q_{n,o}$ . Hence, soft switching during LIC operation is guaranteed for the converter designed with  $\mu = 0.96$ . Using (3.17),  $\theta_{CV} > 2 \cos^{-1} \{D_v\}$  is verified for  $Q_n$  varying from  $0.005Q_{n,o}$  to  $Q_{n,o}$ . Hence, soft switching during LIV operation is also guaranteed for the converter designed with  $\mu = 0.96$ . The values calculated are shown in Table 3.4, where it is observed that the converter with  $\mu = 1$  does not have soft switching during LIC output operation.

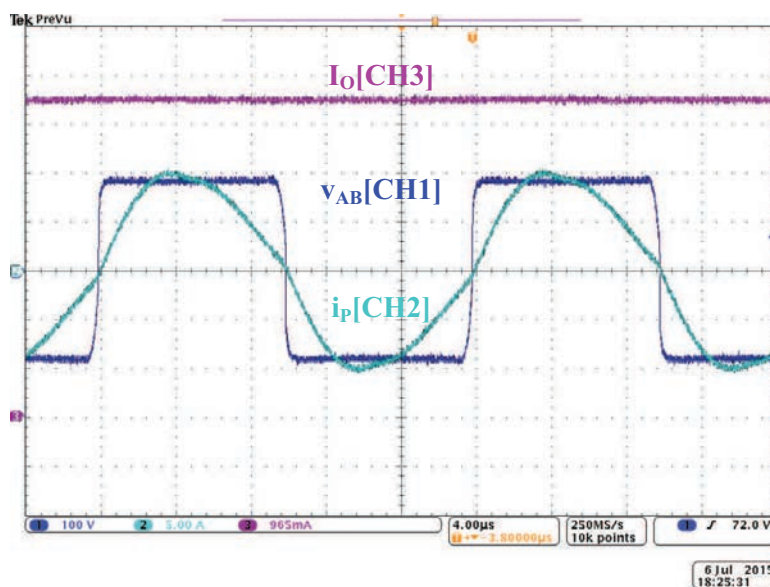
### 3.4.2 Soft Switching in LIC and LIV Operation

Using the prototype IPT converter designed with  $\mu = 1$ , waveforms of the converter at the start and end of the CC charging stage are shown in Figs. 3.16(a) and 3.16(b), respectively. It can be observed that soft switching is still achievable in Fig. 3.16(b), but Fig. 3.16(a) shows hard switching. Moreover, with  $\mu = 0.96$ , corresponding waveforms are shown in Figs. 3.17(a) and 3.17(b), which clearly show ZVS operation.

Using the prototype IPT converter designed with  $\mu = 1$ , waveforms of the converter at the start and end of the CC charging stage are shown in Figs. 3.18(a)

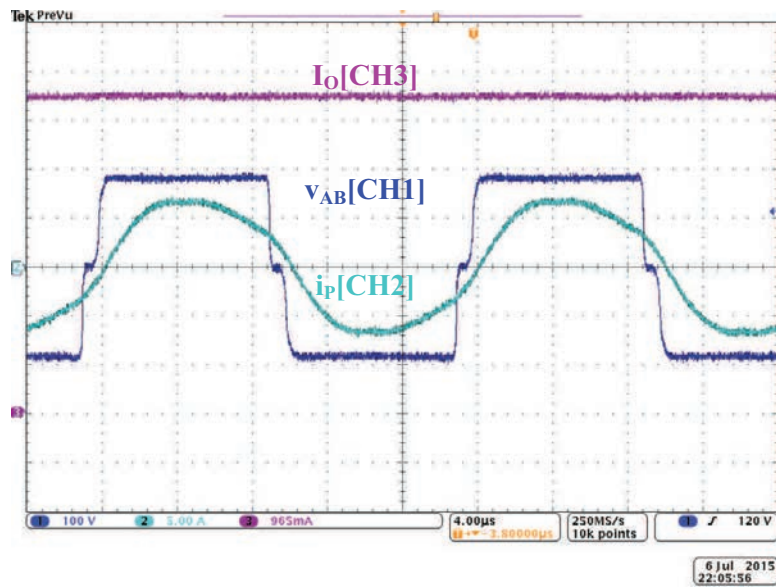


(a)

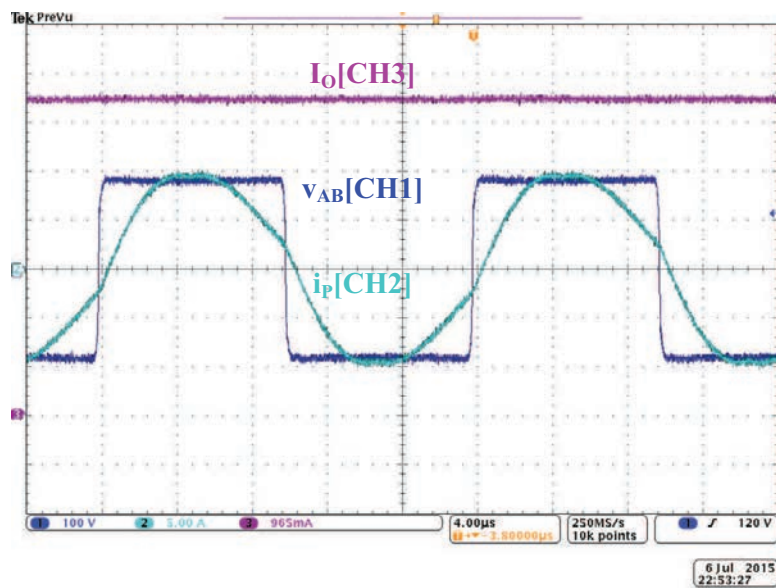


(b)

Figure 3.16: Waveforms of  $v_{AB}$ ,  $i_P$  and  $I_O$  at (a) start and (b) end of CC charging mode of the IPT converter designed with  $\mu = 1$ .

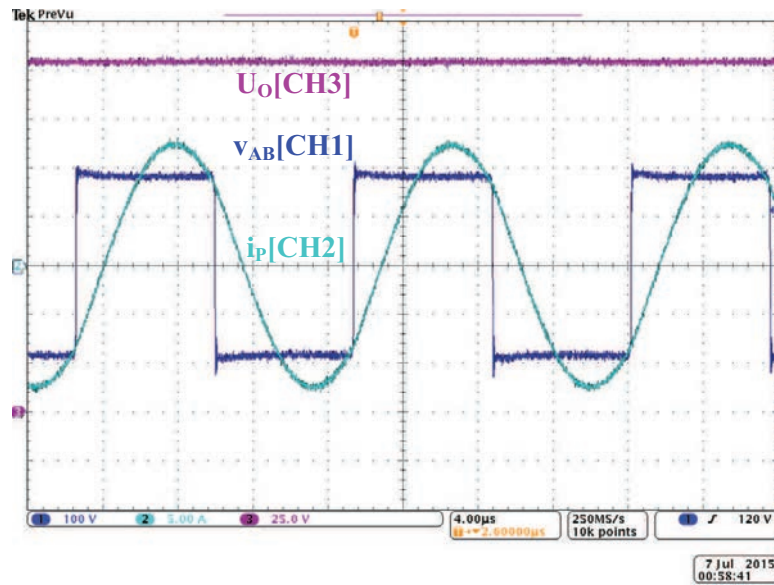


(a)

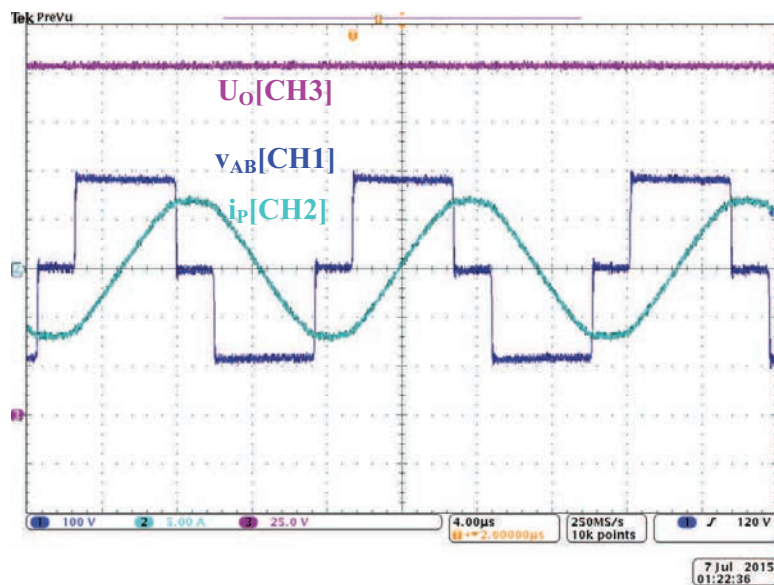


(b)

Figure 3.17: Waveforms of  $v_{AB}$ ,  $i_P$  and  $I_O$  at (a) start and (b) end of CC charging mode of the IPT converter designed with  $\mu = 0.96$ .

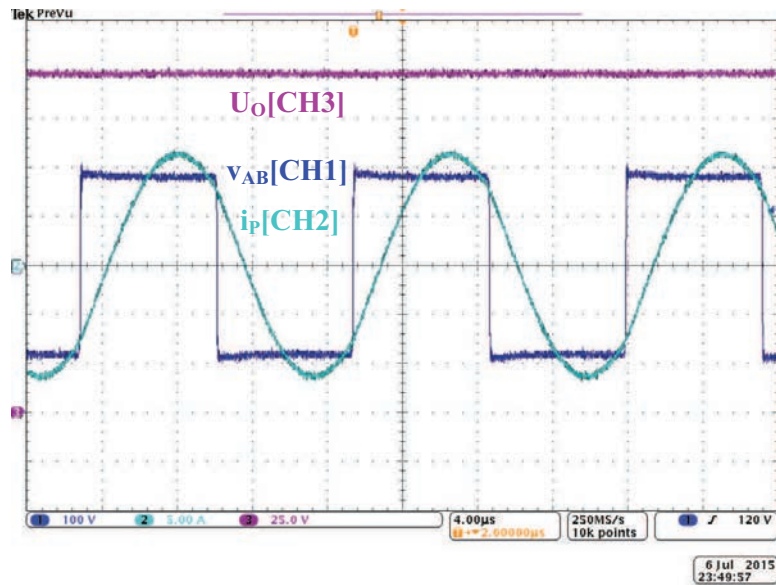


(a)

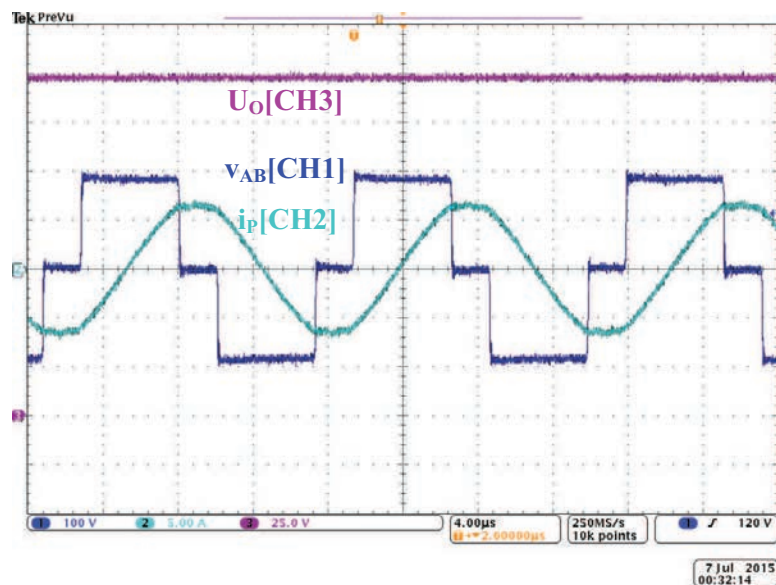


(b)

Figure 3.18: Waveforms of  $v_{AB}$ ,  $i_P$  and  $I_O$  at (a) start and (b) end of CV mode of charging of the IPT converter designed with  $\mu = 1$ .



(a)



(b)

Figure 3.19: Waveforms of  $v_{AB}$ ,  $i_P$  and  $I_O$  at (a) start and (b) end of CV mode of charging of the IPT converter designed with  $\mu = 0.96$ .

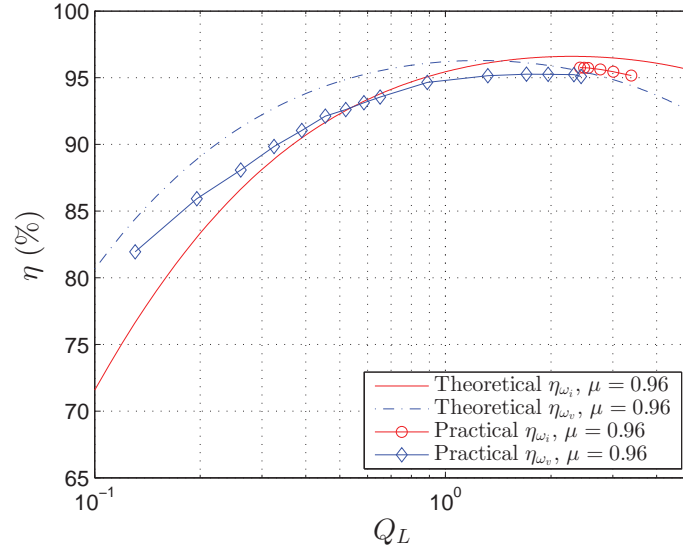


Figure 3.20: Measured charging efficiency  $\eta$  versus load quality factor  $Q_L$ .

and 3.18(b), respectively. Also, for  $\mu = 0.96$ , corresponding waveforms are shown in Fig. 3.19(a) and 3.19(b). All waveforms of LIV operation show ZVS.

### 3.4.3 Efficiency

A comparison of the calculated and measured efficiencies of the converter with  $\mu = 0.96$  for the load quality factor varying from 0.11 to 3.08 of the battery charging profile is shown in Fig. 3.20. The efficiencies have been measured using two Voltech PM100 power analyzers, one for the DC input power and the other for the DC output power. Theoretical calculations are shown in solid curve for CC output and dashed curve for CV output. Practical measurements are marked with ‘o’ for CC mode and with ‘o’ for CV mode. The reasons for the practical efficiency being lower than the theoretical efficiency for both LIC and LIV operations are

- turn-on switching loss is not completely eliminated after employing ZVS,
- turn-off switching loss is not considered in the model,
- the output rectifying diode-bridge has nonlinearity which cannot be fully

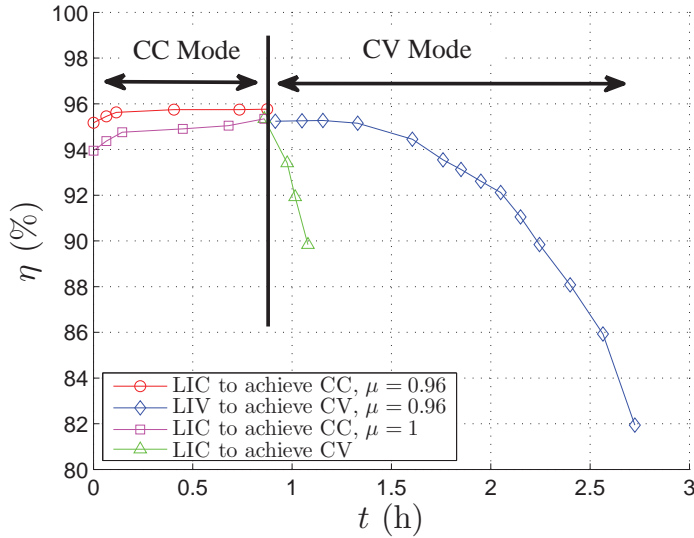


Figure 3.21: Measured charging efficiency  $\eta$  versus time  $t$ .

represented by a single loading resistor  $R_L$ ,

- the model only considers the fundamental frequency component and omits all other components, and
- the rectifying diodes have forward voltage  $V_F$  varying with the load, which has not been considered in the loss calculation.

The experimental charging efficiency versus time of the two prototype converters are shown in Fig. 3.21. The converter with  $\mu = 0.96$  achieving ZVS gives a higher charging efficiency (marked with ‘o’) while the hard switching converter with  $\mu = 1$  gives lower charging efficiency (marked with ‘□’) in CC charging mode. When the LIC output converter is controlled to operate in CV mode, the measured efficiency (marked with ‘△’) decreases rapidly due to the required fast decrease of duty cycle at lighter load conditions and the converter ends up with hard switching. In Fig. 3.21, only four hard switching ‘△’ data points are shown for the LIC operation providing a constant output voltage. The measured efficiency points (marked with ‘◇’) are the same data points appeared in Fig. 3.20. There is no observable change in measured efficiency of the LIV

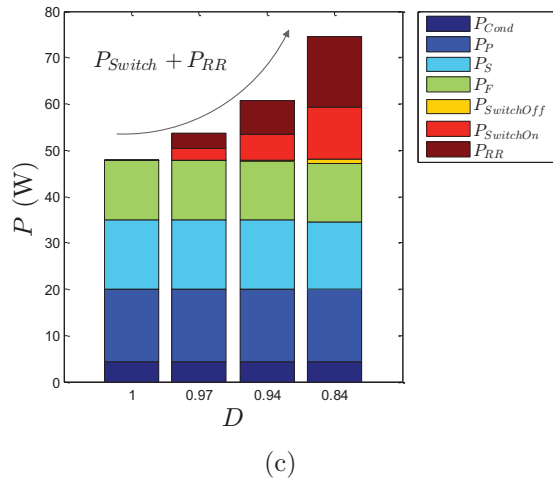
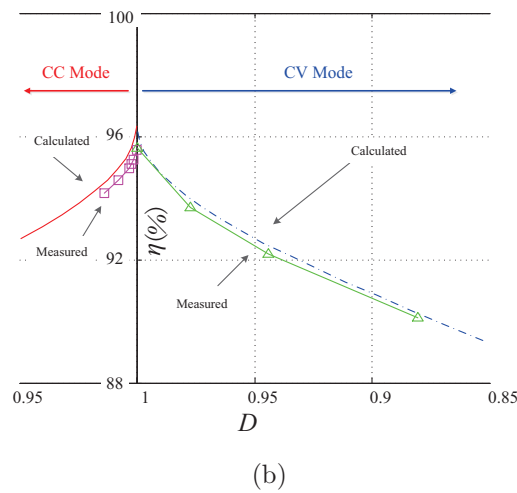
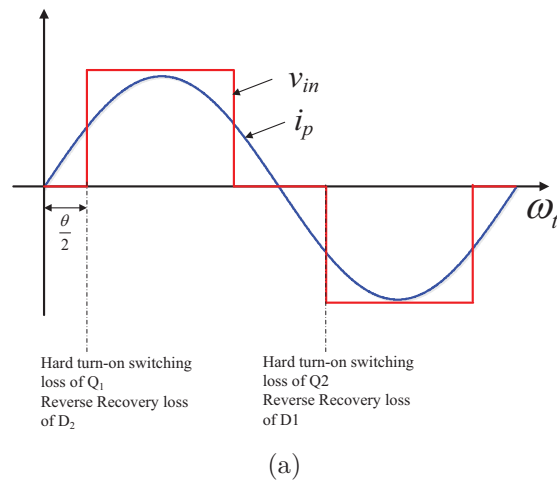


Figure 3.22: Loss components estimation. (a) Illustrative voltage and current waveforms at the two phase legs of the H-bridge. (b) Measured charging efficiency  $\eta$  versus duty cycle  $D$  with LIC operation with  $\mu = 1$ . The LIC output is regulated by varying  $D$  to provide the required constant output current for CC mode and the required constant output voltage for CV mode. (c) Estimated loss components versus  $D$ , where  $P_{Switch} = P_{SwitchOn} + P_{SwitchOff}$ .

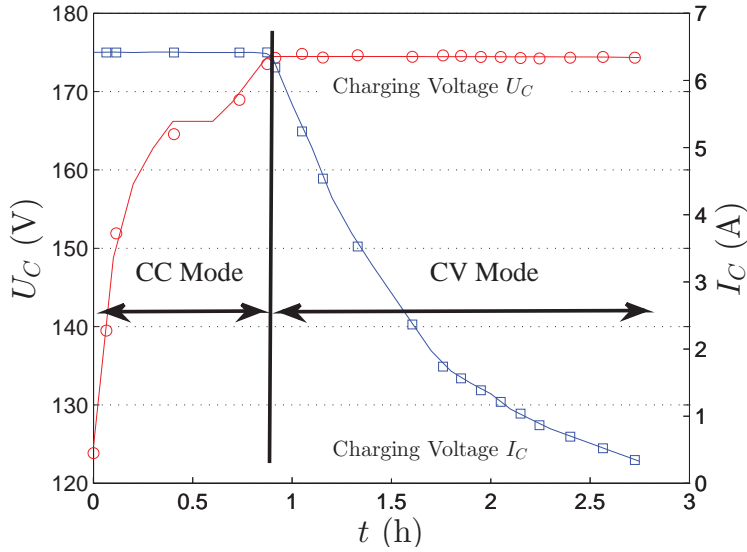


Figure 3.23: Measured charging profiles of voltage  $U_C$  and current  $I_C$ .

output for the two prototype converters.

The losses in hard switching can be analyzed in terms of the typical square voltage waveform  $v_{in}$  after modulation and the current waveform  $i_P$  of the H-bridge inverter, as shown in Fig. 3.22(a). The switching loss and diode reverse recovery loss during switching are estimated assuming a phase angle of  $\frac{\theta}{2}$ . Power losses included in the calculation are switching loss  $P_{Switch}$ , diode reverse recovery loss  $P_{RR}$ , conduction loss  $P_{Cond}$ , primary winding loss  $P_P$ , secondary winding loss  $P_S$  and forward voltage drop loss  $P_F$  of the rectifier diodes [182]. The power efficiency is thus estimated as  $\eta = \frac{P_O}{P_O + P_{Switch} + P_{Cond} + P_{RR} + P_P + P_S + P_F}$ . A comparison of the calculated and previously measured efficiency of the prototype converter with  $\mu = 1$  is given in Fig. 3.22(b). Since the duty cycles required for CV output by using the LIC operating point is well below the ZVS limit of  $D = 0.995$  for the prototype converter with  $\mu = 0.96$ , a converter with a much smaller  $\mu$  than 0.96 is needed to achieve soft switching. Fig. 3.22(c) shows the loss components versus  $D$ , which verifies that the additional losses, i.e.  $P_{SW} + P_{RR}$ , due to hard switching increases significantly with decreasing  $D$ . In contrary, the efficiency gained from

soft switching is unable to counteract the extra loss incurred by using a much smaller  $\mu$ , as explained in Section 3.2.1. Hence, the converter operating with LIC output has a narrow range of control by using PWM modulation and is unsuitable for use as a CV output converter.

As a final remark, the converter operating efficiently with LIC output has a tight modulation margin which is only good for achieving soft switching against load variation. This supports the view that implementation cases (C2) and (C4) of battery charging cannot achieve high efficiency as described in Section 3.1. Fortunately, the charging current needs not be precise [183], and thus as long as the current rating of the battery has been taken care of, the converter can be left uncontrolled at its maximum duty cycle. If a precise output current is needed against input voltage variation, a fixed-frequency-on-off control can be utilized for this converter [184]. Finally, the experimental charging voltage and charging current versus time for the ZVS converter with  $\mu = 0.96$  are shown in Fig. 3.23. The overall experimental charging efficiency is found to be 94.5%.

### 3.5 Summary

An IPT EV charging system, which is based on a single compensated topology and two fixed operating frequencies, has been described in this chapter. The series-series capacitor compensation topology has the characteristics of load-independent current output and load-independent voltage output at two different operating frequencies, which are suitable for constant-current charging and constant-voltage charging of the EV battery, respectively. Analysis and design for efficiency optimization have been studied in depth, and experimental evaluation of a 1.5 kW IPT EV battery charger has been reported.



## Chapter 4

# Control Design for Optimizing Efficiency

In Chapter 3, a single topology IPT converter is designed for EV battery charging by operating at LIC and LIV. However, this design is not suitable for general applications which usually have arbitrary variation of coupling coefficient and output power. Therefore, this chapter will go into a general multi-stage IPT system and propose a simple and fast voltage control scheme for efficiency optimization and power control. Such IPT system can be used in arbitrary applications with variations of coupling coefficient and load condition.

Design and optimization of inductive power transfer (IPT) systems have been widely studied. One of the main objectives is to achieve high efficiency. The optimization involves the choice of appropriate structure of magnetic couplers [117] and their interoperability [121]. It is well known that a higher coupling coefficient and higher coil quality factors of the pair of windings of the magnetic coupler would increase the system efficiency [4, 185]. Optimization approaches for these two parameters to achieve high efficiency have been proposed [88, 186]. Meanwhile, since the system efficiency is not monotonically varying with the load, optimum loads that achieve maximum efficiency of the system are also

studied [50, 172, 173]. Moreover, various design aspects to achieve maximum efficiency for different converter transfer functions using series and parallel compensations have been studied [136, 137]. Previous studies show that given a coupling coefficient and coil quality factors, an IPT converter should be designed to operate at some fixed operating frequencies with load-independent transfer characteristic to modulate slightly for soft switching when a simple half-bridge or full-bridge inverter circuit is used, and to operate within a restricted load range in order to achieve maximum efficiency [134, 136, 137, 158]. Among the four basic types of compensation, the widely used *series-series* compensated IPT (SSIPT) converter is the most power efficient IPT converter when it is operating with load-independent output current [50, 134, 136, 137, 158, 172, 173]. However, in some practical applications, the design may not meet the required wide variations of the coupling coefficient, the load resistance and the load power. Thus, once an IPT converter has been designed at a particular coupling coefficient and a particular load, the efficiency of the IPT system cannot always be maintained near its maximum point.

To improve the system efficiency under variation of the load, a load-side DC/DC converter is connected between the load and the secondary of an SSIPT converter to adaptively control the equivalent load observed by the SSIPT converter, thus maintaining a maximum efficiency of the front-end power amplifier driver [164, 187]. To achieve output regulation, source modulation is needed. The modulation can be provided by either a pulse-width modulated inverter, a front-side DC/DC converter which amplitude-modulates the inverter circuit, or a power amplifier. The inverter circuit is mostly implemented by either a half-bridge or full-bridge circuit which provides the highest efficiency but suffers from shallow modulation due to the need for maintaining soft switching [136, 137, 173]. The depth of modulation can be greatly improved when the inverter is amplitude-modulated by a front-end DC/DC converter. The combined circuit incurs a

penalty of additional loss due to the extra power stage. The power amplifier can be considered as a circuit consisting of a front-side DC/DC converter, amplitude modulating an inverter circuit with an output filter. The study by Li *et al.* [163] shows that a system consisting of the SSIPT converter with front-side and load-side DC/DC converters (the system is denoted as F-SSIPT-L) can achieve better overall system efficiency compared to a system consisting of the same SSIPT converter and a load-side DC/DC converter utilizing the modulation of the internal inverter (such a system is denoted as M-SSIPT-L) with frequency modulation. A maximum efficiency tracking (MET) algorithm has been proposed by Li *et al.* [163], where the secondary DC/DC converter regulates the output voltage while the front-side DC/DC converter maximizes the system efficiency. Another MET algorithm has also been studied using the F-SSIPT-L system where the front-side DC/DC converter controls the input current of the SSIPT converter for better handling of small coupling coefficient and light load [165]. Furthermore, a MET algorithm has been applied to the inverter to minimize the input power of an M-SSIPT-L system where the load-side dc/dc converter solely regulates the output [160]. The benefit is that no wireless data feedback is needed from the secondary to the primary of the magnetic coupler. The MET control schemes studied so far are based on perturbation and observation (P&O) of the system power or the system efficiency [160, 163–165]. It is well known that P&O based control schemes are slow due to the uncertainties of perturbation speed and amplitude. Moreover, such control schemes are based on real-time processing of both voltage and current for obtaining information of power or efficiency, resulting in high error of the processed information and necessitating the use of cost-ineffective current sensor(s).

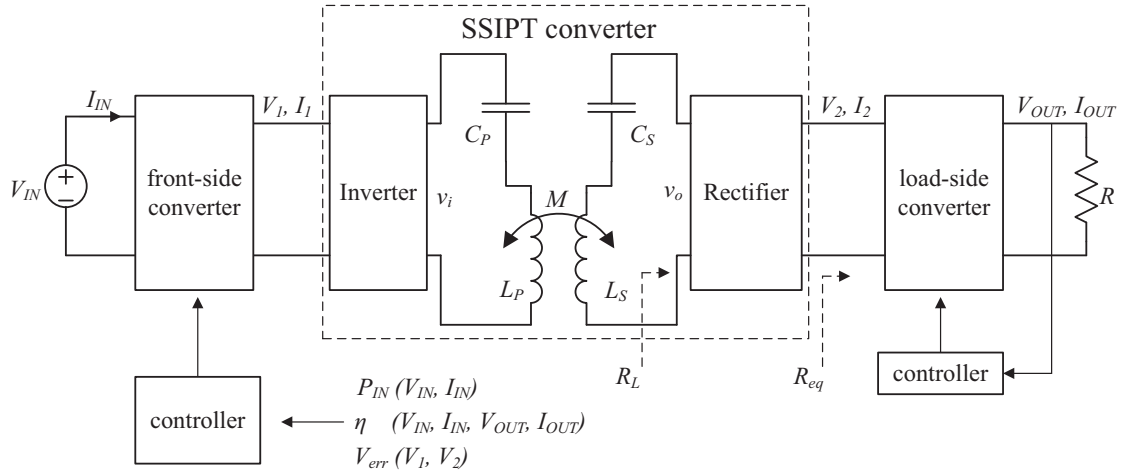


Figure 4.1: SSIPT converter cascaded with a front-side converter and a load-side converter.

## 4.1 Maximum IPT Converter Efficiency and Input-to-output Ratio

For simplicity, the SSIPT converter is normally designed to operate at the aligned resonant frequency, i.e.,  $\omega = \omega_P = \omega_S$ , where  $\omega_P$  and  $\omega_S$  are given in (2.12) and (2.13), respectively. As a result, the power efficiency  $\eta$  is maximized at a particular load quality factor  $Q_{L,opt}$  given in (2.19). Therefore, the optimum load resistance  $R_{L,opt}$  is therefore given by

$$R_{L,opt} = R_S \sqrt{1 + \frac{\omega^2 M^2}{R_P R_S}}. \quad (4.1)$$

The magnitude of the transconductance  $|G|$  at this operating frequency is given by

$$|G_{LIC}| = \frac{\omega_S M}{R_P (R_S + R_L) + \omega_S^2 M^2}. \quad (4.2)$$

The voltage transfer ratio at maximum efficiency is thus given by

$$\left| \frac{v_o}{v_i} \right| = |G_{\text{LIC}}| R_{L,\text{opt}} \approx \sqrt{\frac{R_S}{R_P}} \text{ for } \frac{\omega^2 M^2}{R_P R_S} \gg 1. \quad (4.3)$$

From (4.3), it is possible to maintain a high IPT converter efficiency by controlling the converter voltage ratio at  $\sqrt{\frac{R_S}{R_P}}$  against variation of the load.

## 4.2 SSIPT Converter Voltage Ratio Control

A general three-stage IPT system is illustrated in Fig. 4.1 [160,163,165]. The IPT system includes a front-side dc/dc converter, an SSIPT converter and a load-side dc/dc converter. The operating frequency of the inverter is fixed at the resonant frequency to achieve maximum efficiency. The control functions of the three-stage system provide

1. regulation to the output voltage or current, and
2. control for maximum efficiency of the SSIPT converter.

Three control schemes with optimization functions  $P_{\text{IN}}$ ,  $\eta$  and  $V_{\text{err}}$  are shown in Fig. 4.1 and compared in Table 4.1. Dynamic response of P&O based controller are slow to track the maximum efficiency. Moreover, the output voltage and current of the IPT converter maybe overshoot or undershoot in response to variations of coupling coefficient or load condition. Some advantages of our proposed linear control method can be readily observed:

1. The control function versus modulated input  $m_1$  (duty cycle of the front-side converter) is monotonic with a well defined control reference  $V_{\text{err}} = 0$  to minimize the error voltage  $V_{\text{err}} = V_1 - \sqrt{\frac{R_P}{R_S}} V_2$ . With a proper design, a simple linear PI controller can be implemented with either analog or digital techniques. This results in a faster response.

2. The sampled voltages can be used for the linear PI controller without further processing. This results in a faster and more accurate response. Moreover, no current sensor is required, and the system cost is lower.

In view of the potential advantages of our proposed control, the details of our converter system are given subsequently. The steady-state operation of the converter system is studied in this section. Small signal analysis will be conducted in Section. 4.3.1. The load-side converter regulates the output voltage or current to the load  $R$  and it appears as a power load  $P_O$  at the output and sinusoidal magnitudes, we have  $\frac{1}{\omega M} = \left| \frac{i_o}{v_i} \right| = \frac{\frac{\pi}{2} I_2}{\frac{4}{\pi} V_1}$ , which gives

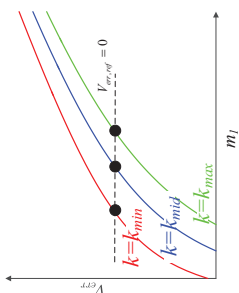
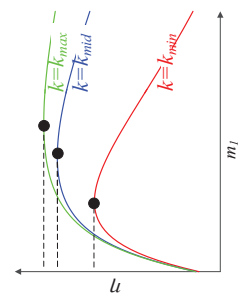
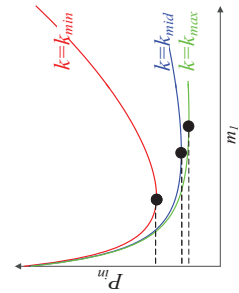
$$P_O = V_2 \frac{8}{\pi^2 \omega M} V_1. \quad (4.4)$$

To achieve (4.3), it is equivalent to minimize  $|V_{err}|$  given by

$$V_{err} = V_1 - \sqrt{\frac{R_P}{R_S}} V_2 = V_1 - \sqrt{\frac{R_P}{R_S}} \frac{P_O \pi^2 \omega M}{8 V_1}. \quad (4.5)$$

When using a front-side PWM converter,  $V_1$  is the modulated output of  $V_{IN}$  from a modulation index  $m_1 = \frac{V_1}{V_{IN}}$ . Monotonic curves for the control function  $V_{err}$  of (4.5) are shown in Table. 4.1 under different coupling coefficient  $k = \frac{M}{\sqrt{L_P L_S}}$ . linear PI controller can be used for its simple structure, better robustness and higher reliability. The design will be presented in Section.4.3.

Table 4.1: Comparison of Different control schemes

Voltage error control (this chapter)		Maximum efficiency tracking [163, 165]	Minimum input power tracking [160]
Control function			
Monotonicity	definitely $\frac{\Delta V_{err}}{\Delta m_l} > 0$	probing $\frac{\Delta \eta}{\Delta m_l}$ for signs	probing $\frac{\Delta P_{in}}{\Delta m_l}$ for signs
Control reference	$V_{err,ref} = 0$	adaptively tracking the maximum point.	adaptively tracking the minimum point.
Control method	PI controller, analog or digital	P&O, digital	P&O, digital
Sampling	$V_1, V_2$	$V_{IN}, I_{IN}, V_{OUT}, I_{OUT}$	$V_{IN}, I_{IN}$

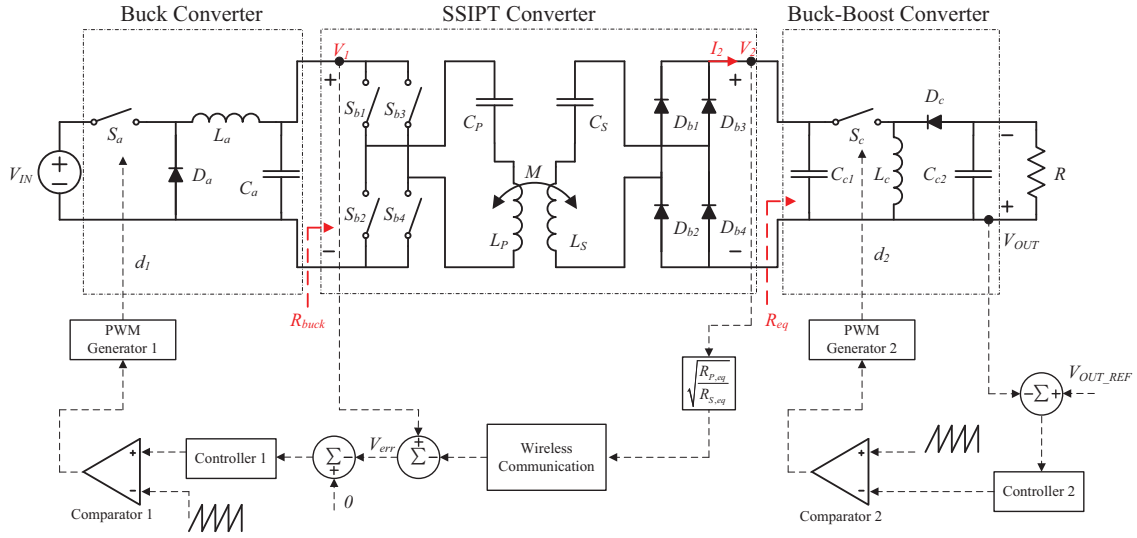


Figure 4.2: Schematic of the system.

### 4.3 Controller Design

Linear PI controllers will be designed to optimize the efficiency of the SSIPT converter system. Fig. 4.2 shows the schematic of the proposed control. For the SSIPT converter, an H-bridge inverter is used to generate an AC voltage at the resonant frequency. Thus, the SSIPT converter behaves as a transconductance converter. The current output is cascaded with a buck-boost converter which is regulated with a stand-alone PI controller to achieve a constant voltage output  $V_{OUT}$ . The front-side converter is a buck converter whose output voltage  $V_1$  drives the SSIPT converter. Voltages  $V_1$  and  $V_2$  of the SSIPT converter are sampled. No current sensor is needed here. Voltage  $V_2$  after scaled by a factor of  $\sqrt{\frac{R_P}{R_S}}$  is transmitted wirelessly from the secondary to the primary of the magnetic coupler and connected to the input of the PI controller of the buck converter. The voltage error  $V_{err}$  is controlled to be zero by the buck PI controller to attain maximum efficiency of the SSIPT converter.

At the optimal efficiency point, the steady-state parameters of the converters are calculated using  $R_{eq} = \frac{\pi^2}{8} \omega M \sqrt{\frac{R_S}{R_P}}$ ,  $R_{buck} = \frac{\pi^2}{8} \omega M \sqrt{\frac{R_P}{R_S}}$ ,  $V_2 = V_{OUT} \sqrt{\frac{R_{eq}}{R}}$ , and  $V_1 = V_{OUT} \sqrt{\frac{R_{buck}}{R}}$ , by assuming that all converters are lossless.

### 4.3.1 Small-signal Model of Transconductance

The small-signal transfer function of the SSIPT converter can be derived and calculated using the generalized averaging technique given in [188] for ordinary PWM and resonant power converters. Later, the same technique has been rephrased as dynamic-phasor model and applied for single-phase induction machines [189], microgrid systems [190] and extended for the perspective control of power converters [191]. Since the application of the generalized averaging technique or the dynamic-phasor model may not be obvious for the IPT converters, the procedure is highlighted as follows. A sinusoidal signal  $x(t)$  with time-varying magnitude  $X$  and phase angle  $\theta$  can be written by

$$x(t) = X \sin(\omega t + \theta) \quad (4.6)$$

$$= X [\cos \theta \sin \omega t + \sin \theta \cos \omega t] \quad (4.7)$$

$$= X_d \sin \omega t + X_q \cos \omega t \quad (4.8)$$

$$= \Im \left( (X_d + jX_q) e^{j\omega t} \right), \quad (4.9)$$

where  $X_d = X \cos \theta$ ,  $X_q = X \sin \theta$  are the direct and quadrature components of  $x(t)$ . The time functions of the slow time-varying properties of  $X$ ,  $\theta$ ,  $X_d$  and  $X_q$  are omitted for brevity. It can be readily shown that

$$\frac{dx(t)}{dt} = \Im \left\{ \left[ \left( \frac{dX_d}{dt} - \omega X_q \right) + j \left( \frac{dX_q}{dt} + \omega X_d \right) \right] e^{j\omega t} \right\}. \quad (4.10)$$

For a pure capacitor  $C$  having current  $i_C(t)$  and voltage  $v_C(t)$ , and a pure inductor  $L$  having current  $i_L(t)$  and voltage  $v_L(t)$ , the following basic relationships hold

$$i_C(t) = C \frac{dv_C(t)}{dt}, \text{ and} \quad (4.11)$$

$$v_L(t) = L \frac{di_L(t)}{dt}. \quad (4.12)$$

Substituting (4.9) and (4.10) into (4.11) and (4.12) and simplifying, we have

$$I_{C,d} + jI_{C,q} = C \left( \frac{dV_{C,d}}{dt} - \omega V_{C,q} \right) + j \left( \frac{dV_{C,q}}{dt} + \omega V_{C,d} \right), \text{ and} \quad (4.13)$$

$$V_{L,d} + jV_{L,q} = L \left( \frac{dI_{L,d}}{dt} - \omega I_{L,q} \right) + j \left( \frac{dI_{L,q}}{dt} + \omega I_{L,d} \right). \quad (4.14)$$

We can write  $x(t)$  as a complex vector given as  $\dot{X} = X_d + jX_q$ . Hence, (4.13) and (4.14) can be simplified at steady-state to become

$$\dot{I}_C = I_{C,d} + jI_{C,q} = j\omega \dot{V}_C, \text{ and} \quad (4.15)$$

$$\dot{V}_L = V_{L,d} + jV_{L,q} = j\omega \dot{I}_L, \quad (4.16)$$

which is commonly used in complex vector analysis. Obviously, (4.13) and (4.14) are vector transformations of (4.11) and (4.12). We can write (4.13) and (4.14) in matrix forms as

$$\mathbf{I}_C = C \left( \mathbb{I}_\omega + \frac{d}{dt} \right) \mathbf{V}_C, \text{ and} \quad (4.17)$$

$$\mathbf{V}_L = L \left( \mathbb{I}_\omega + \frac{d}{dt} \right) \mathbf{I}_L, \quad (4.18)$$

where  $\mathbf{X}_Y = [X_{Y,d}, X_{Y,q}]^T$  is a column vector and

$$\mathbb{I}_\omega = \begin{pmatrix} 0 & -\omega \\ \omega & 0 \end{pmatrix} \quad (4.19)$$

is a  $2 \times 2$  matrix.

The SSIPT system shown in Fig. 2.2(a) is governed by a state-space equation given as

$$\frac{d}{dt} X = AX + BV, \quad (4.20)$$

where

$$X = \begin{bmatrix} v_P(t) & v_S(t) & i_P(t) & i_S(t) \end{bmatrix}^T \quad (4.21)$$

$$V = \begin{bmatrix} v_i(t) & v_o(t) \end{bmatrix}^T \quad (4.22)$$

$$A = \begin{bmatrix} 0 & 0 & \frac{1}{C_P} & 0 \\ 0 & 0 & 0 & \frac{1}{C_S} \\ -\alpha_P & \beta & -\alpha_P R_P & \beta R_S \\ \beta & -\alpha_S & \beta R_P & -\alpha_S R_S \end{bmatrix} \quad (4.23)$$

$$B = \begin{bmatrix} 0 & 0 & \alpha_P & -\beta \\ 0 & 0 & -\beta & \alpha_S \end{bmatrix} \quad (4.24)$$

$$\alpha_P = \frac{1}{L_P(1 - k^2)}, \quad (4.25)$$

$$\alpha_S = \frac{1}{L_S(1 - k^2)}, \quad (4.26)$$

$$\beta = \frac{k}{(1 - k^2)\sqrt{L_P L_S}}, \quad (4.27)$$

Here,  $v_P(t)$  is the voltage of  $C_P$ ,  $v_S(t)$  is the voltage of  $C_S$ ,  $i_P(t)$  is the current of  $L_P$  and  $i_S(t)$  is the current of  $L_S$ . The SSIPT system has input  $v_i(t)$  and output  $v_o(t)$  powering load  $R_L$ . All state variables are sinusoidal.

Equation (4.20) can be readily vector transformed using (4.17) and (4.18) to obtain

$$\frac{d}{dt}\mathbf{X} = \mathbf{A}\mathbf{X} + \mathbf{B}\mathbf{V}, \quad (4.28)$$

where

$$\mathbf{X} = \begin{bmatrix} \mathbf{V}_P & \mathbf{V}_S & \mathbf{I}_P & \mathbf{I}_S \end{bmatrix}^T \quad (4.29)$$

$$\mathbf{V} = \begin{bmatrix} \mathbf{V}_I & \mathbf{V}_O \end{bmatrix}^T \quad (4.30)$$

$$\mathbf{A} = \begin{bmatrix} -\mathbb{I}_\omega & 0 & \frac{1}{C_P}\mathbb{I}_2 & 0 \\ 0 & -\mathbb{I}_\omega & 0 & \frac{1}{C_S}\mathbb{I}_2 \\ -\alpha_P\mathbb{I}_2 & \beta\mathbb{I}_2 & -\alpha_P R_P\mathbb{I}_2 - \mathbb{I}_\omega & \beta R_S\mathbb{I}_2 \\ \beta\mathbb{I}_2 & -\alpha_S\mathbb{I}_2 & \beta R_P\mathbb{I}_2 & -\alpha_S R_S\mathbb{I}_2 - \mathbb{I}_\omega \end{bmatrix} \quad (4.31)$$

$$\mathbf{B} = \begin{bmatrix} 0 & 0 & \alpha_P\mathbb{I}_2 & -\beta\mathbb{I}_2 \\ 0 & 0 & -\beta\mathbb{I}_2 & \alpha_S\mathbb{I}_2 \end{bmatrix}^T \quad (4.32)$$

where  $\mathbb{I}_2$  is the 2-dimensional identity matrix and variable  $\mathbf{X}_Y = (X_{Yr}, X_{Yi})^T$ .

A converter is cascaded with the SSIPT instead of a resistor. Assumed that the converter is well controlled to maintain a constant voltage or current output, it can be considered as a constant power load [192]. The extended describing function of  $\mathbf{V}_O$  is given

$$V_{O,d} = -2P_O \frac{I_{S,d}}{I_{S,d}^2 + I_{S,q}^2}, \quad (4.33)$$

$$V_{O,q} = -2P_O \frac{I_{S,q}}{I_{S,d}^2 + I_{S,q}^2}, \quad (4.34)$$

$P_O$  is the output power of the SSIPT. With (4.28), (4.33) and (4.34), The small signal model of (4.28) can be derived,

$$\begin{cases} \frac{d}{dt}\hat{\mathbf{X}} = \hat{\mathbf{A}}\hat{\mathbf{X}} + \hat{\mathbf{B}}\hat{\mathbf{V}}_I \\ \hat{\mathbf{I}}_O = \hat{\mathbf{C}}\hat{\mathbf{X}} \end{cases} \quad (4.35)$$

where

$$\hat{\mathbf{X}} = \begin{bmatrix} \hat{\mathbf{V}}_P & \hat{\mathbf{V}}_S & \hat{\mathbf{I}}_P & \hat{\mathbf{I}}_S \end{bmatrix}^T \quad (4.36)$$

$$\hat{\mathbf{V}}_I = \begin{bmatrix} \hat{\mathbf{V}}_{I,d} & \hat{\mathbf{V}}_{I,q} \end{bmatrix}^T \quad (4.37)$$

$$\hat{\mathbf{I}}_O = \begin{bmatrix} \hat{\mathbf{I}}_{O,d} & \hat{\mathbf{I}}_{O,q} \end{bmatrix}^T \quad (4.38)$$

$$\hat{\mathbf{A}} = \begin{bmatrix} -\mathbb{I}_\omega & 0 & \frac{1}{C_P}\mathbb{I}_2 & 0 \\ 0 & -\mathbb{I}_\omega & 0 & \frac{1}{C_S}\mathbb{I}_2 \\ -\alpha_P\mathbb{I}_2 & \beta\mathbb{I}_2 & -\alpha_P R_P\mathbb{I}_2 - \mathbb{I}_\omega & \beta(R_S\mathbb{I}_2 + \mathbb{I}_\delta) \\ \beta\mathbb{I}_2 & -\alpha_S\mathbb{I}_2 & \beta R_P\mathbb{I}_2 & -\alpha_S(R_S\mathbb{I}_2 + \mathbb{I}_\delta) - \mathbb{I}_\omega \end{bmatrix} \quad (4.39)$$

$$\hat{\mathbf{B}} = \begin{bmatrix} 0 & 0 & \alpha_P\mathbb{I}_2 & -\beta\mathbb{I}_2 \end{bmatrix}^T \quad (4.40)$$

$$\hat{\mathbf{C}} = \begin{bmatrix} 0 & 0 & 0 & -\mathbb{I}_\omega \end{bmatrix} \quad (4.41)$$

$$\mathbb{I}_\delta = \begin{pmatrix} P & -P \\ P & -P \end{pmatrix}, \text{ and} \quad (4.42)$$

$$P = 2P_O \frac{-i_{S,d}^2 + i_{S,q}^2}{(i_{S,d}^2 + i_{S,q}^2)^2}. \quad (4.43)$$

The frequency response of the transconductance of the SSIPT converter is plotted using Matlab with details shown in Fig. 4.3. It shows that, within a bandwidth of  $\frac{1}{100}$  of the fundamental frequency, the simulated transconductance can be approximated as the ideal transconductance  $\frac{1}{\omega M}$ , which is load-independent.

### 4.3.2 Voltage Error Control Loop

We define  $\hat{x}_y$  as small signal of  $X_y$ . Since the designed bandwidth of the control will be far lower than  $\frac{1}{100}th$  of the fundamental frequency, the SSIPT converter in Fig. 4.2 will be considered as a flat-frequency transconductance, given by

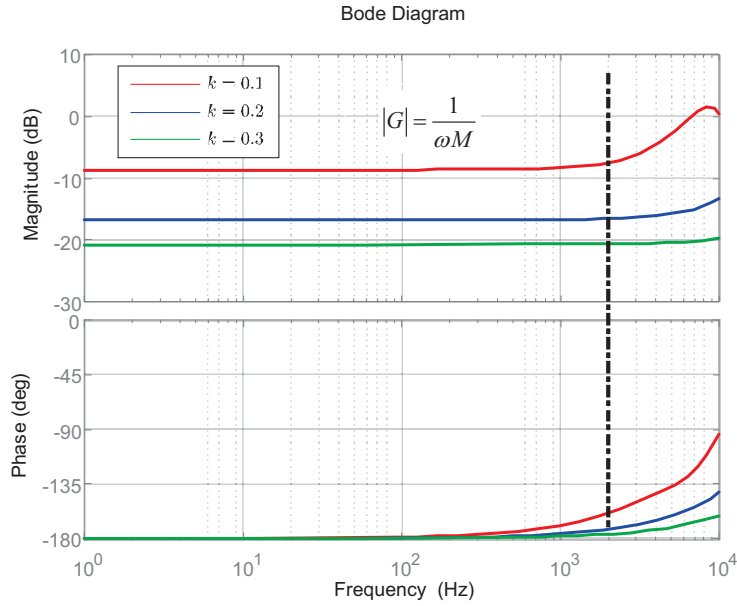


Figure 4.3: Simulated frequency response of transconductance of the SSIPT model. Parameters used in simulation are:  $L_P = L_S = 30 \mu\text{H}$ ,  $C_P = C_S = 21.11 \text{ nF}$ ,  $R_P = R_S = 0.5 \Omega$ ,  $\frac{\omega}{2\pi} = 200 \text{ kHz}$ ,  $v_i = 30\text{V}$  and  $P_O = 60\text{W}$ .

$$G_I = \frac{\hat{i}_2}{\hat{v}_1} = \frac{8}{\pi^2 \omega M}. \quad (4.44)$$

General wireless communication protocols, like 2.4G, are fast enough to transmit the output voltage  $V_2$  of the SSIPT converter, and time delay is not considered here [4]. The load-side buck-boost converter is assumed to be ideally controlled as a constant power load, and its input small-signal impedance is considered as a negative resistance  $-R_{eq}$  in this small-signal model [192]. Voltage  $\hat{v}_2$  is thus given as

$$\hat{v}_2 = \hat{v}_1 G_I (-R_{eq}) = -\hat{v}_1 \sqrt{\frac{R_S}{R_P}}. \quad (4.45)$$

From (4.3) and the bandwidth considered, the voltage error transfer function

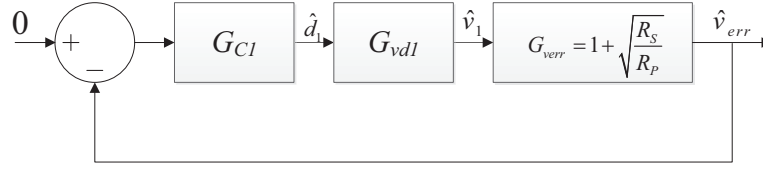


Figure 4.4: Block diagram of the voltage control loop of the cascaded buck-SSIPT converter system.

of the SS IPT converter is assumed as

$$G_{verr} = \frac{\hat{v}_1 - \hat{v}_2}{\hat{v}_1} = 1 + \sqrt{\frac{R_S}{R_P}}. \quad (4.46)$$

The input voltage  $\hat{v}_1$  of the SS IPT converter is controlled by the front-side buck converter in Fig. 4.2, the control to output transfer function of the buck converter is given by [193]

$$G_{vd1} = \frac{\hat{v}_1}{\hat{d}_1} = \frac{V_{IN}}{L_a C_a s^2 + \frac{L_a}{R_{buck}} s + 1}. \quad (4.47)$$

The control loop of the system is shown in Fig. 4.4. The transfer function of the input duty cycle  $\hat{d}_1$  to the voltage error  $\hat{v}_{err}$  is given by  $G_{vd1}G_{verr}$ , of which the Bode diagram is shown in Fig. 4.5(a). For this system, the design of compensator  $G_{C1}$  is similar to that of a buck converter [194]. Thus, a simple PI controller  $G_{C1}$  can be chosen as

$$G_{C1} = \frac{K_{PS} + K_I}{s}. \quad (4.48)$$

### 4.3.3 Stability Analysis

The open loop transfer function  $T$  of the front-side buck converter cascaded with the SS IPT converter is given by

$$T = G_{C1}G_{vd1}G_{verr}. \quad (4.49)$$

A third-order characteristic equation of the system is obtained by solving  $1 + T = 0$  as

$$a_3s^3 + a_2s^2 + a_1s + a_0 = 0. \quad (4.50)$$

where  $a_3 = L_a C_a$ ,  $a_2 = \frac{L_a}{R_{\text{buck}}}$ ,  $a_1 = (1 + \sqrt{\frac{R_s}{R_p}})K_P V_{\text{IN}} + 1$  and  $a_0 = (1 + \sqrt{\frac{R_s}{R_p}})K_I V_{\text{IN}}$ .

The load  $R$  and the coupling coefficient  $k$  usually vary within some ranges during operation. To have stable control,  $K_P$  and  $K_I$  should be designed to ensure system stability for all operating ranges. From the characteristic equation,  $R$  does not contribute to the design of  $K_P$  and  $K_I$ . An example design of the controller shown in Fig. 4.4 illustrates that all roots are located in LHP. Therefore, the stability of the system is ensured for  $k$  varying from 0.1 to 0.3.

## 4.4 Experiment Evaluation

An experimental prototype as shown in Fig. 4.6 is built to verify the linear control scheme and a version of P&O control scheme [160] is also implemented for comparison. The parameters of the schematic shown in Fig. 4.2 are given in Table 4.2.

### 4.4.1 Design of Control Parameters

When the magnetic coupler is designed without a magnetic core, the variation of the air gap distance has little effect on the self inductances. Thus, the

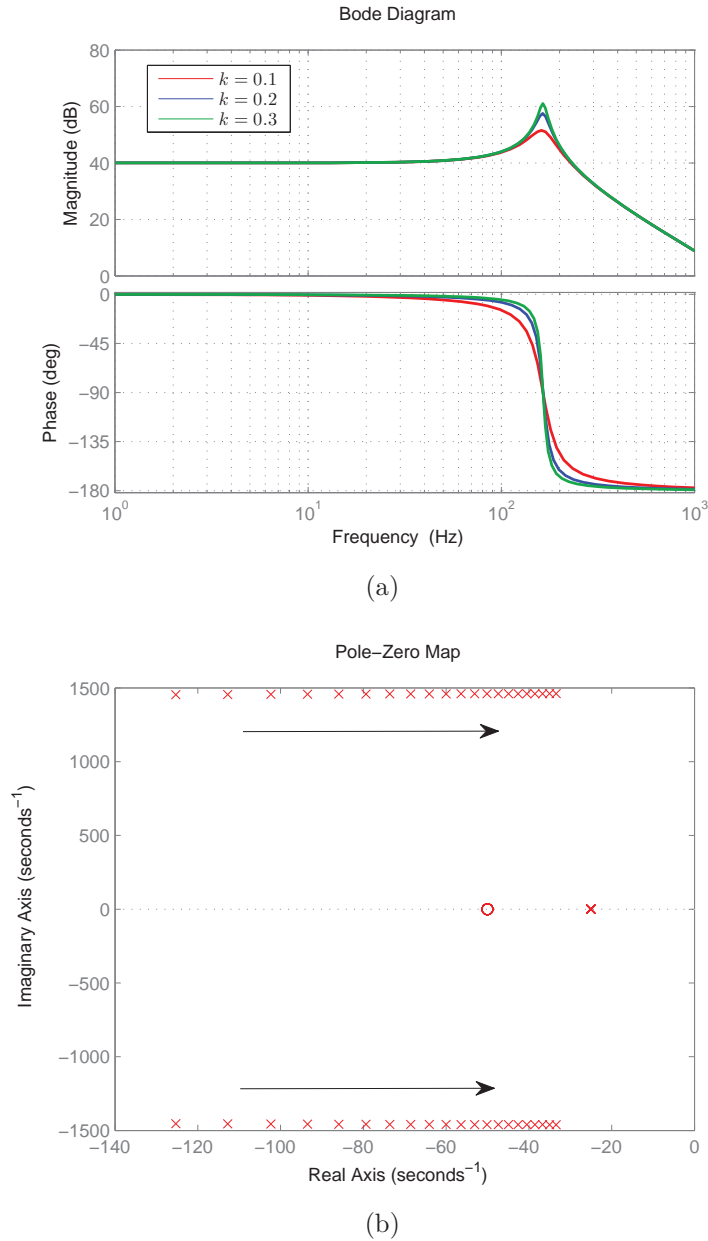


Figure 4.5: (a) Frequency response of  $\hat{v}_{\text{err}}$  versus  $\hat{d}$ . (b) Locations of pole (marked with 'x') and zero (marked with 'o') of the system with  $K_P = 0.01$ ,  $K_I = 0.5$ , when  $k$  increases from 0.1 to 0.3 as indicated by the arrow direction. Simulation parameters of the SSIPT converter are  $L_P = L_S = 30 \mu\text{H}$ ,  $C_P = C_S = 21.11 \text{ nF}$ , and  $\frac{\omega}{2\pi} = \frac{\omega_P}{2\pi} = \frac{\omega_S}{2\pi} = 200 \text{ kHz}$ . Parameters of the buck converter are  $L_a = 1.2 \text{ mH}$ ,  $C_a = 760 \mu\text{F}$ ,  $V_{\text{IN}} = 50 \text{ V}$ ,  $V_O = 30 \text{ V}$ , and  $R = 20 \Omega$ .

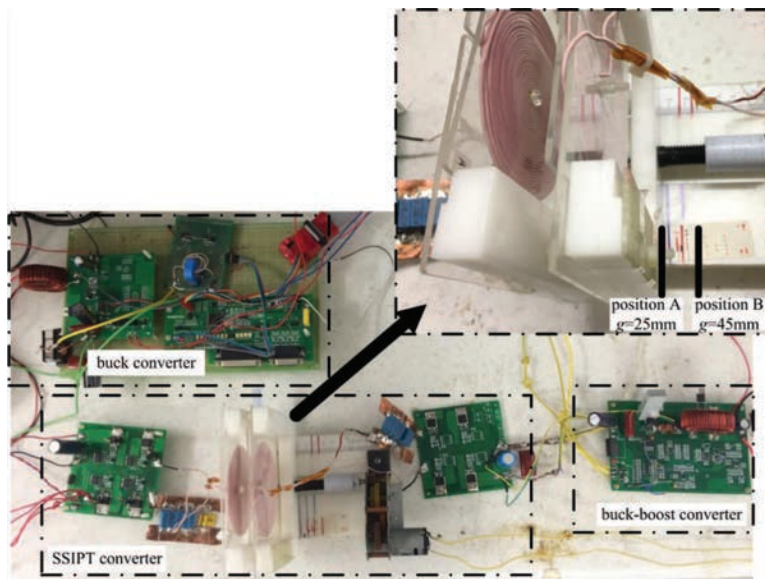


Figure 4.6: Experiment setup of the system and enlarged image of the loosely coupled transformer.

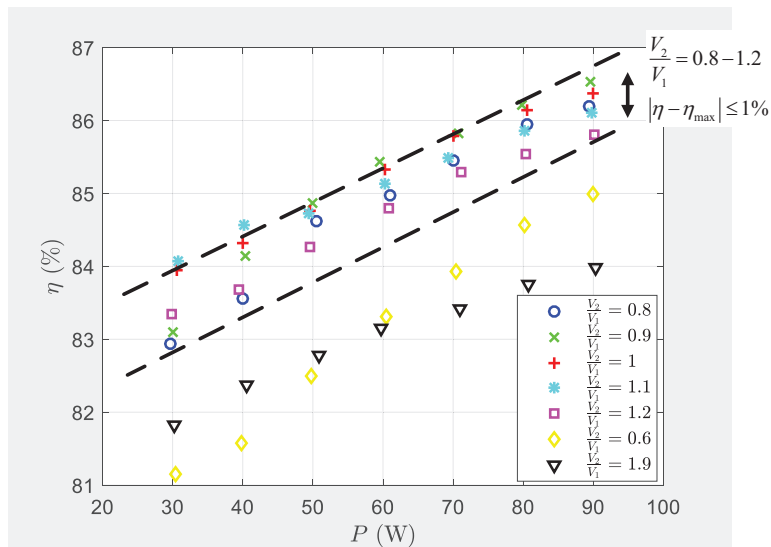
Table 4.2: Components and Parameters of the System

Converter	Parameters	Symbol	Value		
Buck	Switch	$S_a$	IRF540N		
	Diode	$D_a$	MBR20100CTG		
	Inductor	$L_a$	1.2 mH		
	Capacitor	$C_a$	780 $\mu$ F		
SSIPT	Switches	$S_{b1}-S_{b4}$	MTP5P06V		
	Diode	$D_{b1}-D_{b4}$	MBR20100CTG		
	Inner diameter	$d_i$	9 mm		
	Coil width	$w$	1.2 mm		
	Outer diameter	$d_o$	88 mm		
	Primary turns	$N_P$	29		
	Secondary turns	$N_S$	30		
	Air gap distance	$g$	45 mm	33 mm	25mm
	Coupling coefficient	$k$	0.1217	0.1739	0.2541
	Primary self inductance	$L_P$	31.48 $\mu$ H	31.477 $\mu$ H	31.467 $\mu$ H
	Secondary self inductance	$L_S$	32.98 $\mu$ H	32.974 $\mu$ H	32.955 $\mu$ H
	Primary winding resistance	$R_{P,w}$	245.8 m $\Omega$	245.76 m $\Omega$	245.59 m $\Omega$
	Secondary winding resistance	$R_{S,w}$	246.3 m $\Omega$	246.32 m $\Omega$	246.33 m $\Omega$
	Compensation capacitance	$C_P$	19.98 nF		
Compensation capacitance	$C_S$	19.08 nF			
Buck-boost	Switch	$S_c$	IRF540N		
	Diode	$D_c$	MBR20100CTG		
	Capacitor	$C_{c1}$	680 $\mu$ F		
	Inductor	$L_c$	1.2 mH		
	Capacitor	$C_{c2}$	470 $\mu$ F		

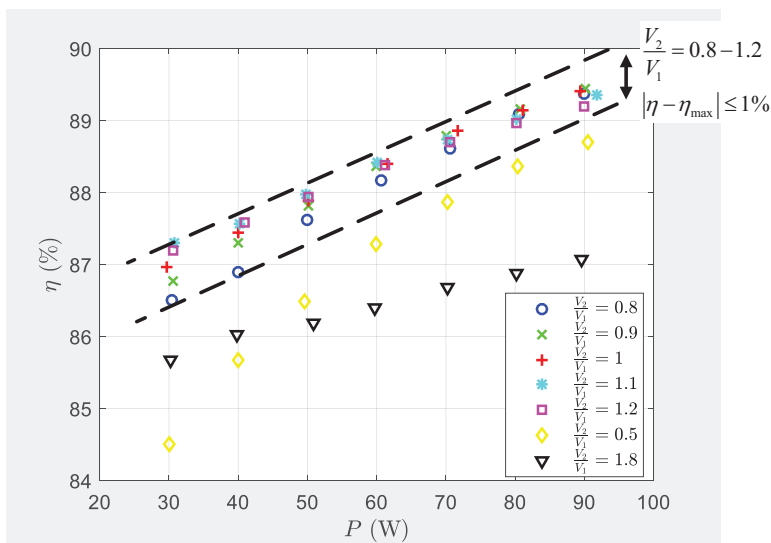
resonant frequency can be considered as constant and the operating frequency of the inverter can be fixed. However, when the magnetic coupler is designed with a magnetic core to improve the coupling coefficient, the variation of the air gap distance will affect the self inductances significantly [117]. Therefore, the operating frequency of the inverter should be dynamically adjusted to match the resonant frequency by using additional control, such as the self-oscillating control given in [145]. For the prototype studied in this chapter, since the magnetic coupler is designed without a magnetic core, the variation of the air gap distance has little effect on the self inductances, as shown in Table II, and no additional control for frequency adaptation is applied. The input voltage  $V_{IN}$  of this prototype is fixed at 50 V. The output voltage  $V_{OUT}$  is maintained at 30 V. A PI controller with  $K_P = 0.01$  and  $K_I = 0.5$  is designed for voltage control.

The SSIPT converter is designed to operate at zero input phase angle. Apart from the winding loss, additional loss to be incorporated into  $R_P$  from the inverter includes conduction loss from  $R_{on}$  and turn-on loss  $P_{switch-on}$  of the MOSFET switches. Additional loss to be incorporated into  $R_S$  includes loss due to the rectifier forward voltage  $V_F$ . Therefore,  $R_P$  and  $R_S$  in 4.3 are approximated as  $R_P \approx R_{P,\omega} + 2R_{on} + \frac{16P_{switch-on}}{\pi^2 I_1^2}$  and  $R_S \approx R_{S,\omega} + \frac{16V_F}{\pi^2 I_1^2}$  where  $R_{P,\omega}$  and  $R_{S,\omega}$  are the primary and secondary winding resistances, respectively, of the magnetic coupler.

The efficiency of the SSIPT converter is measured by a Yokogawa PX8000 Precision Power Scope. The buck-boost converter is closed loop controlled and the buck converter is also closed loop controlled with different control references. The efficiency curves of the SSIPT converter versus output power for different values of the voltage ratio are measured as shown in Fig. 4.7. At  $\frac{V_2}{V_1} = 1$ , near maximum efficiency (with less than 1% error) can be achieved under different loading conditions. Therefore,  $\frac{V_2}{V_1} = 1$  is used as the control reference for achieving maximum efficiency.



(a)



(b)

Figure 4.7: Measured efficiency of SSIPT converter versus output power under various voltage gains at (a)  $k = 0.1739$ , (b)  $k = 0.2541$ .

### 4.4.2 Small-Signal Response

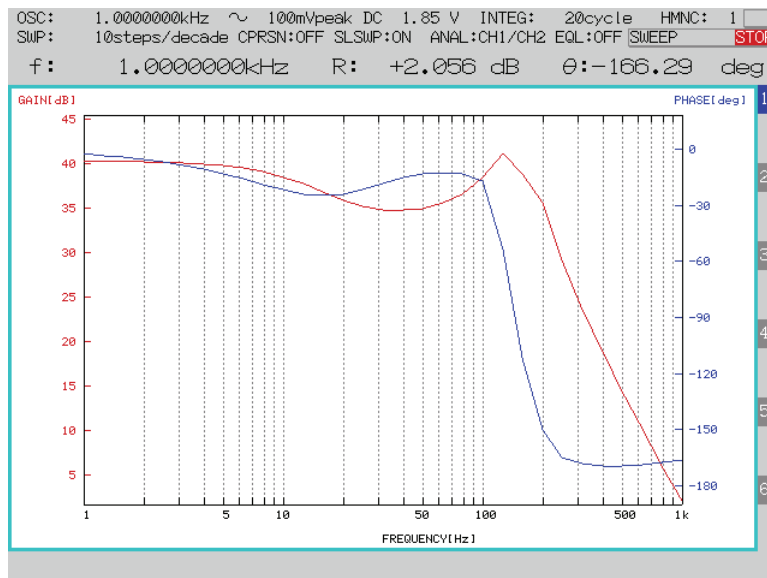
Fig. 4.8 shows the measured frequency response of the input duty cycle to the voltage error of the SSIPT converter. It matches the simulation result shown in Fig. 4.5(a) and verifies that the design of small-signal parameters of the controller for the cascaded buck-SSIPT converter can follow that of a buck converter.

### 4.4.3 Transient Response Against Variation of $k$

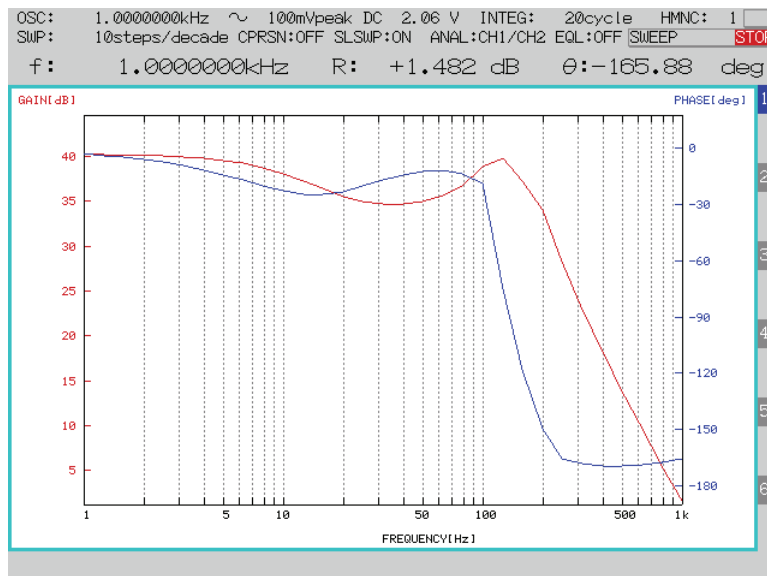
To show the performance of the proposed control, variation of the air gap distance is introduced by using a dc motor which dynamically varies the position of the secondary side coupler. In Fig. 4.6, an enlarged image shows the prototype of the loosely coupled transformer with position variation driven by a motor. At position A, the air gap distance  $g$  is 25 mm and the coupling coefficient  $k$  is 0.2541. At position B,  $g$  is 45 mm and the coupling coefficient  $k$  is 0.1217. More parameters of the loosely coupled transformer are shown in Table.4.2.

Experimental waveforms using voltage error control for the dynamical variation of  $g$  at a time scale of 2 s/div are shown in Fig. 4.9. The efficiency of the system is kept at its optimum by observing that the instantaneous voltages  $V_2$  and  $V_1$  are kept almost identical under variation of  $k$  (or  $g$ ).

As a comparison, experimental waveforms using an implementation of the minimum input current P&O control are also measured as shown in Fig. 4.10. The same variation speed of  $g$  as in Fig. 4.9 is used. In the minimum input current P&O control, a perturbation frequency 20 times faster than that adopted in [160] is used with the same perturbation size. Thus, the P&O control in this chapter is theoretically faster than that in [160]. Fig. 4.10 shows that, the instantaneous input current  $I_{IN}$  needs more than 8 second to settle to the steady-state solution. The response of this P&O control is much slower than the voltage error control proposed in this chapter against variations of  $k$ .

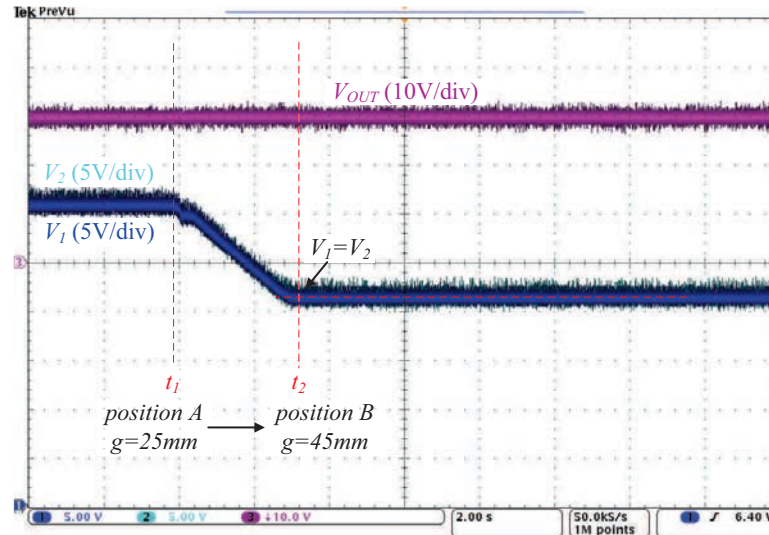


(a)

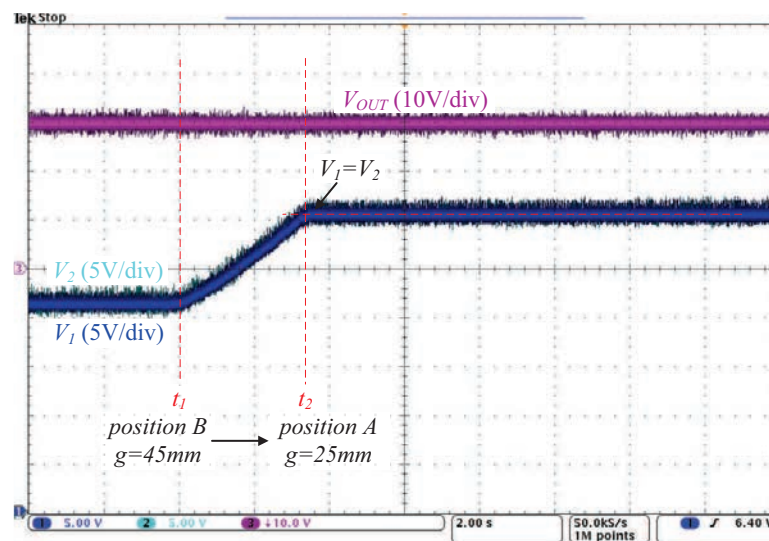


(b)

Figure 4.8: Measurements of the frequency response of input duty cycle to voltage error of the SSIPT at (a)  $k = 0.1739$ , (b)  $k = 0.2541$ .

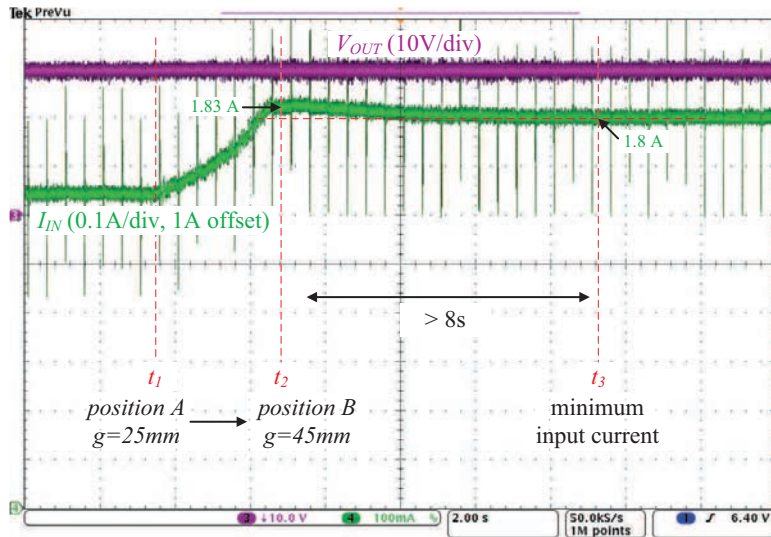


(a)

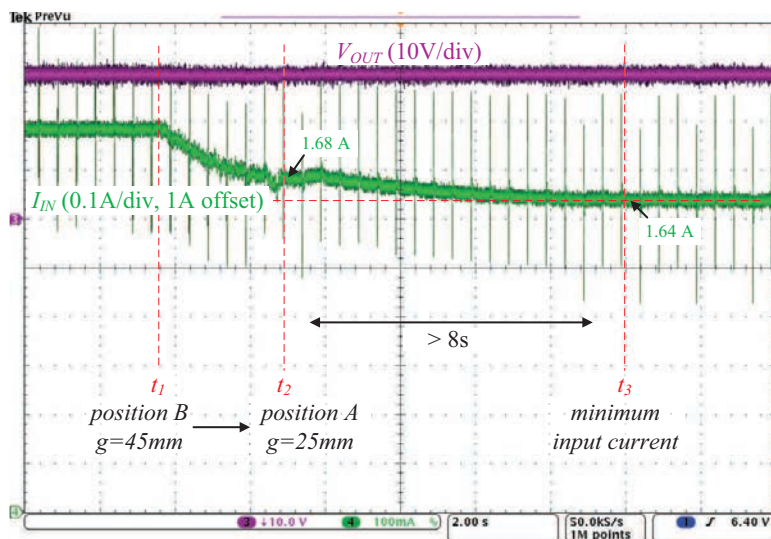


(b)

Figure 4.9: Transient waveforms of key control parameters of voltage error control with  $g$  dynamically changing (a) from 25 mm to 45 mm, (b) from 45 mm to 25 mm. The load resistance  $R$  is 10  $\Omega$ .



(a)



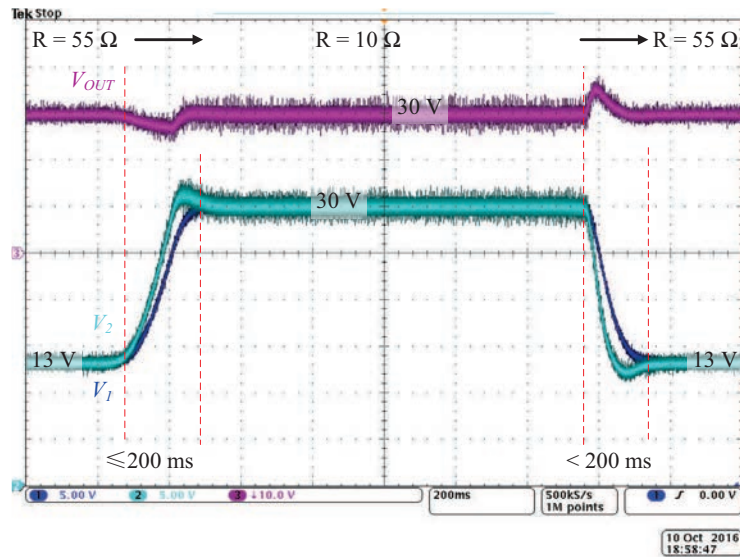
(b)

Figure 4.10: Transient waveforms of key control parameters of an implementation of the minimum input current P&O control with  $g$  dynamically changing (a) from 25 mm to 45 mm, (b) from 45 mm to 25 mm. The loading condition is  $R$  is 10  $\Omega$ .

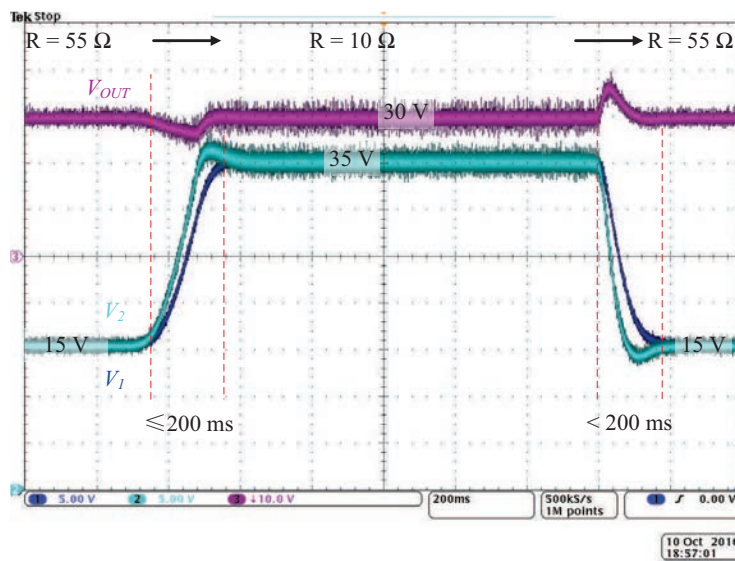
#### 4.4.4 Transient Response Against Load Variations

Fig. 4.11 shows the waveforms of voltage tracking processes of the load  $R$  switching from  $55\ \Omega$  to  $10\ \Omega$  and from  $10\ \Omega$  back to  $55\ \Omega$ . Using the PI controller, the steady-state error is eliminated. Within 300 ms, the input voltage  $V_1$  and the output voltage  $V_2$  are tracked, so that maximum efficiency of the system are maintained. We have performed experiments using the same parameters based on the P&O control implemented in Section.4.4.3. We found that the transient voltage fluctuations can be harmful to the converters. Therefore, a reduced load range switching from  $30$  to  $10\ \Omega$  is used for comparison of performance between the voltage error control and the P&O control. Four key parameters  $I_{IN}$ ,  $V_1$ ,  $V_2$  and  $V_{OUT}$  of the system as shown in Fig. 4.2 are chosen for the comparison of waveforms. In Fig. 4.12, the timebase is set at  $4\ \text{s/div}$ , the test systems are open loop before  $t_1$  with  $R = 30\ \Omega$ , the controls are applied after  $t_1$ , and the loads are switched to  $R = 10\ \Omega$  at  $t_2$ . Fig. 4.12(a) shows the transient waveforms when the voltage error control is used. It can be observed that  $V_{OUT}$  is always tightly regulated regardless of the excitations applied. This shows that the independently controlled load-side buck-boost converter can be stable with the input current  $I_2$  (not shown) and voltage  $V_2$  for the whole period of time indicated in Fig. 4.11(a). As soon as the voltage ratio control is applied at  $t_1$ ,  $\frac{V_2}{V_1}$  is immediately regulated at 1. At the same time,  $I_{IN}$  is also reduced immediately, thus improving the system efficiency. At  $t_2$ , the output power increases by threefold by switching the load resistance from  $30\ \Omega$  to  $10\ \Omega$ . The voltage ratio is rapidly followed and controlled with  $V_1 = V_2 = 30V$  at steady state.

Under the same experimental condition, the minimum input current P&O control produces the transient waveforms shown in Fig. 4.12(b). The system is completely out of control after  $t_2$  upon load switching. The system instability can be explained as follows. With the same initial condition as that of the voltage

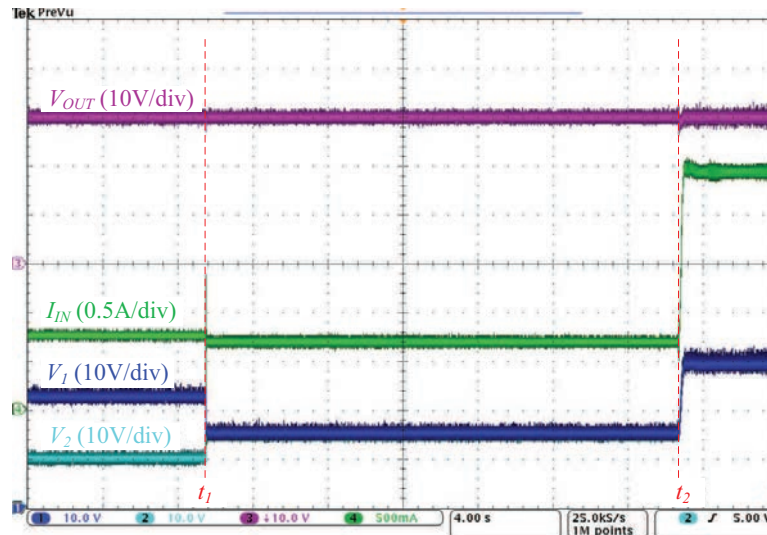


(a)

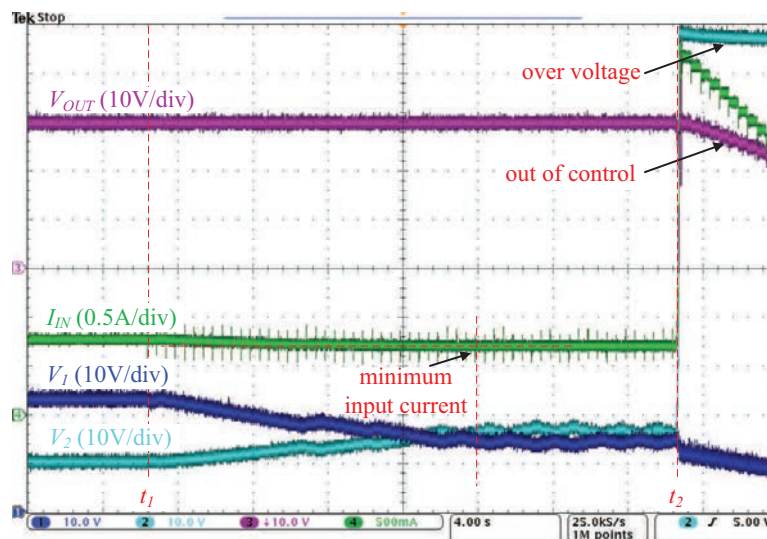


(b)

Figure 4.11: Transient waveforms of voltage tracking processes for  $R$  switching from  $55 \Omega$  to  $10 \Omega$  and from  $10 \Omega$  to  $55 \Omega$  at (a)  $k = 0.1739$ , (b)  $k = 0.2541$ .



(a)



(b)

Figure 4.12: Transient waveforms of (a) voltage error control, and (b) minimum input current P&O control. At  $t_1$ , the control is executed. At  $t_2$ , load resistance  $R$  is switched from  $30\ \Omega$  to  $10\ \Omega$ .  $k$  is 0.1739.

ratio control, the minimum input current P&O control is executed right after  $t_1$ . It takes more than 10 seconds to search for the minimum input current. As shown in Fig. 4.12(b), the voltage ratio  $\frac{V_2}{V_1}$  can be kept between 0.8 and 1.2, which are within the range of maximum efficiency as indicated in Fig. 4.7. At  $t_2$ , the output power increases three times by switching the load resistance from  $30 \Omega$  to  $10 \Omega$ . The SSIPT converter is a transconductance converter and the load-side converter is a current-driven converter. The output current  $I_2$  of the SSIPT converter is proportional to  $V_1$ . Due to the slow regulation of  $V_1$  by the P&O control,  $I_2$  cannot keep up with the sudden large increment of the output power. However, the control loop of the load-side converter is fast. Therefore, the voltage input  $V_2$  of the current-driven load-side converter rises rapidly trying to acquire more power. As shown in Fig. 4.12(b),  $V_2$  becomes saturated because of over voltage, leading to the output voltage being out of control. By comparing Fig. 4.12(a) and Fig. 4.12(b), the voltage error control has better robustness against load-variation due to its faster regulation speed.

#### 4.4.5 Discussion

Table 4.3:  $k$ -independent Converter Transfer Function at Maximum Efficiency

Topology	Converter at maximum efficiency
SS	$\frac{v_o}{v_i} = \sqrt{\frac{R_S}{R_P}}$
PS	$\frac{v_o}{i_i} = \omega L_S \sqrt{\frac{R_S}{R_P}}$

For an IPT converter with a  $k$ -independent input-to-output transfer function and maximum efficiency, the linear control method proposed in this chapter can be used. Two example converters are shown in Table. 4.3. For IPT converters having  $k$ -dependent input-to-output transfer functions and maximum efficiency, before applying this linear control method, the  $k$ -dependent characteristic should be removed by some means, such as using a self-oscillating control as proposed

in [195]. Design parameters of the IPT converters are usually known during the design phase. Equivalent series resistances  $R_P$  and  $R_S$  can be estimated from device parameters. The approximated voltage ratio  $\frac{V_2}{V_1}$  can be calculated using (4.3) as a control reference. Moreover, if the parameters are not available during the design phase or whenever verification is necessary, they can be measured experimentally as illustrated in Fig. 4.7. Alternatively, automatic in-circuit measuring methods, such as the P&O method, can also be implemented to determine the voltage ratio  $\frac{V_2}{V_1}$  at maximum efficiency dynamically at the expense of using more sensors. The voltage ratio  $\frac{V_2}{V_1}$  determined can be stored as a control reference for the linear control method proposed in this chapter to improve performance.

## 4.5 Summary

To achieve maximum efficiency of an inductive power transfer (IPT) system, it is common to use nonlinear perturbation and observation (P&O) control for an IPT system consisting of an IPT converter cascaded with front-side and load-side dc/dc converters. The P&O control is inevitably slow. A linear control scheme is proposed to achieve fast maximum efficiency tracking for an inductive power transfer system in this chapter. By observing that the maximum efficiency occurs at a specific input-to-output voltage transfer ratio, a small-signal model for the IPT converter and the front-side converter operating as a combined transconductance converter is developed in this chapter. To be compatible with the current output of the transconductance converter, the load-side converter is designed with a stand-alone trans-resistance converter. The controllers for the system are analyzed and experimentally verified to be fast and effective in this chapter.



## Chapter 5

# Stability Criteria for SSIPT Power Distribution System

In previous chapters, we have discussed that the SSIPT converter can provide a constant output current which is independent of load variations when operating at its power efficient point [136,158]. The SSIPT converter cascaded with a single load-side converter for output power regulation is studied in Chapter 4. In this chapter, we will generalize the current-source system where the SSIPT converter is cascaded with multiple load-side converters.

Wireless power transfer systems are often designed with an inductive power transfer (IPT) converter cascaded with a downstream pulse-width modulation (PWM) converter to achieve a high overall system efficiency under line or load variation [150, 160, 163, 187, 196]. As an example, a three-stage IPT system is studied in Chapter 4. In this chapter, we will go further into a current-source system where an SSIPT converter is cascaded with multiple load-side converters.

The series-series compensated IPT (SSIPT) converters [160, 163, 187, 196] are among the most power efficient IPT converters [136, 158]. In this current-source system, no voltage regulation is needed at the interface of the cascaded power converters. Therefore, an equivalent source converter of the system has high

output impedance which makes it difficult to meet the Middlebrook stability criterion applied to a voltage-source system that a stable cascaded converter should have its upstream power converter having a substantially lower output impedance compared to the input impedance of its downstream power converter [197–199]. However, the impedance-based stability criterion for current-source systems presented by [200, 201] is not general enough for applications with multiple loads, as shown in Fig. 5.1. In such a system, the converters can share either a common voltage bus or a common current loop. Additionally, as will be shown in Section 5.3, the definition of either a voltage-source system or a current-source system is still unclear for the configurations shown in Figs. 5.1(b) and (c), making direct application of the Middlebrook stability criterion and its dual rather difficult.

In this chapter, we analyze the general cascaded converter system by considering an equivalent model as seen by one of the DC/DC converters and apply power balance to gain insights into the difference between a voltage-source system and a current-source system. A general set of impedance based criteria of stability will be developed as a generalization of the criteria presented in [200, 201]. The set of stability criteria developed from this simple model will be verified experimentally by a cascaded SSIPT-PWM converter system. A stable prototype of independently controlled IPT and PWM converters will be demonstrated.

## 5.1 Impedance-based Stability Criterion

Impedance-based stability criterion [197] has been applied for the voltage source system consisting a voltage-source converter and a load converter connected in cascade, with a regulated voltage being the interface between the source and load converters. Based on a small-signal model, the Middlebrook stability criterion states that the system is stable if the following conditions are satisfied

- V1 the source converter having an output voltage  $V_o$  and output impedance  $Z_s$  is stable without being loaded,
- V2 the load converter having an input impedance  $Z_l$  is stable when connected to an ideal voltage source  $V_o$ , and
- V3(a) aggressively,  $T_v = Z_s/Z_l$  satisfies the Nyquist stability criterion, or
- V3(b) conservatively,  $|T_v| \ll 1$

Cascaded-converter systems with an inverter of high impedance current source output connected to the low impedance input of a grid voltage have been studied by Sun [200] who identified the systems as current source systems and presented a stability criterion as a dual to that given in [197]. Specifically, this current source system is stable if the following conditions are satisfied:

- C1 the source converter having an output current  $I_o$  and impedance  $Z_p$  is stable without being loaded,
- C2 the load converter having an input impedance  $Z_l$  is stable when connected to an ideal current source  $I_o$ , and
- C3(a) aggressively,  $T_c = Z_l/Z_p$  satisfies the Nyquist stability criterion, or
- C3(b) conservatively,  $|T_c| \ll 1$

The above stability criteria have been applied to dc power distribution systems with multiple sources and loads where the numbers of sources and loads are changing dynamically [201]. Apart from verifying condition V1 or V2 as appropriate for each converter, the system's minor loop gain  $T_v$  (referred to in V3) has been extended to include every impedance (or admittance) of the system

given by

$$T_v = \frac{\text{parallel of all } m \text{ source impedances}}{\text{parallel of all } n \text{ load impedances}} \quad (5.1)$$

$$= \frac{\sum_{j=1}^n \frac{1}{Z_{lj}}}{\sum_{j=1}^m \frac{1}{Z_{sj}}}. \quad (5.2)$$

Likewise, similar modification has been proposed for the current-source system. However, only the usual voltage source systems are studied in detail [201] due to the fact that such voltage source systems, having a dominating bus voltage regulator, are the only systems considered in most DC power distribution systems.

## 5.2 Steady-state Operation Points from Viewpoint of Power Balance

To differentiate a voltage-source system from a current-source system, we can consider the DC steady-state model of the system by referring to Fig. 5.1 with all small-signal variables being replaced by their DC counterparts. For brevity, we can start with  $n = 1$ , where Fig. 5.1(a) becomes identical to Fig. 5.1(c) and Fig. 5.1(b) becomes identical to Fig. 5.1(d). The DC operating circuit for  $n = 1$  is shown in Fig. 5.2, where the source and load share the same voltage bus  $V$  and current loop  $I$ .

Fig. 5.1 shows equivalent small-signal models of closed-loop converters. We assume that the converters are stable, operating safely within their voltage, current and power ratings, and can be perfectly controlled to their DC operating points with a finite bandwidth  $f_{BW}$ . In this sense, the voltage-source converter S1 has been stably biased to its DC operating point as an ideal voltage source  $V_o$  with a small source resistance  $R_S$ , which represents the resistance of interconnection as well as the intentional output resistance from control algorithms such as the

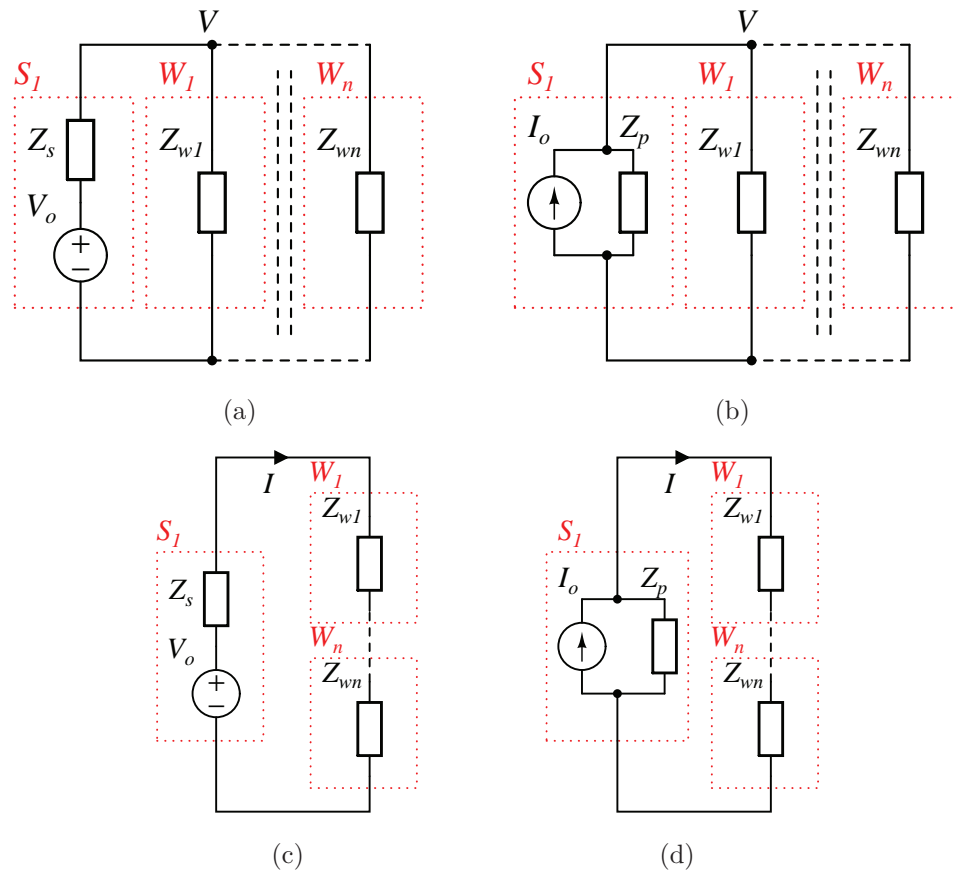


Figure 5.1: Impedance-based models of a source converter  $S_1$  and  $n$  load converters  $W_1, \dots, W_n$ . Components inside the dotted line blocks are the small-signal-equivalent circuit of the converters. (a) Voltage source converter  $S_1$  sharing a common voltage with  $n$  load converters. (b) Current source converter  $S_1$  sharing a common voltage with  $n$  load converters. (c) Voltage source converter  $S_1$  sharing a common current with  $n$  load converters. (d) Current source converter  $S_1$  sharing a common current with  $n$  load converters.

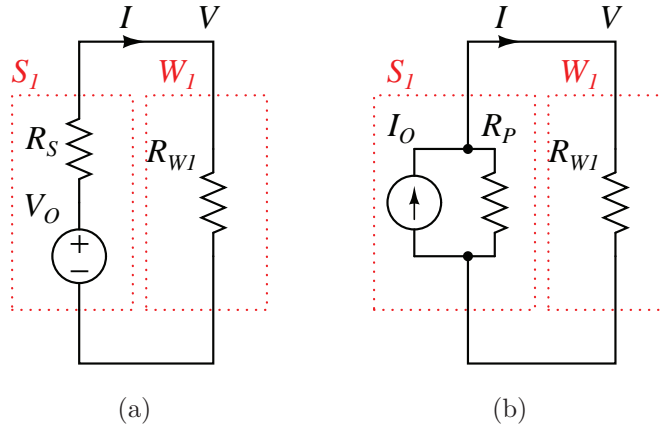


Figure 5.2: DC operation models of a source converter  $S_1$  and a load converter  $L_1$ . Components inside the dotted line blocks are the DC-equivalent circuit of the converters. (a) Voltage source converter  $S_1$  sharing a common voltage with a load converter. (b) Current source converter  $S_1$  sharing a common voltage with a load converter.

droop controller. The DC operating circuit shares the same circuit structure as shown in Fig. 5.1, with the corresponding DC variables being represented with uppercase letters and subscripts as appropriate. Likewise, we have an ideal DC current source  $I_o$  and its large parallel output resistance  $R_p$  for a current-source converter.

The  $n$ -load converters are normally regulated with a constant output voltage or current. When such near lossless converters are connected with resistive loads, their inputs will behave as a near perfect constant power sink  $P_{W_i} = V_{W_i} I_{W_i}$ , where  $i = 1, \dots, n$ . Obviously, the same  $P_{W_i}$  can be biased at different points on a constant power curve, such as points A, B or C, as shown in Fig. 5.3. It should be noted that point A has a DC resistance of  $R_A = \frac{V_A}{I_A}$  while its incremental resistance on the constant power curve is  $-R_A$ , which should equal  $Z_{w_i}$  within  $f_{BW}$ . Obviously, to meet the output power requirement of  $P_{W_i}$ , the load converter  $W_i$  can be biased anywhere on the power curve. The choice of biasing at a point on the power curve will be decided by the practical requirements of meeting the voltage and current ratings by designing a suitable  $R_{W_i}$  and the regulation bandwidth dictates the associated  $Z_{w_i}(f) = -R_{W_i}$  with  $f < f_{BW}$ .

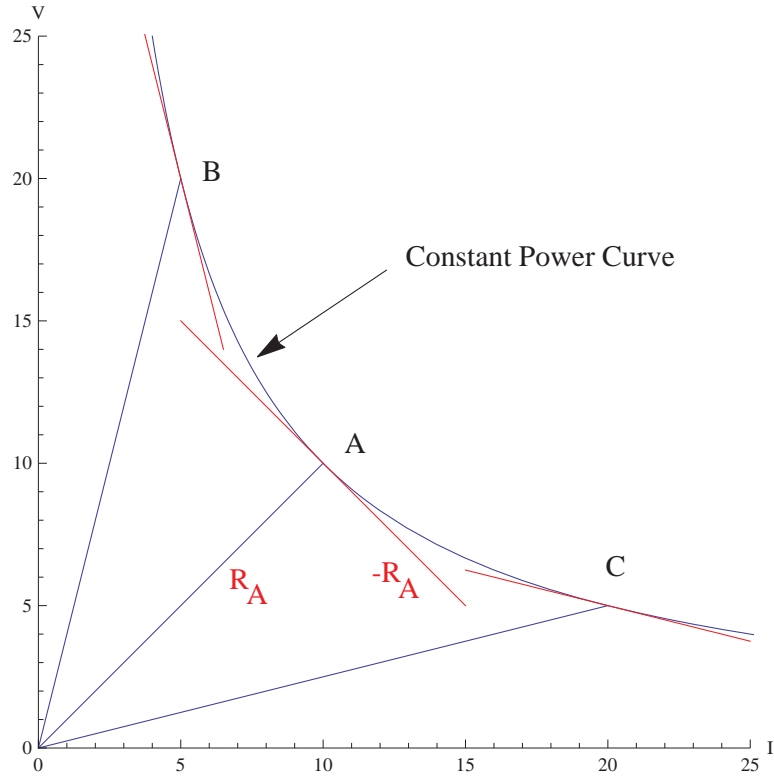


Figure 5.3: Constant power curve with biasing points A, B and C.

With reference to Fig. 5.2(a), the power output from  $S_1$  should be identical to the power input to  $W_1$ . The power  $P_I = P_{W_1}$  feeding to  $R_L = R_{W_1}$  can be plotted as shown in Fig. 5.4, which gives the expected maximum power transfer when  $R_L$  is equal to  $R_S$ . Moreover, an intended input power  $P_I$  can be biased at two loading resistances  $R_{Lx}$  and  $R_{Ly}$  such that  $R_{Lx} < R_S < R_{Ly}$ . For a native source resistance  $R_S$ , operating at  $R_{Ly}$  will be more efficient than that at  $R_{Lx}$ . However, if  $R_S$  is a virtual equivalent resistance as a result of application of some control algorithms which are common in some AC or DC voltage bus systems [202], there would not be much difference in efficiency between the operation points  $R_{Lx}$  and  $R_{Ly}$ . It can be observed that a small increment of  $R_L$  at  $R_{Lx}$  acquires a higher  $P_I$ , while a small increment of  $R_L$  at  $R_{Ly}$  corresponds to a lower  $P_I$ . This gives an intuitive explanation on the requirement that the load  $R_{Ly}$  is stable when it is connected to an ideal voltage source as the two systems give near identical  $\frac{\delta P_I}{\delta R_L}$ ,

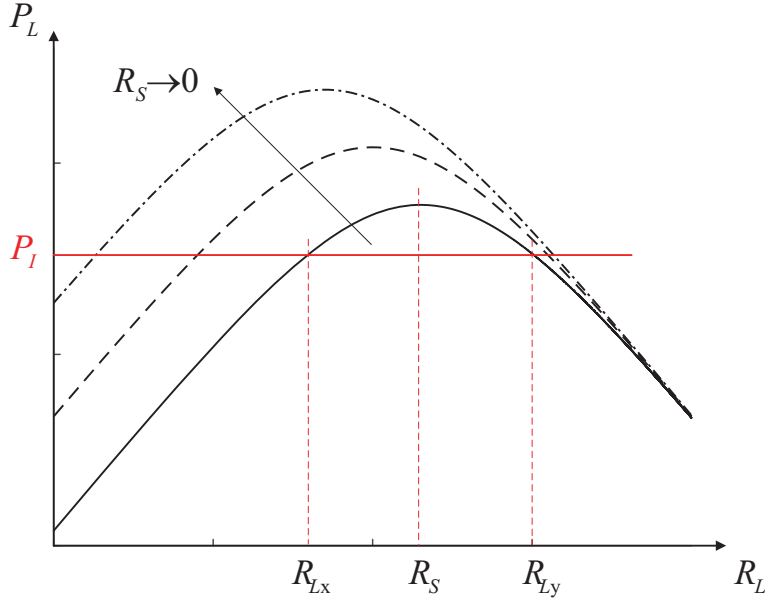


Figure 5.4: Power transfer characteristic of a voltage-source system.

especially when  $R_L \gg R_S$ . It can be observed in Fig. 5.4 that the load converter  $W_1$  operating with  $R_{Ly}$ , i.e.,  $R_L > R_S$ , will become unstable when it is operating near  $R_S$  and even worse for  $R_L \leq R_S$  as  $\frac{\delta P_l}{\delta R_L}$  will deviated significantly from that operating with  $R_{Ly}$  [203]. It is obvious that converter  $W_1$  switching operation points from  $R_{Ly}$  to  $R_{Lx}$  should have its feedback circuit redesigned.

Likewise, with reference to Fig. 5.2(b), a current-source system has a power transfer characteristic as shown in Fig. 5.5. It is similar to Fig. 5.4 except that the current-source system is normally operating at  $R_{Lx}$  while for a voltage-source system, it is normally operating at  $R_{Ly}$ . Based on our previous analysis on voltage-source systems, we can arrive at a corresponding set of results using the *Duality Principle*. Specifically, for a voltage-source system,  $\frac{\delta P_l}{\delta R_L}$  at  $R_{Lx}$  is proportional to  $R_{Lx}$ , while for a current source system  $\frac{\delta P_l}{\delta R_L}$  at  $R_{Ly}$  it is inversely proportional to  $R_{Ly}$ . This gives an intuitive explanation for the requirement that the load  $R_{Lx}$  is stable when it is connected to an ideal current source as the two systems give near identical  $\frac{\delta P_l}{\delta R_L}$ , especially when  $R_L \ll R_P$ . Similarly, it can be observed from Fig. 5.5 that the load converter  $W_1$  operating at  $R_{Lx}$ , i.e.,

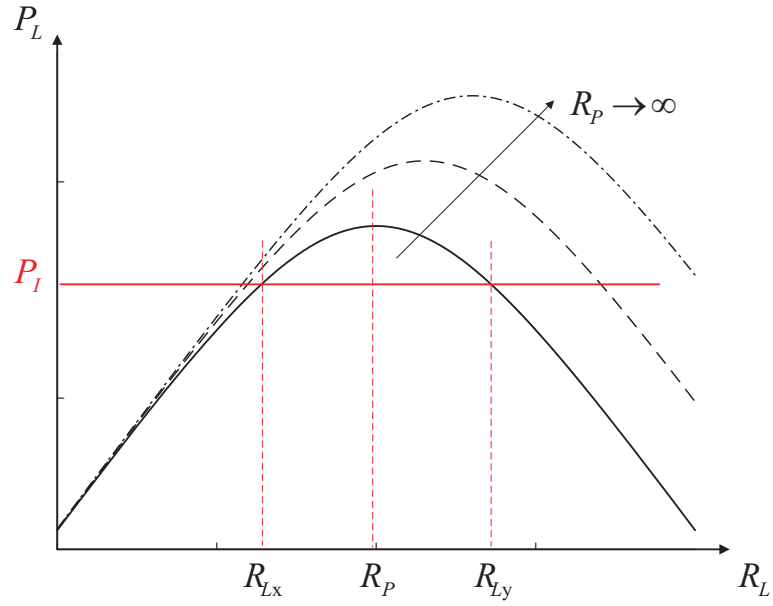


Figure 5.5: Power transfer characteristic of a current-source system.

$R_L < R_P$ , will become unstable when it is operating near  $R_P$  and even worse for  $R_L \geq R_P$ . It is also obvious that converter  $W_1$  switching operation points from  $R_{Lx}$  to  $R_{Ly}$  should have its feedback circuit redesigned.

It can be concluded from Figs. 5.4 and 5.5 that for the source converter having output resistance  $R_O$  and the load converter having input resistance  $R_L$ , the system is considered a voltage source system if  $R_L \gg R_O$ , otherwise it must have  $R_L \ll R_O$  and the system is a current source system. Meanwhile for  $f < f_{BW}$ ,  $R_L \gg R_O$  is equivalent to  $|Z_i(f)| \gg |Z_o(f)|$  and  $R_L \ll R_O$  is equivalent to  $|Z_i(f)| \ll |Z_o(f)|$  that these two conditions are subsets of the conservative conditions V3(b) of the Middlebrook stability criterion and C3(b) of the dual of the Middlebrook stability criterion.

### 5.3 Current or Voltage Driven Subsystems of Single Source Multiple Loads

In Section 5.2, the single-source single-load system is readily distinguished as being a voltage-source system or a current-system by considering the relative magnitude of the source and load resistances at DC operation. In Fig. 5.6, two loads  $W_1$  and  $W_2$  are assumed independently controlled, or otherwise, they can be combined into a single load such that the system is equivalent to a single-load system as shown in Figs. 5.2(a) or 5.2(b). To distinguish between a voltage-source system and a current-source system, we assess the converter subsystems individually. It can be readily observed from Fig. 5.6(a) that as long as

$$R_S \ll (R_{W1} || R_{W2}), \quad (5.3)$$

we have

$$(R_S || R_{W2}) \ll R_{W1}, \text{ and} \quad (5.4)$$

$$(R_S || R_{W1}) \ll R_{W2}. \quad (5.5)$$

For  $S_1$ , an equivalent resistance of  $R_L = (R_{W1} || R_{W2})$  is being driven. Equation (5.3) identifies a voltage-source system for  $S_1$ . Likewise, (5.4) and (5.5) identify a voltage-source system for  $W_1$  and  $W_2$ . They can be designed stable by following the Middlebrook stability criterion [197] for their individual equivalent circuits. Similar arguments apply to Fig. 5.6(d) with respect to a current-source system with  $R_P \gg (R_{W1} + R_{W2})$  and each load is designed to be stable when it is connected to an ideal current source. The results can be readily generalized to an  $n$ -load voltage-source system with  $R_S \ll R_{W1} || R_{W2} || \dots || R_{Wn}$  and an  $n$ -load current-source system with  $R_P \gg (R_{W1} + R_{W2} + \dots + R_{Wn})$ . Common properties

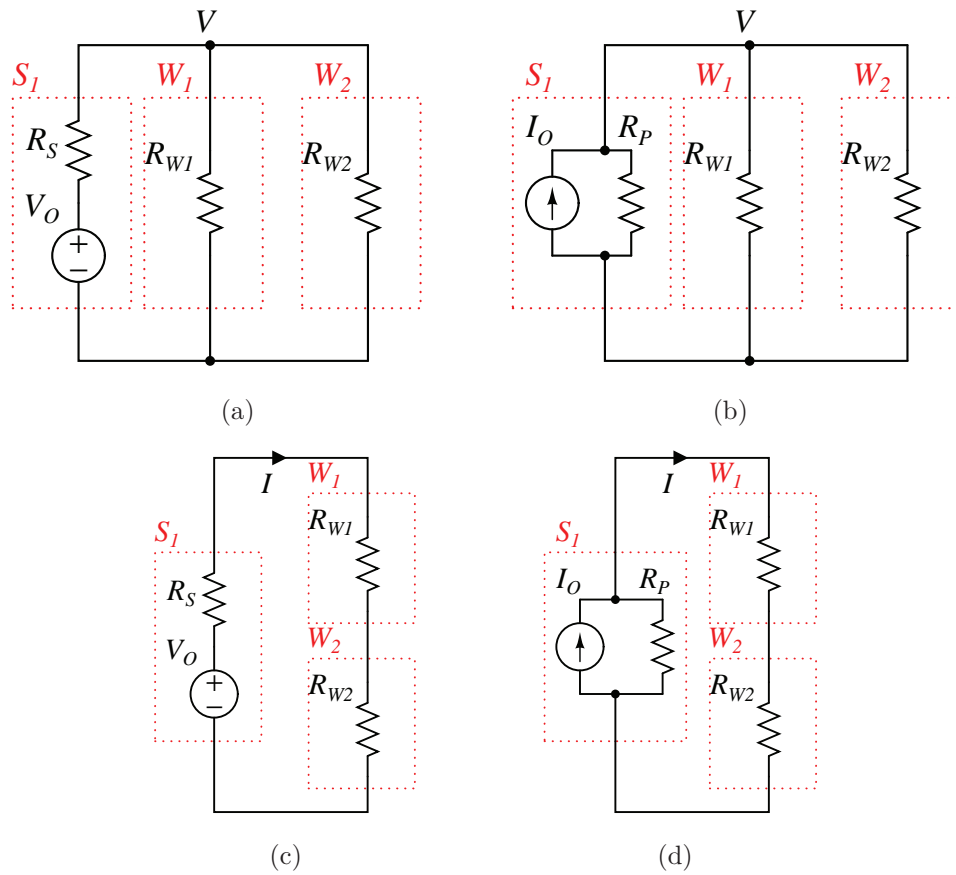


Figure 5.6: DC circuit models of four possible configurations consisting of a source converter  $S_1$  and two load converters  $W_1$  and  $W_2$ .

of systems represented by Fig. 5.6(a) and (d) are:

- there is a dominated source which regulates either the bus voltage or current of the system, and
- each load shares the *same* system defined by the source converter, i.e., a voltage or a current source system.

The stabilities of these well defined voltage-source or current-source systems can be easily assessed by applying either (V1) to (V3) or (C1) to (C3) to each of the source or load converters, or simply (5.2) or its dual [201].

The systems shown in Figs. 5.6(c) and (d) are less attractive than those shown in Figs. 5.6(a) and (b) which share a common voltage bus for easy connection or

disconnection of loads. The identification and possible modification of the voltage or current source system shown in Fig. 5.6(b) will be developed as follows. For the current-driven system shown in Fig. 5.6(b), by applying Middlebrook stability criterion [197, 200] to each of the subsystem, the source  $S_1$  is stable if (C1) and the conservative condition (C3b) (we only need this condition to be satisfied for  $f < f_{BW}$ ) are satisfied, which is equivalent to

$$R_P \gg (R_{W1} || R_{W2}), \quad (5.6)$$

the load  $W_1$  should assume being driven by a current source. If so, we have

$$(R_P || R_{W2}) \gg R_{W1} \quad (5.7)$$

and the load  $W_2$  should assume being driven by a current source. If so, we have

$$(R_P || R_{W1}) \gg R_{W2}. \quad (5.8)$$

It can be observed from Fig. 5.5 that (5.7) and (5.8) cannot be satisfied simultaneously if  $R_{W1}$  and  $R_{W2}$  are of similar order of magnitude and both  $W_1$  and  $W_2$  are stable when they are connected to an ideal current source. Without loss of generality, let us assume

$$R_{W1} \ll R_{W2} \quad (5.9)$$

such that (5.7) is satisfied, i.e., subsystem  $W_1$  is stable if it is stable when connected to an ideal current source. Now, for subsystem  $W_2$ , (5.8) can never be satisfied, i.e., subsystem  $W_2$  cannot be stable when it is designed to be driven by

a current source. Fortunately, from (5.9) we have

$$(R_P || R_{W1}) \ll R_{W2}, \quad (5.10)$$

which satisfies the stability criterion V2 of subsystem  $W_2$ , as given in Figs. 5.2(a) and 5.5, i.e., subsystem  $W_2$  can be stable if it is stable when it is connected to an ideal *voltage* source [197], where the parallel connection of the current source and resistance  $(R_P || R_{W1})$  are regarded as its Thevénin's voltage source equivalent. Since from the load's perspective, Thevénin's voltage source and Norton's current source are interchangeable, this result is important in several aspects:

1. From the perspective of  $W_1$ , it is driven by a *current-source* as shown in Fig. 5.5 with the source resistance  $(R_P || R_{W2})$ .
2. From the perspective of  $W_2$ , it is driven by a *voltage-source* as shown in Fig. 5.4 with the source resistance  $(R_P || R_{W1})$ .
3. The systems in Fig. 5.4 and Fig. 5.5 are equivalent in terms of the load stability criteria.
4. For the single-source-two-load system, the design of subsystem  $W_1$  which is assumed stable when it is connected to an ideal *current* source is different from that of  $W_2$  which is assumed stable when it is connected to an ideal *voltage* source.
5. For the stable single-source-two-load system, the power level of subsystem  $W_1$  will be much higher than that of subsystem  $W_2$  when they are controlled independently. To have the freedom of operating at any power level, the controls of the subsystems must be well coordinated. In such a case, they reduce to a single-load system.

In summary, the lowest (highest) resistance of the system in Fig. 5.6(b) (Fig. 5.6(c)) acquires most of the power from the current (voltage) source and converts the current (voltage) source into an equivalent voltage (current) source for driving the other load.

The identification of current or voltage driven load subsystems can be readily generalized to an  $n$ -parallel-load current-source system with the conditions that  $R_P \gg (R_{W1} || \dots || R_{Wn})$ ,  $(R_P || R_{W2} || \dots || R_{Wn}) \gg R_{W1}$  and  $(R_P || R_{W1}) \ll R_{W_i}$  for  $i = 2 \dots n$ , where  $W_1$  is stable when it is connected to an ideal current source, and  $W_i (i = 2 \dots n)$  is stable when connected to an ideal voltage source. Similarly, it can be generalized to an  $n$ -series-load voltage-source system with the conditions that  $R_S \ll (R_{W1} + \dots + R_{Wn})$ ,  $(R_S + R_{W2} + \dots + R_{Wn}) \ll R_{W1}$  and  $(R_S + R_{W1}) \gg R_{W_i}$  for  $i = 2 \dots n$ , where  $W_1$  is stable when it is connected to an ideal voltage source, and  $W_i (i = 2 \dots n)$  is stable when connected to an ideal current source.

The stability of each subsystem can be assessed by applying the source system identified. The system is stable when all subsystems satisfy the individually identified Middlebrook stability criterion or its dual.

## 5.4 Illustrative Example: Single-Current-Source Two-Load System

### 5.4.1 Inductive power transfer converter

In this section, the single-source-two-load system as shown in Fig. 5.6(b) is selected for design and verification. As shown in the block diagram of Fig. 5.7, an IPT converter will be selected as  $S_1$  which can operate with its most efficient configuration and has a current output. Two independently controlled DC/DC PWM converters  $W_1$  and  $W_2$  will be designed as load converters of the system.

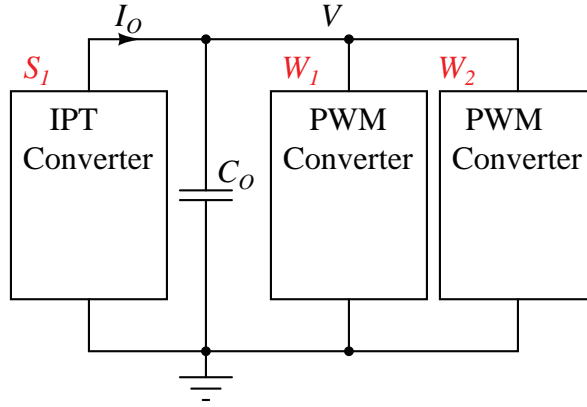


Figure 5.7: Block diagram of the single-current-source-two-load system.

The source converter  $S_1$  and load converters  $W_1$  and  $W_2$  have internal DC operation models shown in Fig. 5.6(b).  $S_1$  has an equivalent resistance  $R_P$  which takes into account the losses due to the IPT transformer windings, magnetic cores and electronic devices. Such an IPT converter normally has a switching frequency current ripple filtering capacitor  $C_O$  which may pose constraints on the design of load converters  $W_1$  and  $W_2$ . Using the extra stability conditions developed in Section 5.3, subsystem  $W_1$  should be designed stable when it is connected with a current-source input, while subsystem  $W_2$  should be designed stable when it is connected with a voltage-source input. Hence, a stable system has  $R_{W1} \ll (R_P \parallel R_{W2})$  and  $R_{W2} \gg (R_P \parallel R_{W1})$ . Moreover, to be qualified as a current source converter,  $R_P \gg (R_{W1} \parallel R_{W2})$ .

Existing PWM converters as shown in Fig. 5.8 are mostly designed with a voltage-source input. The current-source-input converter can be derived from the basic voltage-source converter based on duality principle [204], as shown in Fig. 5.9. However, converters in Figs. 5.9(a) and (c) are not compatible with the filtering capacitor  $C_O$  without appropriate modification. In this example, a higher power dual-boost converter and a lower power buck converter will be chosen as the two parallel load converters  $W_1$  and  $W_2$  respectively.

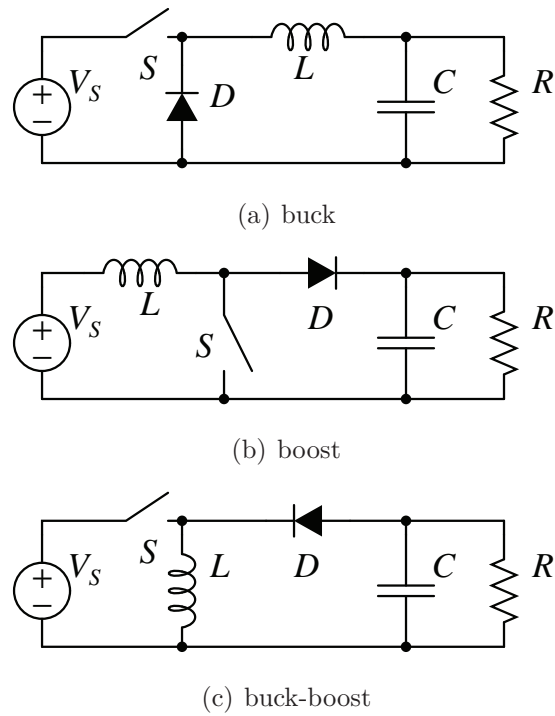


Figure 5.8: Basic PWM voltage converters.

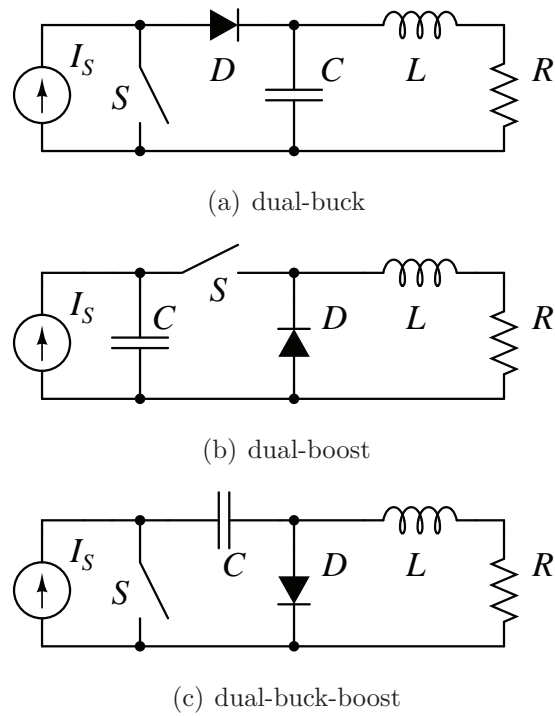
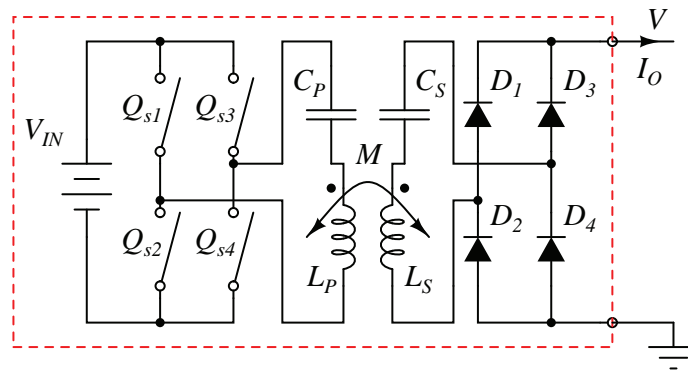
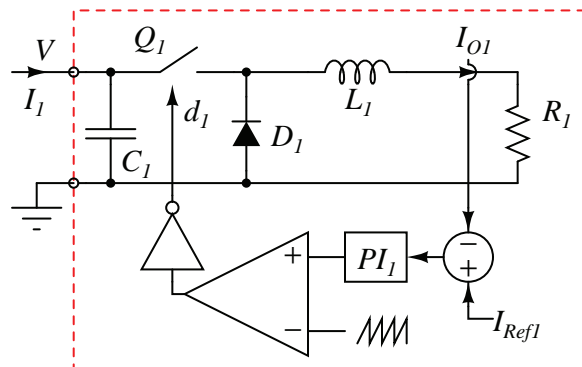


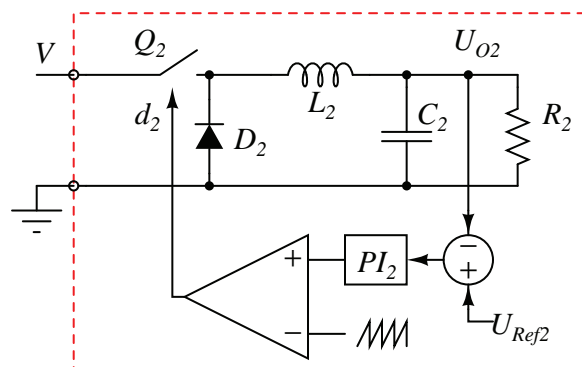
Figure 5.9: Basic PWM current converters.



(a) IPT converter  $S_1$



(b) dual-boost converter  $W_1$



(c) buck converter  $W_2$

Figure 5.10: Schematic of the single-current-source-two-load subsystems.

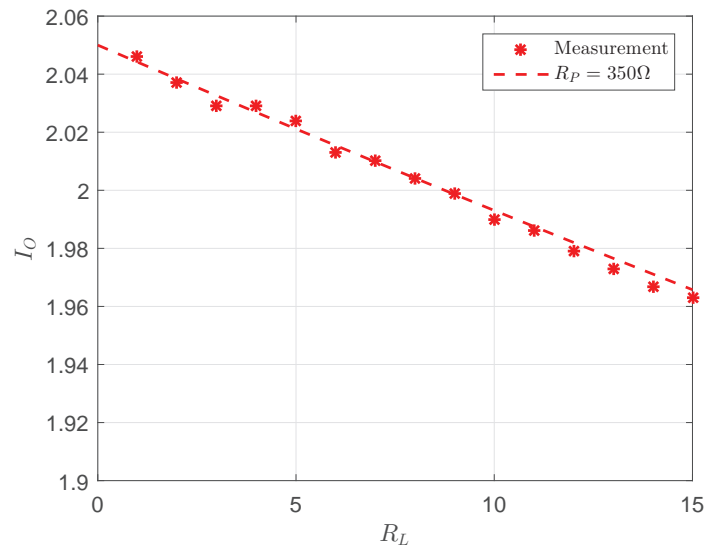
Table 5.1: Parameters of Converters

Parameters	Symbol	Value
Primary self inductance	$L_P$	31.46 $\mu\text{H}$
Secondary self inductance	$L_S$	33.02 $\mu\text{H}$
Mutual inductance	$M$	9.32 $\mu\text{H}$
Coupling coefficient	$k$	0.289
Primary compensation capacitor	$C_P$	19.73 nF
Secondary compensation capacitor	$C_S$	18.8 nF
Switching frequency	$f_S$	202 kHz
Inductance	$L_1$	2 mH
Capacitance	$C_1$	470 $\mu\text{H}$
Proportion Constant	$K_{p1}$	0.04
Integration Constant	$K_{i1}$	0.01
Inductance	$L_2$	2 mH
Capacitance	$C_2$	470 $\mu\text{H}$
Proportion Constant	$K_{p2}$	0.04
Integration Constant	$K_{i2}$	0.01

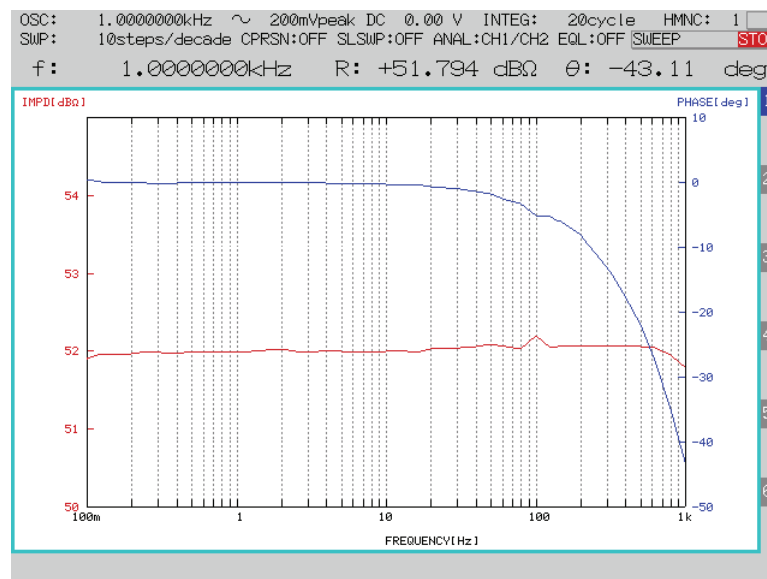
### 5.4.2 Experimental Evaluation

Fig. 5.10 shows the detailed schematics of subsystems  $S_1$ ,  $W_1$  and  $W_2$  of the system shown in Fig. 5.7 with parameters given in Table 5.1. The input voltage of  $S_1$  is  $V_{\text{IN}} = 30$  V. Since the SSIPT converter operates at resonant frequency  $f_S$ , the output current is load-independent [136,160,163,187,196]. The equivalent DC output current of the IPT converter can be estimated as  $I_O = \frac{8}{\pi^2} V_{\text{IN}} \frac{1}{2\pi f_S M} = 2.05$  A.

In this system,  $W_1$  regulates an output current of  $I_{O1} = 3$  A, driving a load  $R_1 = 3.75 \Omega$  at a power of 33.75 W. Also,  $W_2$  regulates an output voltage  $U_{O2} = 15$  V, driving a load  $R_2 = 35 \Omega$  at a power of 6.43 W. Using the viewpoint of power balance and ignoring the power loss of the converters, the bus voltage is estimated using  $VI_O = (33.75 + 6.43)$  W as  $V = 19.6$  V. The DC input equivalent resistances of the converters on the voltage bus  $V$  are  $R_{W1} = 11.4 \Omega$  (21.1 dB $\Omega$ ) and  $R_{W2} = 59.8 \Omega$  (35.5 dB $\Omega$ ). These resistances should guarantee  $R_{W1} \ll (R_P \parallel R_{W2})$  and  $R_{W2} \gg (R_P \parallel R_{W1})$ . The converters are built and their impedances are measured to be shown in the following subsections.



(a)



(b)

Figure 5.11: Output characteristics of  $S_1$ . (a) Steady-state output current  $I_O$  versus load resistance  $R_L$ . (b) Small signal response of output impedance.

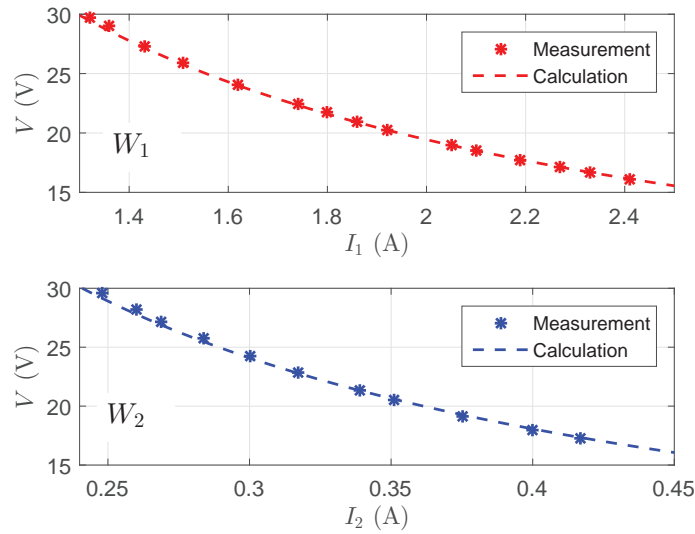


Figure 5.12: Measured input VI steady-state characteristics of PWM converters  $W_1$  and  $W_2$ . The dotted constant power curves fit well with the input powers 33.75 W of  $W_1$  and 6.43 W of  $W_2$ .

### 5.4.3 Output Resistance of the SSIPT Converter

Fig. 5.11(a) shows measured steady-state output current  $I_S$  versus load resistance  $R_L$  of  $S_1$ . The low-frequency output transfer function can be represented by a Norton equivalent circuit with a parallel connection of current  $I_O = 2.05$  A and resistance  $R_P = 350 \Omega$ . Fig. 5.11(b) shows the small signal output impedance of  $S_1$ . With a bandwidth from 0 Hz to 1 kHz,  $S_1$  should be stable driving an impedance lower than, say 50 dB $\Omega$ .

### 5.4.4 Input Resistance of Load Converters

Bus voltage versus input current of the two PWM converters are measured as data points ‘\*’ as shown in Fig. 5.12. The dotted lines are constant power curves of the converters. Small signal impedances of the converters are also measured as shown in Fig. 5.13, where  $W_1$  should be stable when it is driven by an idea current source with infinite impedance and  $W_2$  should be stable when it is driven by an idea voltage source with zero output impedance.

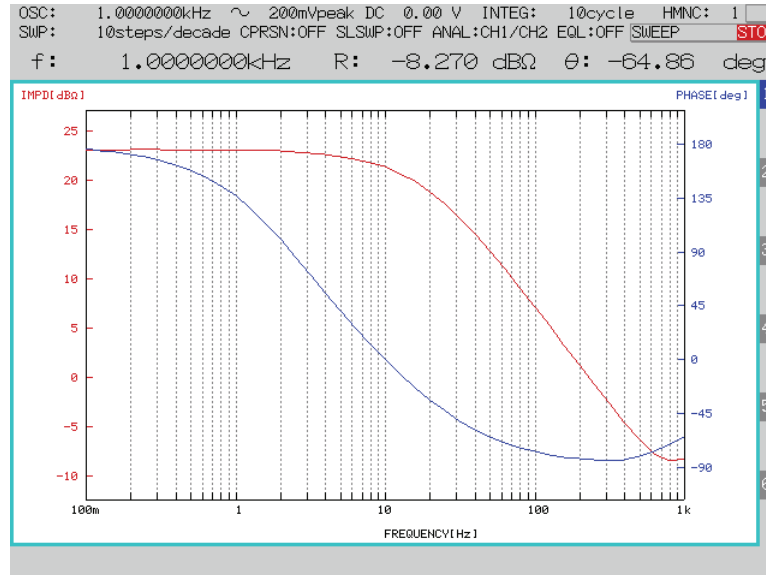
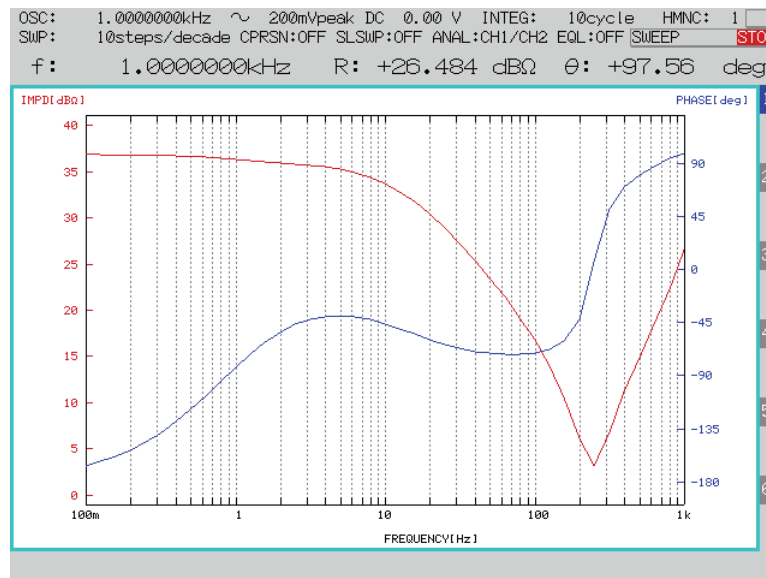
(a) dual boost converter  $W_1$ (b) buck converter  $W_2$ 

Figure 5.13: Measured input impedances of PWM converters.

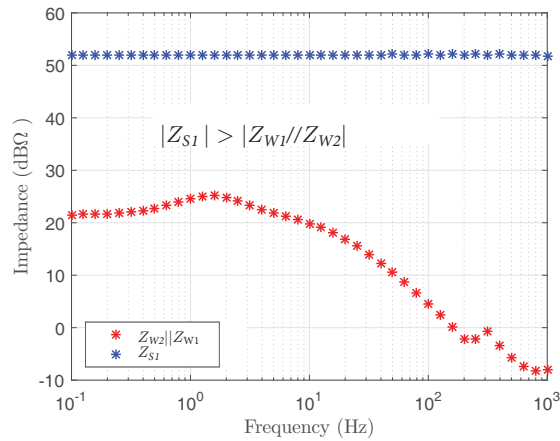
### 5.4.5 Stability Verification of the Single-Current-Source-Two-Load System

From the measurements taken in Section 5.4.4, small-signal responses of the three converters are compared based on the perspectives of each converter for the indication of local stability. Fig. 5.14 indicates that they are all locally stable within the measured bandwidth from 0 Hz to 1 kHz. To verify the system stability in general, step transient responses are performed.

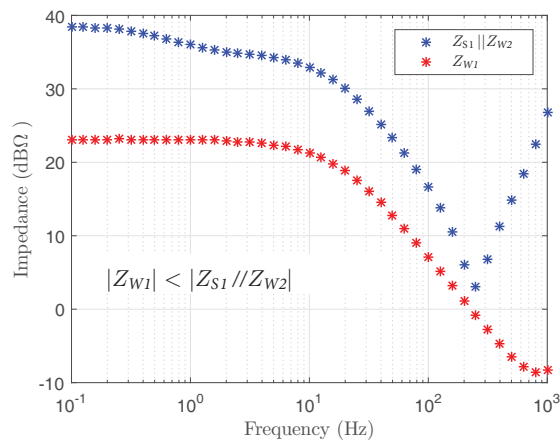
The control of the subsystems are tested by maintaining power balance at steady state. Firstly, the control of  $W_2$  is disabled by fixing  $D_2$ , such that it behaves as a resistor of  $R_{L2} = \frac{R_2}{D_2^2}$ .  $W_1$  is tested for its stability under closed-loop control. Fig. 5.15(a) shows the step response to a sudden reduction of the output reference current  $I_{\text{Ref}1}$  of  $W_1$ . It shows that  $R_{L1}$  decreases with decreasing output power, which coincides with the slope of the operating point  $R_{L1}$  in Fig. 5.5 and verifies the effectiveness of the control shown in Fig. 5.10.

A similar experiment is done to test the stability of the control for  $W_2$ . The duty cycle of  $W_1$  is disabled by fixing  $D_1$ , such that it behaves as a resistor of  $R_{W1} = \frac{R_1}{D_1^2}$ .  $W_2$  is tested for its stability under closed-loop control. Fig. 5.15(b) shows the step response to a sudden reduction of the output voltage reference  $U_{\text{Ref}2}$  of  $W_2$ . It shows that  $R_{W2}$  increases with decreasing output power, which coincides with the slope of the operating point  $R_{Ly}$  shown in Fig. 5.5 and verifies the effectiveness of the control shown in Fig. 5.10.

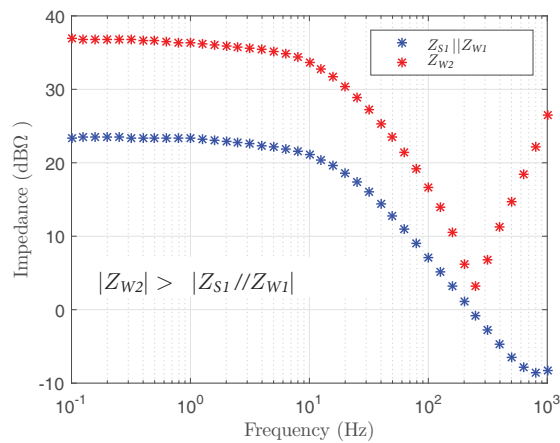
Finally,  $W_1$  and  $W_2$  are controlled independently. Fig. 5.16 shows the system in response to the cold start of  $W_2$ . It shows that the single-current-source-two-load system is stable, when the design is based on the generalized stability criteria developed in this chapter.



(a) SSIPT converter  $S_1$

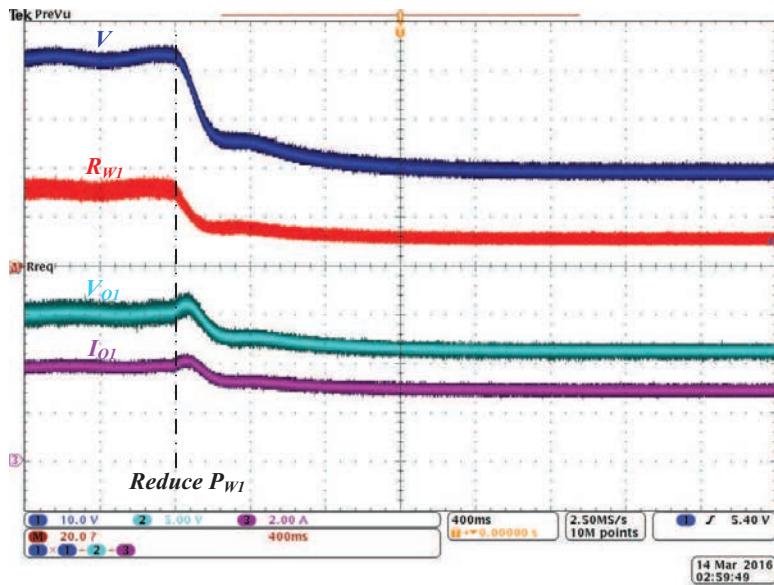


(b) dual boost converter  $W_1$

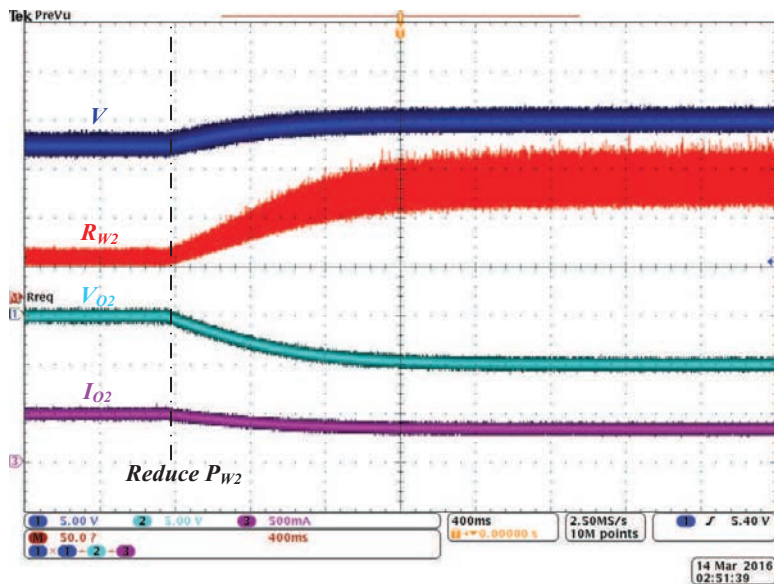


(c) buck converter  $W_2$

Figure 5.14: Measured magnitude of impedance ratio for object based stability verification of local stability within the bandwidth from 0 Hz to 1 kHz for converters (a)  $S_1$  using (C3a), (b)  $W_1$  using (C3a), and (c)  $W_2$  using (V3a).



(a)



(b)

Figure 5.15: Step response of the system. (a) Sudden reduction of the output reference current  $I_{Ref1}$  of  $W_1$  leading to a reduction of input voltage  $V$ , a characteristic of a current source system. Traces  $U_{O1}$  and  $I_{O1}$  are the output voltage and current of  $W_1$ . Trace  $R_{W1}$ , input resistance of  $W_1$ , is calculated based on measured data, using  $R_{W1} = \frac{V^2}{U_{O1}I_{O1}}$ , where the loss of the converter is ignored. (b) Sudden reduction of the output voltage reference  $U_{Ref2}$  of  $W_2$ , leading to an increment of  $V$ , a characteristic of a voltage source system. Traces  $U_{O2}$  and  $I_{O2}$  are output voltage and current of  $W_2$ . Trace  $R_{W2}$  is the input equivalent resistance of  $W_2$ , calculated using  $R_{W2} = \frac{V^2}{U_{O2}I_{O2}}$ , where the loss of the converter is ignored.

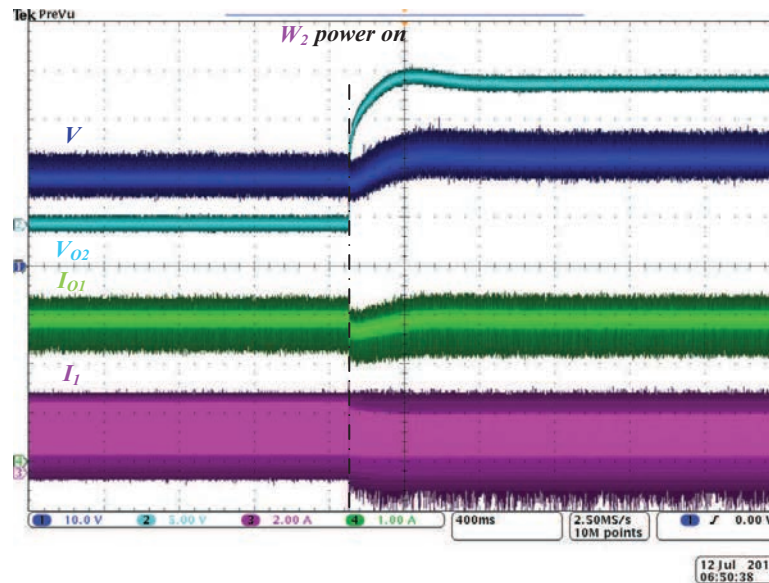


Figure 5.16: System in response to the cold start of  $W_2$ . Traces  $I_1$  and  $I_{O1}$  are the input and output currents of  $W_1$ . Traces  $V$  and  $U_{O2}$  are the input and output voltages of  $W_2$ .

## 5.5 Summary

Impedance-based stability criteria for cascaded systems of converters is revisited in this chapter. A more general set of criteria is presented here, which is suitable for the design of systems consisting of a single source cascaded with multiple load converters. This set of impedance-based stability criteria can be conveniently applied to a current output converter cascaded with multiple independently controlled current and voltage converters, such as those used in inductive power transfer systems.



# Chapter 6

## Conclusions and Suggestions for Future Research

This chapter summarizes the contributions which have been achieved in this project. Also, some suggestions and potential areas of investigation will be given for future research extension.

### 6.1 General Conclusions

A basic research of inductive power transfer (IPT) system was undertaken in this thesis. It includes design of single-stage IPT converter for EV battery charging, efficiency control of a three-stage IPT system and stability of an IPT power distribution power system.

Fundamentals of WPT are introduced in Chapter 1 of this thesis. Three kinds of mechanisms of wireless power transfer have been reviewed, including electromagnetic radiation, capacitive power transfer and inductive power transfer. Due to the advantages of IPT, it has found applications in static and dynamic power supply, including consumer electronics, biomedical implants, electric vehicles and many others. Literature review is given to study recent advances in

IPT systems in the aspects of coupler design, compensation network, control and safety.

Four basic compensation topologies (i.e., SS, SP, PS and PP) are first reviewed and evaluated in Chapter 2, based on conditions to achieve maximum efficiency and load-independent output. We combine maximum efficiency and load-independent output for the design and selection of the IPT converters. For secondary series compensation topologies (i.e., SS and PS), the choice of the operating frequency and the design of compensation network is independent of coupling coefficient  $k$ , which are suitable for dynamic applications.

In Chapter 3, implementation cases of single-stage IPT converter for EV battery charging are first studied. Operating at its native LIC and LIV points, SSIPT converter requires minimal modulation for CC and CV output. By designing  $\mu = \frac{\omega_P}{\omega_S} < 1$ , soft switching is facilitated during CC. And the overall efficiency for charging profile is optimized by determining a nominal quality factor  $Q_n$ . Experiment results evaluate the design of efficient single-stage IPT converter for EV battery charging.

In Chapter 4, a common three-stage IPT system is used for output power regulation and maximum efficiency tracking. By observing that the maximum efficiency occurs at a specific input-to-output voltage transfer ratio, linear control scheme based on voltage ratio is proposed, which can have faster and more accurate response compared with nonlinear control scheme (i.e., P&O). A small-signal model of the IPT converter and the front-side converter operating as a combined transconductance converter is developed. The controllers for the system are analyzed and experimentally verified to be fast and effective in this chapter.

In Chapter 5, impedance-base stability criteria for voltage-source system and current-source system are first reviewed. A current-source system is introduced, where an SSIPT converter is operating at current-source output and two load-side converters are cascaded in parallel. A more general set of stability criterion

based on power balance is proposed to distinguish the load-side converters between voltage-driven and current-driven converter. Experiment results verify the stability of this system.

## 6.2 Contributions of This Thesis Work

The main contributions of this thesis work are as follows.

- By combining maximum efficiency and load-independent output, four basic IPT converters (i.e., SS, SP, PS and PP) are evaluated. Due to  $k$ -independent operating frequency to achieve load-independent output and maximum efficiency, secondary series-compensated IPT converters are more suitable in applications with variation of  $k$ .
- An efficient single-stage SSIPT converter is designed for EV battery charging, by utilizing LIC and LIV characteristics for CC and CV charging, respectively. The design is elaborated with soft switching and overall efficiency optimization for the whole charging profile.
- A three-stage IPT system is used to meet the requirements of output power regulation and maximum efficiency tracking. A linear control scheme based on observing the voltage ratio is proposed, which performs much better than conventional P&O control in applications with fast variations of coupling coefficient and loading condition.
- A more general set of criteria is proposed, which is suitable for the design of systems consisting of a single SSIPT converter, operating as a current source, and multiple load converters in parallel connection.

### 6.3 Suggestions for Future Work

The work conducted in this thesis has focused on characteristics of single IPT converter, efficiency control of IPT converter and stability of IPT systems. Various theoretical analyses, system and component level simulations, and experimental verifications have been undertaken to achieve the research objectives. Useful results have been presented for static and dynamic applications. Further, more areas have also been opened for investigation in the future. To conclude this thesis, several areas are suggested here for future research on the topic.

#### **Frequency Control with Magnetic Shielding**

The efficiency of the IPT converter depends on the coupling coefficient of the loosely-coupled transformer. Therefore, it is common to use magnetic core to guide the magnetic flux, which can help improving the coupling coefficient. However, with magnetic core, the variation of the air gap distance will affect the self inductances of the coils in the primary and the secondary significantly. Therefore, the operating frequency should be dynamically adjusted by some control methods to satisfy the output requirement of the IPT converter.

#### **Control Design for Optimizing Efficiency for General IPT Converters**

In chapter 4, control design for optimizing efficiency for SSIPT converter has been studied. For more general IPT converters, such as SP, PS, PP and high order compensated converters, the output characteristics of maximum efficiency should be further studied. Unlike SSIPT converter, of which the operating frequency is  $k$ -independent, frequency control should also be studied to achieve maximum efficiency for most IPT converters.

### **Output Impedance and Compensation Network**

It is common to cascade load-side converters to the IPT converters, which requires the IPT converters to act as a current source or a voltage source. Otherwise, it is hard to control the load-side converters cascading to an uncertain source. It has been shown in Chapter 5, SSIPT converter has high output impedance when operating at  $\omega = \omega_P = \omega_S$ . It is also studied in Chapter 3 that the efficiency of SSIPT converter can be improved by designing  $\omega_P < \omega_S$ . However, such design of the compensation network will affect the output impedance of SSIPT converter, may lead to stability problems when cascading load-side converter. Therefore, to ensure the stability of the IPT systems, we should further investigate the relation between output impedance and compensation network design.

### **Compensation and Control for IPT converters with Multiple Receivers**

It has been studied in [120] that bipolar pad (BBP) matches the performance of double-D quadrature pad (DDQP) as a secondary pad, but with the advantage of using less copper. It has also shown in [5,121] that the design and control of BBP type IPT converter are more complicated. Studies of compensation network for BBP are still missing. Characteristics of BBP type IPT converters should first studied and compared under different design of compensation network. Output control and efficiency control can be further studied for practical applications.



# Bibliography

- [1] M. A. Rothstein and M. R. Anderlik, “The AbioCor artificial replacement heart: Bioengineering meets bioethics,” *Journal of Cardiothoracic and Vascular Anesthesia*, vol. 16, no. 2, pp. 234–239, 2002.
- [2] “30 kW inductive charging with CHAdeMO,” <https://www.chademo.com/30kw-inductive-charging-with-chademo/>.
- [3] J. M. Miller, P. T. Jones, J. M. Li, and O. C. Onar, “ORNL experience and challenges facing dynamic wireless power charging of EV’s,” *IEEE Circuits and Systems Magazine*, vol. 15, no. 2, pp. 40–53, Secondquarter 2015.
- [4] S. Li and C. C. Mi, “Wireless power transfer for electric vehicle applications,” *IEEE Journal of Emerging and Selected Topics in Power Electronics*, vol. 3, no. 1, pp. 4–17, Mar. 2015.
- [5] A. Zaheer, H. Hao, G. A. Covic, and D. Kacprzak, “Investigation of multiple decoupled coil primary pad topologies in lumped IPT systems for interoperable electric vehicle charging,” *IEEE Transactions on Power Electronics*, vol. 30, no. 4, pp. 1937–1955, Apr. 2015.
- [6] “Charging lithium-ion,” [http://batteryuniversity.com/learn/article/charging\\_lithium\\_ion\\_batteries](http://batteryuniversity.com/learn/article/charging_lithium_ion_batteries).

- [7] H. W. Secor, “Tesla apparatus and experimentshow to build both large and small tesla and oudin coils and how to carry on spectacular experiments with them,” *Practical Electrics*, Nov. 1921.
- [8] N. Tesla, “Apparatus for transmitting electrical energy,” U.S. Patent 1, 119, 732, 1914.
- [9] C. F. Andren, M. A. Fadali, V. L. Gott, and S. R. Topaz, “The skin tunnel transformer: A new system that permits both high efficiency transfer of power and telemetry of data through the intact skin,” *IEEE Transactions on Biomedical Engineering*, vol. BME-15, no. 4, pp. 278–280, Oct. 1968.
- [10] “Annual edition 1969 American aircraft modeler,” <http://www.airplanesandrockets.com/airplanes/model-airplanes-industry-annual-1969-aam.htm>.
- [11] J. C. Schuder, J. H. Gold, and H. E. Stephenson, “An inductively coupled rf system for the transmission of 1 kW of power through the skin,” *IEEE Transactions on Biomedical Engineering*, vol. BME-18, no. 4, pp. 265–273, Jul. 1971.
- [12] W. H. Ko, S. P. Liang, and C. D. F. Fung, “Design of radio-frequency powered coils for implant instruments,” *Medical and Biological Engineering and Computing*, vol. 15, no. 6, pp. 634–640, 1977.
- [13] A. Ghahary and B. H. Cho, “Design of a transcutaneous energy transmission system using a series resonant converter,” in *Proceedings of Annual IEEE Conference on Power Electronics Specialists*, 1990, pp. 1–8.
- [14] G. A. J. Elliott, J. T. Boys, and A. W. Green, “Magnetically coupled systems for power transfer to electric vehicles,” in *Proceedings of*

- International Conference on Power Electronics and Drive Systems (PEDS)*, Feb. 1995, pp. 797–801 vol.2.
- [15] J. O. McSpadden and J. C. Mankins, “Space solar power programs and microwave wireless power transmission technology,” *IEEE Microwave Magazine*, vol. 3, no. 4, pp. 46–57, Dec. 2002.
- [16] J. T. Boys, G. A. J. Elliott, and G. A. Covic, “An appropriate magnetic coupling co-efficient for the design and comparison of ICPT pickups,” *IEEE Transactions on Power Electronics*, vol. 22, no. 1, pp. 333–335, Jan. 2007.
- [17] B. Strassner and K. Chang, “Microwave power transmission: Historical milestones and system components,” *Proceedings of the IEEE*, vol. 101, no. 6, pp. 1379–1396, Jun. 2013.
- [18] J. C. Maxwell, “A dynamical theory of the electromagnetic field,” *Philosophical Transactions of the Royal Society of London*, vol. 155, pp. 459–512, 1865.
- [19] P. V. Nikitin, K. V. S. Rao, and S. Lazar, “An overview of near field UHF RFID,” in *Proceedings of IEEE International Conference on RFID*, Mar. 2007, pp. 167–174.
- [20] P. E. Glaser, “Power from the sun: Its future,” *Science*, vol. 162, no. 3856, pp. 857–861, 1968.
- [21] H. Matsumoto, “Research on solar power satellites and microwave power transmission in Japan,” *IEEE Microwave Magazine*, vol. 3, no. 4, pp. 36–45, Dec. 2002.
- [22] M. Mori, H. Kagawa, and Y. Saito, “Summary of studies on space solar power systems of Japan Aerospace Exploration Agency,” *Acta Astronautica*, vol. 59, no. 1, pp. 132–138, 2006.

- [23] S. Sasaki, K. Tanaka, and K. i. Maki, “Microwave power transmission technologies for solar power satellites,” *Proceedings of the IEEE*, vol. 101, no. 6, pp. 1438–1447, Jun. 2013.
- [24] N. Shinohara, Y. Kubo, and H. Tonomura, “Wireless charging for electric vehicle with microwaves,” in *Proceedings of International Electric Drives Production Conference (EDPC)*, Oct. 2013, pp. 1–4.
- [25] —, “Mid-distance wireless power transmission for electric truck via microwaves,” in *Proceedings of International Symposium on Electromagnetic Theory*, May 2013, pp. 841–843.
- [26] W. Zhou and K. Jin, “Efficiency evaluation of laser diode in different driving modes for wireless power transmission,” *IEEE Transactions on Power Electronics*, vol. 30, no. 11, pp. 6237–6244, Nov. 2015.
- [27] —, “Optimal photovoltaic array configuration under gaussian laser beam condition for wireless power transmission,” *IEEE Transactions on Power Electronics*, vol. 32, no. 5, pp. 3662–3672, May 2017.
- [28] B. C. Edwards and H. E. Bennett, “Space elevator feasibility test using laser power beaming,” in *Proceedings of High-Power Lasers and Applications*. International Society for Optics and Photonics, 2002, pp. 141–147.
- [29] D. E. Raible, “High intensity laser power beaming for wireless power transmission,” Master’s thesis, Cleveland State University, Cleveland, OH, USA, May 2008.
- [30] L. Xie, Y. Shi, Y. T. Hou, and A. Lou, “Wireless power transfer and applications to sensor networks,” *IEEE Wireless Communications*, vol. 20, no. 4, pp. 140–145, Aug. 2013.

- [31] C. Y. Xia, C. W. Li, and J. Zhang, "Analysis of power transfer characteristic of capacitive power transfer system and inductively coupled power transfer system," in *Proceedings of International Conference on Mechatronic Science, Electric Engineering and Computer (MEC)*, Aug. 2011, pp. 1281–1285.
- [32] A. Kumar, S. Pervaiz, C. K. Chang, S. Korhummel, Z. Popovic, and K. K. Afridi, "Investigation of power transfer density enhancement in large air-gap capacitive wireless power transfer systems," in *Proceedings of IEEE Wireless Power Transfer Conference (WPTC)*, May 2015, pp. 1–4.
- [33] International Commission on Non-Ionizing Radiation Protection, "ICNIRP guidelines for limiting exposure to time-varying electric and magnetic fields (1 Hz to 100 kHz)." *Health Physics*, vol. 99, pp. 818–836, 2010.
- [34] E. Culurciello and A. G. Andreou, "Capacitive inter-chip data and power transfer for 3-D VLSI," *IEEE Transactions on Circuits and Systems II: Express Briefs*, vol. 53, no. 12, pp. 1348–1352, Dec. 2006.
- [35] A. P. Hu, C. Liu, and H. L. Li, "A novel contactless battery charging system for soccer playing robot," in *Proceedings of International Conference on Mechatronics and Machine Vision in Practice*, Dec. 2008, pp. 646–650.
- [36] C. Liu, A. P. Hu, and N. K. C. Nair, "Coupling study of a rotary capacitive power transfer system," in *Proceedings of IEEE International Conference on Industrial Technology*, Feb. 2009, pp. 1–6.
- [37] H. Funato, H. Kobayashi, and T. Kitabayashi, "Analysis of transfer power of capacitive power transfer system," in *Proceedings of IEEE International Conference on Power Electronics and Drive Systems (PEDS)*, Apr. 2013, pp. 1015–1020.

- [38] D. Shmilovitz, A. Abramovitz, and I. Reichman, “Quasi-resonant LED driver with capacitive isolation and high PF,” *IEEE Journal of Emerging and Selected Topics in Power Electronics*, vol. 3, no. 3, pp. 633–641, Sep. 2015.
- [39] J. Kim and F. Bien, “Electric field coupling technique of wireless power transfer for electric vehicles,” in *Proceedings of IEEE TENCON Spring Conference*, Apr. 2013, pp. 267–271.
- [40] J. Dai and D. C. Ludois, “A survey of wireless power transfer and a critical comparison of inductive and capacitive coupling for small gap applications,” *IEEE Transactions on Power Electronics*, vol. 30, no. 11, pp. 6017–6029, Nov. 2015.
- [41] F. Lu, H. Zhang, H. Hofmann, and C. C. Mi, “An inductive and capacitive combined wireless power transfer system with LC-compensated topology,” *IEEE Transactions on Power Electronics*, vol. 31, no. 12, pp. 8471–8482, Dec. 2016.
- [42] A. Karalis, J. D. Joannopoulos, and M. Soljačić, “Efficient wireless non-radiative mid-range energy transfer,” *Annals of Physics*, vol. 323, no. 1, pp. 34–48, 2008.
- [43] T. Aoki, B. Dayan, E. Wilcut, W. P. Bowen, A. S. Parkins, T. J. Kippenberg, H. J. K. J. Vahala, and Kimble, “Observation of strong coupling between one atom and a monolithic microresonator,” *Nature*, vol. 443, no. 7112, pp. 671–674, 2006.
- [44] A. Kurs, A. Karalis, R. Moffatt, J. D. Joannopoulos, P. Fisher, and M. Soljačić, “Wireless power transfer via strongly coupled magnetic resonances,” *science*, vol. 317, no. 5834, pp. 83–86, 2007.

- [45] J. W. Kim, H. C. Son, D. H. Kim, K. H. Kim, and Y. J. Park, "Analysis of wireless energy transfer to multiple devices using CMT," in *Proceedings of Asia-Pacific Microwave Conference*, Dec. 2010, pp. 2149–2152.
- [46] N. Yin, G. Xu, Q. Yang, J. Zhao, X. Yang, J. Jin, W. Fu, and M. Sun, "Analysis of wireless energy transmission for implantable device based on coupled magnetic resonance," *IEEE Transactions on Magnetics*, vol. 48, no. 2, pp. 723–726, Feb. 2012.
- [47] B. L. Cannon, J. F. Hoburg, D. D. Stancil, and S. C. Goldstein, "Magnetic resonant coupling as a potential means for wireless power transfer to multiple small receivers," *IEEE Transactions on Power Electronics*, vol. 24, no. 7, pp. 1819–1825, Jul. 2009.
- [48] C. J. Chen, T. H. Chu, C. L. Lin, and Z. C. Jou, "A study of loosely coupled coils for wireless power transfer," *IEEE Transactions on Circuits and Systems II: Express Briefs*, vol. 57, no. 7, pp. 536–540, Jul. 2010.
- [49] M. Kiani and M. Ghovanloo, "The circuit theory behind coupled-mode magnetic resonance-based wireless power transmission," *IEEE Transactions on Circuits and Systems I: Regular Papers*, vol. 59, no. 9, pp. 2065–2074, Sep. 2012.
- [50] C. K. Lee, W. X. Zhong, and S. Y. R. Hui, "Effects of magnetic coupling of nonadjacent resonators on wireless power domino-resonator systems," *IEEE Transactions on Power Electronics*, vol. 27, no. 4, pp. 1905–1916, Apr. 2012.
- [51] S. Y. R. Hui and W. C. Ho, "A new generation of universal contactless battery charging platform for portable consumer electronic equipment," in *Proceedings of IEEE Annual Power Electronics Specialists Conference*, vol. 1, Jun. 2004, pp. 638–644 Vol.1.

- [52] C. S. Wang, O. H. Stielau, and G. A. Covic, “Design considerations for a contactless electric vehicle battery charger,” *IEEE Transactions on Industrial Electronics*, vol. 52, no. 5, pp. 1308–1314, Oct. 2005.
- [53] S. Y. R. Hui and W. W. C. Ho, “A new generation of universal contactless battery charging platform for portable consumer electronic equipment,” *IEEE Transactions on Power Electronics*, vol. 20, no. 3, pp. 620–627, May 2005.
- [54] X. Liu and S. Y. R. Hui, “Equivalent circuit modeling of a multilayer planar winding array structure for use in a universal contactless battery charging platform,” *IEEE Transactions on Power Electronics*, vol. 22, no. 1, pp. 21–29, Jan. 2007.
- [55] ———, “Optimal design of a hybrid winding structure for planar contactless battery charging platform,” *IEEE Transactions on Power Electronics*, vol. 23, no. 1, pp. 455–463, Jan. 2008.
- [56] Z. N. Low, R. A. Chinga, R. Tseng, and J. Lin, “Design and test of a high-power high-efficiency loosely coupled planar wireless power transfer system,” *IEEE Transactions on Industrial Electronics*, vol. 56, no. 5, pp. 1801–1812, May 2009.
- [57] X. Zhang, S. L. Ho, and W. N. Fu, “Quantitative analysis of a wireless power transfer cell with planar spiral structures,” *IEEE Transactions on Magnetics*, vol. 47, no. 10, pp. 3200–3203, Oct. 2011.
- [58] S. Y. R. Hui, “Planar wireless charging technology for portable electronic products and Qi,” *Proceedings of the IEEE*, vol. 101, no. 6, pp. 1290–1301, Jun. 2013.

- [59] J. J. Casanova, Z. N. Low, and J. Lin, “A loosely coupled planar wireless power system for multiple receivers,” *IEEE Transactions on Industrial Electronics*, vol. 56, no. 8, pp. 3060–3068, Aug. 2009.
- [60] K. E. Koh, T. C. Beh, T. Imura, and Y. Hori, “Impedance matching and power division using impedance inverter for wireless power transfer via magnetic resonant coupling,” *IEEE Transactions on Industry Applications*, vol. 50, no. 3, pp. 2061–2070, May 2014.
- [61] B. H. Waters, B. J. Mahoney, V. Ranganathan, and J. R. Smith, “Power delivery and leakage field control using an adaptive phased array wireless power system,” *IEEE Transactions on Power Electronics*, vol. 30, no. 11, pp. 6298–6309, Nov. 2015.
- [62] Y. J. Kim, D. Ha, W. J. Chappell, and P. P. Irazoqui, “Selective wireless power transfer for smart power distribution in a miniature-sized multiple-receiver system,” *IEEE Transactions on Industrial Electronics*, vol. 63, no. 3, pp. 1853–1862, Mar. 2016.
- [63] J. Zhou, B. Luo, X. Zhang, and Y. Hu, “Extendible load-isolation wireless charging platform for multi-receiver applications,” *IET Power Electronics*, vol. 10, no. 1, pp. 134–142, Jan. 2017.
- [64] Wireless Power Consortium, “Qi system description: Wireless power transfer,” Version 1.2.2, Apr. 2016.
- [65] A. Alliance”, “A4WP wireless power transfer system baseline system specification (BSS),” Version 1.3, Nov. 2014.
- [66] M. W. Baker and R. Sarpeshkar, “Feedback analysis and design of RF power links for low-power bionic systems,” *IEEE Transactions on Biomedical Circuits and Systems*, vol. 1, no. 1, pp. 28–38, Mar. 2007.

- [67] N. M. Neihart and R. R. Harrison, "Micropower circuits for bidirectional wireless telemetry in neural recording applications," *IEEE Transactions on Biomedical Engineering*, vol. 52, no. 11, pp. 1950–1959, Nov. 2005.
- [68] H. Chen, M. Liu, C. Jia, C. Zhang, and Z. Wang, "Low power IC design of the wireless monitoring system of the orthopedic implants," in *Proceedings of Annual International Conference of the IEEE Engineering in Medicine and Biology Society*, Aug. 2007, pp. 5766–5769.
- [69] S. Smith, T. B. Tang, J. G. Terry, J. T. M. Stevenson, B. W. Flynn, H. M. Reekie, A. F. Murray, A. M. Gundlach, D. Renshaw, B. Dhillon, A. Ohtori, Y. Inoue, and A. J. Walton, "Development of a miniaturised drug delivery system with wireless power transfer and communication," *IET Nanobiotechnology*, vol. 1, no. 5, pp. 80–86, Oct. 2007.
- [70] G. Wang, W. Liu, M. Sivaprakasam, M. Zhou, J. D. Weiland, and M. S. Humayun, "A dual band wireless power and data telemetry for retinal prosthesis," in *Proceedings of International Conference of the IEEE Engineering in Medicine and Biology Society*, Aug. 2006, pp. 4392–4395.
- [71] M. Catrysse, B. Hermans, and R. Puers, "An inductive power system with integrated bi-directional data-transmission," *Sensors and Actuators A: Physical*, vol. 115, no. 2, pp. 221–229, 2004.
- [72] M. Ghovanloo and K. Najafi, "A wireless implantable multichannel microstimulating system-on-a-chip with modular architecture," *IEEE Transactions on Neural Systems and Rehabilitation Engineering*, vol. 15, no. 3, pp. 449–457, Sep. 2007.
- [73] L. Wu, Z. Yang, E. Basham, and W. Liu, "An efficient wireless power link for high voltage retinal implant," in *Proceedings of IEEE Biomedical Circuits and Systems Conference*, Nov. 2008, pp. 101–104.

- [74] A. K. RamRakhyani, S. Mirabbasi, and M. Chiao, "Design and optimization of resonance-based efficient wireless power delivery systems for biomedical implants," *IEEE Transactions on Biomedical Circuits and Systems*, vol. 5, no. 1, pp. 48–63, Feb. 2011.
- [75] Q. Chen, S. C. Wong, C. K. Tse, and X. Ruan, "Analysis, design, and control of a transcutaneous power regulator for artificial hearts," *IEEE Transactions on Biomedical Circuits and Systems*, vol. 3, no. 1, pp. 23–31, Feb. 2009.
- [76] H. Y. Leung, D. M. Budgett, and A. P. Hu, "Minimizing power loss in air-cored coils for TET heart pump systems," *IEEE Journal on Emerging and Selected Topics in Circuits and Systems*, vol. 1, no. 3, pp. 412–419, Sep. 2011.
- [77] S. Kim, J. S. Ho, L. Y. Chen, and A. S. Poon, "Wireless power transfer to a cardiac implant," *Applied Physics Letters*, vol. 101, no. 7, p. 073701, 2012.
- [78] S. C. Tang, T. L. T. Lun, Z. Guo, K. W. Kwok, and N. J. McDannold, "Intermediate range wireless power transfer with segmented coil transmitters for implantable heart pumps," *IEEE Transactions on Power Electronics*, vol. 32, no. 5, pp. 3844–3857, May 2017.
- [79] S. H. Cho, L. Cauller, W. Rosellini, and J. B. Lee, "A mems-based fully-integrated wireless neurostimulator," in *Proceedings of IEEE International Conference on Micro Electro Mechanical Systems (MEMS)*, Jan. 2010, pp. 300–303.
- [80] S. H. Cho, N. Xue, L. Cauller, W. Rosellini, and J. B. Lee, "A SU-8-based fully integrated biocompatible inductively powered wireless

- neurostimulator,” *Journal of Microelectromechanical Systems*, vol. 22, no. 1, pp. 170–176, Feb. 2013.
- [81] T. B. Tang, S. Smith, B. W. Flynn, J. T. M. Stevenson, A. M. Gundlach, H. M. Reekie, A. F. Murray, D. Renshaw, B. Dhillon, A. Ohtori, Y. Inoue, J. G. Terry, and A. J. Walton, “Implementation of wireless power transfer and communications for an implantable ocular drug delivery system,” *IET Nanobiotechnology*, vol. 2, no. 3, pp. 72–79, Sep. 2008.
- [82] C. C. Chan, “The state of the art of electric, hybrid, and fuel cell vehicles,” *Proceedings of the IEEE*, vol. 95, no. 4, pp. 704–718, Apr. 2007.
- [83] C. C. Chan, A. Bouscayrol, and K. Chen, “Electric, hybrid, and fuel-cell vehicles: Architectures and modeling,” *IEEE Transactions on Vehicular Technology*, vol. 59, no. 2, pp. 589–598, Feb. 2010.
- [84] S. Lukic and Z. Pantic, “Cutting the cord: Static and dynamic inductive wireless charging of electric vehicles,” *IEEE Electrification Magazine*, vol. 1, no. 1, pp. 57–64, Sep. 2013.
- [85] Z. Bi, T. Kan, C. C. Mi, Y. Zhang, Z. Zhao, and G. A. Keoleian, “A review of wireless power transfer for electric vehicles: Prospects to enhance sustainable mobility,” *Applied Energy*, vol. 179, pp. 413–425, Oct. 2016.
- [86] J. Sallan, J. L. Villa, A. Llombart, and J. F. Sanz, “Optimal design of ICPT systems applied to electric vehicle battery charge,” *IEEE Transactions on Industrial Electronics*, vol. 56, no. 6, pp. 2140–2149, Jun. 2009.
- [87] U. K. Madawala and D. J. Thrimawithana, “A bidirectional inductive power interface for electric vehicles in V2G systems,” *IEEE Transactions on Industrial Electronics*, vol. 58, no. 10, pp. 4789–4796, Oct. 2011.

- [88] M. Budhia, J. T. Boys, G. A. Covic, and C. Y. Huang, "Development of a single-sided flux magnetic coupler for electric vehicle IPT charging systems," *IEEE Transactions on Industrial Electronics*, vol. 60, no. 1, pp. 318–328, Jan. 2013.
- [89] M. Chinthavali, O. C. Onar, S. L. Campbell, and L. M. Tolbert, "Integrated charger with wireless charging and boost functions for PHEV and EV applications," in *Proceedings of IEEE Transportation Electrification Conference and Expo (ITEC)*, Jun. 2015, pp. 1–8.
- [90] B. Goeldi, J. Tritschler, and S. Reichert, "Measurement results of a 22 kW bidirectional inductive charger," in *Proceedings of International Exhibition and Conference for Power Electronics, Intelligent Motion, Renewable Energy and Energy Management (PCIM Europe 2015)*, May 2015, pp. 1–8.
- [91] T. Kan, T. D. Nguyen, J. C. White, R. K. Malhan, and C. C. Mi, "A new integration method for an electric vehicle wireless charging system using LCC compensation topology: Analysis and design," *IEEE Transactions on Power Electronics*, vol. 32, no. 2, pp. 1638–1650, Feb. 2017.
- [92] S. Lee, J. Huh, C. Park, N. S. Choi, G. H. Cho, and C. T. Rim, "On-line electric vehicle using inductive power transfer system," in *Proceedings of IEEE Energy Conversion Congress and Exposition (ECCE)*, Sep. 2010, pp. 1598–1601.
- [93] J. Huh, S. W. Lee, W. Y. Lee, G. H. Cho, and C. T. Rim, "Narrow-width inductive power transfer system for online electrical vehicles," *IEEE Transactions on Power Electronics*, vol. 26, no. 12, pp. 3666–3679, Dec. 2011.
- [94] W. Y. Lee, J. Huh, S. Y. Choi, X. V. Thai, J. H. Kim, E. A. Al-Ammar, M. A. El-Kady, and C. T. Rim, "Finite-width magnetic mirror models of

- mono and dual coils for wireless electric vehicles,” *IEEE Transactions on Power Electronics*, vol. 28, no. 3, pp. 1413–1428, Mar. 2013.
- [95] S. Lee, B. Choi, and C. T. Rim, “Dynamics characterization of the inductive power transfer system for online electric vehicles by laplace phasor transform,” *IEEE Transactions on Power Electronics*, vol. 28, no. 12, pp. 5902–5909, Dec. 2013.
- [96] J. H. Kim, B. S. Lee, J. H. Lee, S. H. Lee, C. B. Park, S. M. Jung, S. G. Lee, K. P. Yi, and J. Baek, “Development of 1-MW inductive power transfer system for a high-speed train,” *IEEE Transactions on Industrial Electronics*, vol. 62, no. 10, pp. 6242–6250, Oct. 2015.
- [97] S. Y. Choi, B. W. Gu, S. Y. Jeong, and C. T. Rim, “Advances in wireless power transfer systems for roadway-powered electric vehicles,” *IEEE Journal of Emerging and Selected Topics in Power Electronics*, vol. 3, no. 1, pp. 18–36, Mar. 2015.
- [98] C. C. Mi, G. Buja, S. Y. Choi, and C. T. Rim, “Modern advances in wireless power transfer systems for roadway powered electric vehicles,” *IEEE Transactions on Industrial Electronics*, vol. 63, no. 10, pp. 6533–6545, Oct. 2016.
- [99] Y. Hiraga, J. Hirai, Y. Kaku, Y. Nitta, A. Kawamura, and K. Ishioka, “Decentralized control of machines with the use of inductive transmission of power and signal,” in *Proceedings of IEEE Industry Applications Society Annual Meeting*, Oct. 1994, pp. 875–881 vol.2.
- [100] T. Assaf, C. Stefanini, and P. Dario, “Autonomous underwater biorobots: A wireless system for power transfer,” *IEEE Robotics Automation Magazine*, vol. 20, no. 3, pp. 26–32, Sep. 2013.

- [101] C. Park, S. Lee, G. H. Cho, S. Y. Choi, and C. T. Rim, "Two-dimensional inductive power transfer system for mobile robots using evenly displaced multiple pickups," *IEEE Transactions on Industry Applications*, vol. 50, no. 1, pp. 558–565, Jan. 2014.
- [102] H. H. Wu, J. T. Boys, and G. A. Covic, "An AC processing pickup for IPT systems," *IEEE Transactions on Power Electronics*, vol. 25, no. 5, pp. 1275–1284, May 2010.
- [103] H. H. Wu, G. A. Covic, J. T. Boys, and D. J. Robertson, "A series-tuned inductive-power-transfer pickup with a controllable AC-voltage output," *IEEE Transactions on Power Electronics*, vol. 26, no. 1, pp. 98–109, Jan. 2011.
- [104] X. Qu, W. Zhang, S. C. Wong, and C. K. Tse, "Design of a current-source-output inductive power transfer LED lighting system," *IEEE Journal of Emerging and Selected Topics in Power Electronics*, vol. 3, no. 1, pp. 306–314, Mar. 2015.
- [105] T. McGinnis, C. P. Henze, and K. Conroy, "Inductive power system for autonomous underwater vehicles," in *Proceedings of OCEANS*, Sep. 2007, pp. 1–5.
- [106] Z. Cheng, Y. Lei, K. Song, and C. Zhu, "Design and loss analysis of loosely coupled transformer for an underwater high-power inductive power transfer system," *IEEE Transactions on Magnetics*, vol. 51, no. 7, pp. 1–10, Jul. 2015.
- [107] M. Lin, C. Yang, D. Li, T. Zhang, and T. Wang, "Design and analysis of the load adaptive IPT system applied to underwater docking system," in *Proceedings of MTS/IEEE OCEANS*, Sep. 2016, pp. 1–7.

- [108] W. Zhong, C. K. Lee, and S. Y. R. Hui, “General analysis on the use of Tesla’s resonators in domino forms for wireless power transfer,” *IEEE Transactions on Industrial Electronics*, vol. 60, no. 1, pp. 261–270, Jan. 2013.
- [109] C. Zhang, N. Tang, W. Zhong, C. K. Lee, and R. S. Y. Hui, “A new energy harvesting and wireless power transfer system for smart grid,” in *Proceedings of IEEE International Symposium on Power Electronics for Distributed Generation Systems (PEDG)*, Jun. 2016, pp. 1–5.
- [110] R. Laouamer, M. Brunello, J. P. Ferrieux, O. Normand, and N. Buchheit, “A multi-resonant converter for non-contact charging with electromagnetic coupling,” in *Proceedings of International Conference on Industrial Electronics, Control and Instrumentation (IECON)*, vol. 2, Nov. 1997, pp. 792–797 vol.2.
- [111] H. Sakamoto, K. Harada, S. Washimiya, K. Takehara, Y. Matsuo, and F. Nakao, “Large air-gap coupler for inductive charger [for electric vehicles],” *IEEE Transactions on Magnetics*, vol. 35, no. 5, pp. 3526–3528, Sep. 1999.
- [112] J. Hirai, T. W. Kim, and A. Kawamura, “Study on intelligent battery charging using inductive transmission of power and information,” *IEEE Transactions on Power Electronics*, vol. 15, no. 2, pp. 335–345, Mar. 2000.
- [113] S. Valtchev, B. Borges, K. Brandisky, and J. B. Klaassens, “Resonant contactless energy transfer with improved efficiency,” *IEEE Transactions on Power Electronics*, vol. 24, no. 3, pp. 685–699, Mar. 2009.
- [114] A. J. Moradewicz and M. P. Kazmierkowski, “Contactless energy transfer system with FPGA-controlled resonant converter,” *IEEE Transactions on Industrial Electronics*, vol. 57, no. 9, pp. 3181–3190, Sep. 2010.

- [115] Y. Matsuo, O. M. Kondoh, and F. Nakao, “Controlling new die mechanisms for magnetic characteristics of super-large ferrite cores,” *IEEE Transactions on Magnetics*, vol. 36, no. 5, pp. 3411–3414, Sep. 2000.
- [116] F. Nakao, Y. Matsuo, M. Kitaoka, and H. Sakamoto, “Ferrite core couplers for inductive chargers,” in *Proceedings of the Power Conversion Conference (PCC)*, vol. 2, Aug. 2002, pp. 850–854.
- [117] M. Budhia, G. A. Covic, and J. T. Boys, “Design and optimization of circular magnetic structures for lumped inductive power transfer systems,” *IEEE Transactions on Power Electronics*, vol. 26, no. 11, pp. 3096–3108, Nov. 2011.
- [118] M. Budhia, G. A. Covic, J. T. Boys, and C. Y. Huang, “Development and evaluation of single sided flux couplers for contactless electric vehicle charging,” in *Proceedings of IEEE Energy Conversion Congress and Exposition (ECCE)*, Sep. 2011, pp. 614–621.
- [119] M. Budhia, G. Covic, and J. Boys, “A new IPT magnetic coupler for electric vehicle charging systems,” in *Proceedings of Annual Conference on IEEE Industrial Electronics Society (IECON)*, Nov. 2010, pp. 2487–2492.
- [120] A. Zaheer, D. Kacprzak, and G. A. Covic, “A bipolar receiver pad in a lumped IPT system for electric vehicle charging applications,” in *Proceedings of IEEE Energy Conversion Congress and Exposition (ECCE)*, Sep. 2012, pp. 283–290.
- [121] W. Zhang, J. C. White, A. M. Abraham, and C. C. Mi, “Loosely coupled transformer structure and interoperability study for EV wireless charging systems,” *IEEE Transactions on Power Electronics*, vol. 30, no. 11, pp. 6356–6367, Nov. 2015.

- [122] J. Achterberg, E. A. Lomonova, and J. de Boeij, “Coil array structures compared for contactless battery charging platform,” *IEEE Transactions on Magnetics*, vol. 44, no. 5, pp. 617–622, May 2008.
- [123] H. Y. Shen, J. Y. Lee, and T. W. Chang, “Study of contactless inductive charging platform with core array structure for portable products,” in *Proceedings of International Conference on Consumer Electronics, Communications and Networks (CECNet)*, Apr. 2011, pp. 756–759.
- [124] G. A. Covic and J. T. Boys, “Modern trends in inductive power transfer for transportation applications,” *IEEE Journal of Emerging and Selected Topics in Power Electronics*, vol. 1, no. 1, pp. 28–41, Mar. 2013.
- [125] G. R. Nagendra, G. A. Covic, and J. T. Boys, “Sizing of inductive power pads for dynamic charging of evs on ipt highways,” *IEEE Transactions on Transportation Electrification*, vol. 3, no. 2, pp. 405–417, Jun. 2017.
- [126] C. S. Wang, G. A. Covic, and O. H. Stielau, “Power transfer capability and bifurcation phenomena of loosely coupled inductive power transfer systems,” *IEEE Transactions on Industrial Electronics*, vol. 51, no. 1, pp. 148–157, Feb. 2004.
- [127] N. A. Keeling, G. A. Covic, and J. T. Boys, “A unity-power-factor IPT pickup for high-power applications,” *IEEE Transactions on Industrial Electronics*, vol. 57, no. 2, pp. 744–751, Feb. 2010.
- [128] C. S. Wang, G. A. Covic, and O. H. Stielau, “Investigating an LCL load resonant inverter for inductive power transfer applications,” *IEEE Transactions on Power Electronics*, vol. 19, no. 4, pp. 995–1002, Jul. 2004.

- [129] C. S. Wang, O. H. Stielau, and G. A. Covic, “Design considerations for a contactless electric vehicle battery charger,” *IEEE Transactions on Industrial Electronics*, vol. 52, no. 5, pp. 1308–1314, Oct. 2005.
- [130] Z. Pantic, S. Bai, and S. M. Lukic, “ZCS *LCC*-compensated resonant inverter for inductive-power-transfer application,” *IEEE Transactions on Industrial Electronics*, vol. 58, no. 8, pp. 3500–3510, Aug. 2011.
- [131] B. Wang, A. P. Hu, and D. Budgett, “Maintaining middle zero voltage switching operation of parallel-parallel tuned wireless power transfer system under bifurcation,” *IET Power Electronics*, vol. 7, no. 1, pp. 78–84, Jan. 2014.
- [132] N. C. Kuo, B. Zhao, and A. M. Niknejad, “Bifurcation analysis in weakly-coupled inductive power transfer systems,” *IEEE Transactions on Circuits and Systems I: Regular Papers*, vol. 63, no. 5, pp. 727–738, May 2016.
- [133] Z. Huang, S. C. Wong, and C. K. Tse, “Design methodology of a series-series inductive power transfer system for electric vehicle battery charger application,” in *Proceedings of IEEE Energy Conversion Congress and Exposition (ECCE)*, Sep. 2014, pp. 1778–1782.
- [134] ———, “Design of a single-stage inductive-power-transfer converter for efficient EV battery charging,” *IEEE Transactions on Vehicular Technology*, vol. 66, no. 7, pp. 5808–5821, Jul. 2017.
- [135] X. Qu, Y. Jing, H. Han, S. C. Wong, and C. K. Tse, “Higher order compensation for inductive-power-transfer converters with constant-voltage or constant-current output combating transformer parameter constraints,” *IEEE Transactions on Power Electronics*, vol. 32, no. 1, pp. 394–405, Jan. 2017.

- [136] W. Zhang, S. C. Wong, C. K. Tse, and Q. Chen, “Load-independent duality of current and voltage outputs of a series- or parallel-compensated inductive power transfer converter with optimized efficiency,” *IEEE Journal of Emerging and Selected Topics in Power Electronics*, vol. 3, no. 1, pp. 137–146, Mar. 2015.
- [137] —, “Analysis and comparison of secondary series- and parallel-compensated inductive power transfer systems operating for optimal efficiency and load-independent voltage-transfer ratio,” *IEEE Transactions on Power Electronics*, vol. 29, no. 6, pp. 2979–2990, Jun. 2014.
- [138] S. Li, W. Li, J. Deng, T. D. Nguyen, and C. C. Mi, “A double-sided lcc compensation network and its tuning method for wireless power transfer,” *IEEE Transactions on Vehicular Technology*, vol. 64, no. 6, pp. 2261–2273, Jun. 2015.
- [139] J. Hou, Q. Chen, X. Ren, X. Ruan, S. C. Wong, and C. K. Tse, “Precise characteristics analysis of series/series-parallel compensated contactless resonant converter,” *IEEE Journal of Emerging and Selected Topics in Power Electronics*, vol. 3, no. 1, pp. 101–110, Mar. 2015.
- [140] W. Zhang and C. C. Mi, “Compensation topologies of high-power wireless power transfer systems,” *IEEE Transactions on Vehicular Technology*, vol. 65, no. 6, pp. 4768–4778, Jun. 2016.
- [141] J. Byeon, M. Kang, M. Kim, D. M. Joo, and B. K. Lee, “Hybrid control of inductive power transfer charger for electric vehicles using LCCL-S resonant network in limited operating frequency range,” in *Proceedings of IEEE Energy Conversion Congress and Exposition (ECCE)*, Sep. 2016, pp. 1–6.
- [142] J. Tian and A. P. Hu, “A DC-voltage-controlled variable capacitor for stabilizing the ZVS frequency of a resonant converter for wireless power

- transfer,” *IEEE Transactions on Power Electronics*, vol. 32, no. 3, pp. 2312–2318, Mar. 2017.
- [143] J. L. Villa, J. Sallan, J. F. S. Osorio, and A. Llombart, “High-misalignment tolerant compensation topology for ICPT systems,” *IEEE Transactions on Industrial Electronics*, vol. 59, no. 2, pp. 945–951, Feb. 2012.
- [144] H. Feng, T. Cai, S. Duan, J. Zhao, X. Zhang, and C. Chen, “An LCC-compensated resonant converter optimized for robust reaction to large coupling variation in dynamic wireless power transfer,” *IEEE Transactions on Industrial Electronics*, vol. 63, no. 10, pp. 6591–6601, Oct. 2016.
- [145] L. Xu, Q. Chen, X. Ren, S. C. Wong, and C. K. Tse, “Self-oscillating resonant converter with contactless power transfer and integrated current sensing transformer,” *IEEE Transactions on Power Electronics*, vol. 32, no. 6, pp. 4839–4851, Jun. 2017.
- [146] E. Gati, G. Kampitsis, and S. Manias, “Variable frequency controller for inductive power transfer in dynamic conditions,” *IEEE Transactions on Power Electronics*, vol. 32, no. 2, pp. 1684–1696, Feb. 2017.
- [147] U. K. Madawala, M. Neath, and D. J. Thrimawithana, “A power-frequency controller for bidirectional inductive power transfer systems,” *IEEE Transactions on Industrial Electronics*, vol. 60, no. 1, pp. 310–317, Jan. 2013.
- [148] C. Zheng, J. S. Lai, R. Chen, W. E. Faraci, Z. U. Zahid, B. Gu, L. Zhang, G. Lisi, and D. Anderson, “High-efficiency contactless power transfer system for electric vehicle battery charging application,” *IEEE Journal of Emerging and Selected Topics in Power Electronics*, vol. 3, no. 1, pp. 65–74, Mar. 2015.

- [149] A. Namadmalan, “Self-oscillating tuning loops for series resonant inductive power transfer systems,” *IEEE Transactions on Power Electronics*, vol. 31, no. 10, pp. 7320–7327, Oct. 2016.
- [150] H. H. Wu, A. Gilchrist, K. D. Sealy, and D. Bronson, “A high efficiency 5 kW inductive charger for evs using dual side control,” *IEEE Transactions on Industrial Informatics*, vol. 8, no. 3, pp. 585–595, Aug. 2012.
- [151] Y. Zhang, Z. Zhao, and K. Chen, “Frequency decrease analysis of resonant wireless power transfer,” *IEEE Transactions on Power Electronics*, vol. 29, no. 3, pp. 1058–1063, Mar. 2014.
- [152] N. Keeling, G. A. Covic, F. Hao, L. George, and J. T. Boys, “Variable tuning in LCL compensated contactless power transfer pickups,” in *Proceedings of IEEE Energy Conversion Congress and Exposition (ECCE)*, Sep. 2009, pp. 1826–1832.
- [153] G. A. Covic, J. T. Boys, A. M. W. Tam, and J. C. H. Peng, “Self tuning pickups for inductive power transfer,” in *Proceedings of IEEE Power Electronics Specialists Conference*, Jun. 2008, pp. 3489–3494.
- [154] A. Kamineni, G. A. Covic, and J. T. Boys, “Self-tuning power supply for inductive charging,” *IEEE Transactions on Power Electronics*, vol. 32, no. 5, pp. 3467–3479, May 2017.
- [155] J. Kim and J. Jeong, “Range-adaptive wireless power transfer using multiloop and tunable matching techniques,” *IEEE Transactions on Industrial Electronics*, vol. 62, no. 10, pp. 6233–6241, Oct. 2015.
- [156] T. C. Beh, M. Kato, T. Imura, S. Oh, and Y. Hori, “Automated impedance matching system for robust wireless power transfer via magnetic resonance

- coupling,” *IEEE Transactions on Industrial Electronics*, vol. 60, no. 9, pp. 3689–3698, Sep. 2013.
- [157] C. Auvigne, P. Germano, D. Ladas, and Y. Perriard, “A dual-topology ICPT applied to an electric vehicle battery charger,” in *Proceedings of International Conference on Electrical Machines*, Sep. 2012, pp. 2287–2292.
- [158] X. Qu, H. Han, S. C. Wong, C. K. Tse, and W. Chen, “Hybrid IPT topologies with constant current or constant voltage output for battery charging applications,” *IEEE Transactions on Power Electronics*, vol. 30, no. 11, pp. 6329–6337, Nov. 2015.
- [159] R. Mai, Y. Chen, Y. Li, Y. Zhang, G. Cao, and Z. He, “Inductive power transfer for massive electric bicycles charging based on hybrid topology switching with a single inverter,” *IEEE Transactions on Power Electronics*, vol. 32, no. 8, pp. 5897–5906, Aug. 2017.
- [160] W. X. Zhong and S. Y. R. Hui, “Maximum energy efficiency tracking for wireless power transfer systems,” *IEEE Transactions on Power Electronics*, vol. 30, no. 7, pp. 4025–4034, Jul. 2015.
- [161] L. J. Chen, J. T. Boys, and G. A. Covic, “Power management for multiple-pickup IPT systems in materials handling applications,” *IEEE Journal of Emerging and Selected Topics in Power Electronics*, vol. 3, no. 1, pp. 163–176, Mar. 2015.
- [162] A. Zaheer, M. Neath, H. Z. Z. Beh, and G. A. Covic, “A dynamic ev charging system for slow moving traffic applications,” *IEEE Transactions on Transportation Electrification*, vol. 3, no. 2, pp. 354–369, Jun. 2017.
- [163] H. Li, J. Li, K. Wang, W. Chen, and X. Yang, “A maximum efficiency point tracking control scheme for wireless power transfer systems using magnetic

- resonant coupling,” *IEEE Transactions on Power Electronics*, vol. 30, no. 7, pp. 3998–4008, Jul. 2015.
- [164] M. Fu, H. Yin, X. Zhu, and C. Ma, “Analysis and tracking of optimal load in wireless power transfer systems,” *IEEE Transactions on Power Electronics*, vol. 30, no. 7, pp. 3952–3963, Jul. 2015.
- [165] T. D. Yeo, D. Kwon, S. T. Khang, and J. W. Yu, “Design of maximum efficiency tracking control scheme for closed-loop wireless power charging system employing series resonant tank,” *IEEE Transactions on Power Electronics*, vol. 32, no. 1, pp. 471–478, Jan. 2017.
- [166] International Commission on Non-Ionizing Radiation Protection, “ICNIRP guidelines for limiting exposure to time-varying electric, magnetic, and electromagnetic fields (up to 300 ghz),” *Health physics*, vol. 74, no. 4, pp. 494–522, 1998.
- [167] F. Y. Lin, A. Zaheer, M. Budhia, and G. A. Covic, “Reducing leakage flux in IPT systems by modifying pad ferrite structures,” in *Proceedings of IEEE Energy Conversion Congress and Exposition (ECCE)*, Sep. 2014, pp. 1770–1777.
- [168] Y. Nagatsuka, N. Ehara, Y. Kaneko, S. Abe, and T. Yasuda, “Compact contactless power transfer system for electric vehicles,” in *Proceedings of International Power Electronics Conference (IPEC - ECCE ASIA)*, Jun. 2010, pp. 807–813.
- [169] S. Ahn, J. Pak, T. Song, H. Lee, J. G. Byun, D. Kang, C. S. Choi, E. Kim, J. Ryu, M. Kim, Y. Cha, Y. Chun, C. T. Rim, J. H. Yim, D. H. Cho, and J. Kim, “Low frequency electromagnetic field reduction techniques for the on-line electric vehicle (OLEV),” in *Proceedings of IEEE International Symposium on Electromagnetic Compatibility*, Jul. 2010, pp. 625–630.

- [170] J. Kim, J. Kim, S. Kong, H. Kim, I. S. Suh, N. P. Suh, D. H. Cho, J. Kim, and S. Ahn, "Coil design and shielding methods for a magnetic resonant wireless power transfer system," *Proceedings of the IEEE*, vol. 101, no. 6, pp. 1332–1342, Jun. 2013.
- [171] P. Wu, F. Bai, Q. Xue, X. Liu, and S. Y. R. Hui, "Use of frequency-selective surface for suppressing radio-frequency interference from wireless charging pads," *IEEE Transactions on Industrial Electronics*, vol. 61, no. 8, pp. 3969–3977, Aug. 2014.
- [172] S. Y. R. Hui, W. Zhong, and C. K. Lee, "A critical review of recent progress in mid-range wireless power transfer," *IEEE Transactions on Power Electronics*, vol. 29, no. 9, pp. 4500–4511, Sep. 2014.
- [173] W. Zhang, S. C. Wong, C. K. Tse, and Q. Chen, "Design for efficiency optimization and voltage controllability of series-series compensated inductive power transfer systems," *IEEE Transactions on Power Electronics*, vol. 29, no. 1, pp. 191–200, Jan. 2014.
- [174] G. A. Covic, J. T. Boys, M. L. G. Kissin, and H. G. Lu, "A three-phase inductive power transfer system for roadway-powered vehicles," *IEEE Transactions on Industrial Electronics*, vol. 54, no. 6, pp. 3370–3378, Dec. 2007.
- [175] M. K. Kazimierczuk and D. Czarkowski, *Resonant Power Converters*. Hoboken, N. J. : Wiley, 2011.
- [176] R. Bosshard, J. W. Kolar, J. Mhlethaler, I. Stevanović, B. Wunsch, and F. Canales, "Modeling and  $\eta$ - $\alpha$ -pareto optimization of inductive power transfer coils for electric vehicles," *IEEE Journal of Emerging and Selected Topics in Power Electronics*, vol. 3, no. 1, pp. 50–64, Mar. 2015.

- [177] C. Zheng, J. S. Lai, R. Chen, W. E. Faraci, Z. U. Zahid, B. Gu, L. Zhang, G. Lisi, and D. Anderson, "High-efficiency contactless power transfer system for electric vehicle battery charging application," *IEEE Journal of Emerging and Selected Topics in Power Electronics*, vol. 3, no. 1, pp. 65–74, Mar. 2015.
- [178] G. B. Joun and B. H. Cho, "An energy transmission system for an artificial heart using leakage inductance compensation of transcutaneous transformer," *IEEE Transactions on Power Electronics*, vol. 13, no. 6, pp. 1013–1022, Nov. 1998.
- [179] J. Shin, S. Shin, Y. Kim, S. Ahn, S. Lee, G. Jung, S. J. Jeon, and D. H. Cho, "Design and implementation of shaped magnetic-resonance-based wireless power transfer system for roadway-powered moving electric vehicles," *IEEE Transactions on Industrial Electronics*, vol. 61, no. 3, pp. 1179–1192, Mar. 2014.
- [180] A. Affanni, A. Bellini, G. Franceschini, P. Guglielmi, and C. Tassoni, "Battery choice and management for new-generation electric vehicles," *IEEE Transactions on Industrial Electronics*, vol. 52, no. 5, pp. 1343–1349, Oct. 2005.
- [181] C. Fernandez, O. Garcia, R. Prieto, J. A. Cobos, S. Gabriels, and G. V. D. Borghet, "Design issues of a core-less transformer for a contact-less application," in *Proceedings of IEEE Applied Power Electronics Conference and Exposition (APEC)*, vol. 1, 2002, pp. 339–345 vol.1.
- [182] J. Klein, "Synchronous buck MOSFET loss calculations with Excel model," *Fairchild Semiconductor Application note AN6005, Tech. Rep*, 2006.

- [183] W. Shen, T. T. Vo, and A. Kapoor, "Charging algorithms of lithium-ion batteries: An overview," in *2012 7th IEEE Conference on Industrial Electronics and Applications (ICIEA)*, Jul. 2012, pp. 1567–1572.
- [184] Y. S. Lee and Y. C. Cheng, "Design of switching regulator with combined fm and on-off control," *IEEE Transactions on Aerospace and Electronic Systems*, vol. AES-22, no. 6, pp. 725–731, Nov. 1986.
- [185] A. P. Sample, D. T. Meyer, and J. R. Smith, "Analysis, experimental results, and range adaptation of magnetically coupled resonators for wireless power transfer," *IEEE Transactions on Industrial Electronics*, vol. 58, no. 2, pp. 544–554, Feb. 2011.
- [186] R. P. Wojda and M. K. Kazimierzczuk, "Winding resistance of litz-wire and multi-strand inductors," *IET Power Electronics*, vol. 5, no. 2, pp. 257–268, Feb. 2012.
- [187] M. Fu, C. Ma, and X. Zhu, "A cascaded boost-buck converter for high-efficiency wireless power transfer systems," *IEEE Transactions on Industrial Informatics*, vol. 10, no. 3, pp. 1972–1980, Aug. 2014.
- [188] S. C. Wong and A. D. Brown, "Analysis, modeling, and simulation of series-parallel resonant converter circuits," *IEEE Transactions on Power Electronics*, vol. 10, no. 5, pp. 605–614, Sep. 1995.
- [189] A. M. Stankovic, B. C. Lesieutre, and T. Aydin, "Modeling and analysis of single-phase induction machines with dynamic phasors," *IEEE Transactions on Power Systems*, vol. 14, no. 1, pp. 9–14, Feb. 1999.
- [190] M. A. Elizondo, F. K. Tuffner, and K. P. Schneider, "Simulation of inrush dynamics for unbalanced distribution systems using dynamic-phasor

- models,” *IEEE Transactions on Power Systems*, vol. 32, no. 1, pp. 633–642, Jan. 2017.
- [191] S. Almr, S. Marithoz, and M. Morari, “Dynamic phasor model predictive control of switched mode power converters,” *IEEE Transactions on Control Systems Technology*, vol. 23, no. 1, pp. 349–356, Jan. 2015.
- [192] A. Emadi, A. Khaligh, C. H. Rivetta, and G. A. Williamson, “Constant power loads and negative impedance instability in automotive systems: definition, modeling, stability, and control of power electronic converters and motor drives,” *IEEE Transactions on Vehicular Technology*, vol. 55, no. 4, pp. 1112–1125, Jul. 2006.
- [193] R. Ahmadi, D. Paschedag, and M. Ferdowsi, “Closed-loop input and output impedances of DC-DC switching converters operating in voltage and current mode control,” in *IECON 2010 - 36th Annual Conference on IEEE Industrial Electronics Society*, Nov. 2010, pp. 2311–2316.
- [194] W. R. Liou, M. L. Yeh, and Y. L. Kuo, “A high efficiency dual-mode buck converter IC for portable applications,” *IEEE Transactions on Power Electronics*, vol. 23, no. 2, pp. 667–677, Mar. 2008.
- [195] L. Xu, Q. Chen, X. Ren, S. C. Wong, and C. K. Tse, “Self-oscillating resonant converter with contactless power transfer and integrated current sensing transformer,” *IEEE Transactions on Power Electronics*, vol. 32, no. 6, pp. 4839–4851, Jun. 2017.
- [196] O. Knecht, R. Bosshard, and J. W. Kolar, “High-efficiency transcutaneous energy transfer for implantable mechanical heart support systems,” *IEEE Transactions on Power Electronics*, vol. 30, no. 11, pp. 6221–6236, Nov. 2015.

- [197] R. D. Middlebrook, "Input filter considerations in design and application of switching regulators," in *IEEE IAS*, 1976, pp. 366–382.
- [198] C. M. Wildrick, F. C. Lee, B. H. Cho, and B. Choi, "A method of defining the load impedance specification for a stable distributed power system," in *Power Electronics Specialists Conference, 1993. PESC '93 Record., 24th Annual IEEE*, Jun. 1993, pp. 826–832.
- [199] A. Riccobono and E. Santi, "Comprehensive review of stability criteria for DC power distribution systems," *IEEE Transactions on Industry Applications*, vol. 50, no. 5, pp. 3525–3535, Sep. 2014.
- [200] J. Sun, "Impedance-based stability criterion for grid-connected inverters," *IEEE Transactions on Power Electronics*, vol. 26, no. 11, pp. 3075–3078, Nov. 2011.
- [201] X. Zhang, X. Ruan, and C. K. Tse, "Impedance-based local stability criterion for dc distributed power systems," *IEEE Transactions on Circuits and Systems I: Regular Papers*, vol. 62, no. 3, pp. 916–925, Mar. 2015.
- [202] S. Luo, Z. Ye, R.-L. Lin, and F. C. Lee, "A classification and evaluation of paralleling methods for power supply modules," in *Proceedings of Annual IEEE Power Electronics Specialists Conference*, vol. 2, 1999, pp. 901–908 vol.2.
- [203] M. Huang, S. C. Wong, C. K. Tse, and X. Ruan, "Catastrophic bifurcation in three-phase voltage-source converters," *IEEE Transactions on Circuits and Systems I: Regular Papers*, vol. 60, no. 4, pp. 1062–1071, Apr. 2013.
- [204] C. K. Tse, Y. M. Lai, R. J. Xie, and M. H. L. Chow, "Application of duality principle to synthesis of single-stage power-factor-correction voltage

regulators,” *International Journal of Circuit Theory and Applications*, vol. 31, no. 6, pp. 555–570, Nov. 2003.